

SUSTAINABLE BUILDING MATERIALS AND SYSTEMS

By

Harsha Bharadwaj

A THESIS

Submitted to
Michigan State University
in partial fulfillment of the requirements
for the degree of

Civil Engineering – Master of Science

2016

ABSTRACT

SUSTAINABLE BUILDING MATERIALS AND SYSTEMS

By

Harsha Bharadwaj

The supply line of a contingency base constitutes its greatest vulnerability. The reliance of a base on supply line can be reduced through maximum use of locally available construction materials and resources. The objective of this work is to make efficient use of indigenous materials should still provide adequate force protection, safety under relevant loads, quality of life, sustainability, energy-efficiency, economy and durability. Seismic, blast, impact and wind resistance are among the considerations in development of these building systems. A sandwich composite is devised as the primary module for development of the building system. The indigenous reinforcement systems selected for use in ferrocement sheets were two jute burlaps with different yarn spacing, and chicken mesh. These fabrics were characterized through performance of tension tests. Their failure modes and tensile load-deflection behavior were investigated. The tensile strength, stiffness and ductility of jute burlaps were found to compare favorably with those of chicken mesh, which is a viable reinforcement for use in ferrocement.

The flexure and compression test specimens were 1,200 mm long, 300 mm wide and 100 mm thick. The sandwich composite thickness comprised an 80 mm thick indigenous aerated concrete core and two 10 mm thick indigenous ferrocement skins with jute fabric reinforcement. The in-plane shear (diagonal compression) test components were 500 mm square with thickness and cross-sectional designs similar to those of flexure and compression test specimens.

ACKNOWLEDGEMENTS

I would like to express my gratitude to my supervisor, Dr. Parviz Soroushian for the useful comments, remarks and engagement through the learning process of this master thesis. Furthermore I would like to thank Faris Matakah and Weerasiri for conducting successful supporting research work, which constitutes a considerable portion of this report. Also, I like to thank the participants in my lab, who have willingly shared their precious time during the preparation of specimen and experimentation. I would like to thank my loved ones, who have supported me through the process, both by keeping me harmonious and helping me putting pieces together. I will be grateful forever for your support.

TABLE OF CONTENTS

LIST OF TABLES	vi
LIST OF FIGURES	vii
INTRODUCTION	1
DEVELOPMENT OF INDIGENOUS CEMENTITIOUS BINDERS	7
2.1 Introduction	7
2.2 Calcium Aluminosilicate-Based Binders	11
2.2.1 Introduction	11
2.2.2 Experimental Program	13
2.2.3 Test Results and Discussion	16
2.3 Refined Gypsum-Based Binders with Improved Moisture Resistance	19
2.3.1 Introduction	19
2.3.2 Experimental Program	20
2.3.3 Test Results and Discussion	21
2.4 Alkali Aluminosilicate-Based Binders	24
2.4.1 Introduction	24
2.4.2 Experimental Program	30
2.4.3 Test Results and Discussion	33
IDENTIFICATION AND CHARACTERIZATION OF INDIGENOUS REINFORCEMENT SYSTEMS	37
3.1 Introduction	37
3.2 Identification of Indigenous Reinforcement Systems	37
3.3 Experimental Program	40
3.4 Test Results and Discussion	43
DEVELOPMENT OF A STRUCTURALLY EFFICIENT INDIGENOUS BUILDING MODULE	50
4.1 Introduction	50
4.2 Preliminary Design of Military Building Systems with Sandwich Composite Module	52
4.2.1 Introduction	52
4.2.2 An Indigenous Alternative to the Beehive Shelter Under Extreme Loads	53
4.2.3 An Indigenous Alternative to B-Hut under Conventional Loads	63
DEVELOPMENT OF FERROCEMENT WITH INDIGENOUS REINFORCEMENT	68
5.1 Introduction	68
5.2 Some Theoretical Considerations	68
5.3 Experimental Program	70
5.4 Test Results and Discussion	74
5.5 A Preliminary Assessment of the Indigenous Ferrocement Joint Performance	86

DEVELOPMENT AND CHARACTERIZATION OF INDIGENOUS AERATED CONCRETE	88
6.1 Introduction	88
6.2 Experimental Program	91
6.2.1 Materials and Mix Designs	91
6.2.2 Foaming and Mixing Procedures	93
6.2.3 Test Procedures	94
6.3 Test Results and Discussion	98
A PRELIMINARY DEVELOPMENT AND EVALUATION OF SANDWICH COMPOSITES	103
7.1 Introduction	103
7.2 Production of a First-Generation Sandwich Composite	103
7.3 Evaluation of the First-Generation Sandwich Composite Behavior in Flexure and Under Projectile Impact	104
7.3.1 Flexural Behavior	104
7.3.2 Behavior Under Projectile Impact	107
PRODUCTION AND EVALUATION OF INDIGENOUS SANDWICH COMPOSITE	108
8.1 Introduction	108
8.2 Development of Shear Connectors at the Ferrocement Skin/Aerated Concrete Core Interface	109
8.3 Production, Experimental Evaluation and Theoretical Analysis of the Indigenous Sandwich Composite in Out-of-Plane Loading	113
8.3.1 Design and Loading Conditions	113
8.3.2 Production	114
8.3.3 Experimental Evaluation	114
8.3.4 Theoretical Analysis	116
8.4 Production, Experimental Evaluation and Theoretical Analysis of the Indigenous Sandwich Composite In-Plane Shear	119
8.4.1 Design and Loading Conditions	119
8.4.2 Production	121
8.4.3 Experimental Evaluation	122
8.4.4 Theoretical Analysis	123
8.5 A Preliminary Assessment of the Ease of Demolition	124
SUMMARY AND CONCLUSIONS	126
9.1 Introduction	126
9.2 Indigenous Cementitious Binders	126
9.3 Indigenous Reinforcement	130
9.4 Building System and Indigenous Sandwich Composite Module	130
9.5 Indigenous Ferrocement	131
9.6 Indigenous Aerated Concrete	132
9.7 Preliminary Work on Indigenous Sandwich Composites	133
9.8 Production and Structural Evaluation of Indigenous Sandwich Composites	134
9.9 Assessment of Competitive Advantages	136
9.10 Development of Numerical Modelling Capabilities	137
REFERENCES	138

LIST OF TABLES

Table 2.1 <i>Ranges of chemical compositions (wt.%) covered by pumice and lava [78, 79], and the chemical composition of the pumice used in the project obtain via XRF spectroscopy</i>	12
Table 2.2 <i>The mix designs (weight ratios) considered for volcanic deposit/lime binders</i>	15
Table 2.3 <i>Mix designs (weight ratios) evaluated for development of stable hydraulic binders based on gypsum</i>	21
Table 2.4 <i>Typical chemical composition (wt.%) of laterite clays [95-97], and the chemical composition of the laterite clay used in this investigation obtained via XRF spectroscopy</i>	27
Table 2.5 <i>The mix designs (weight ratios) considered for production of alkali aluminosilicate hydrate binders using laterite clay and indigenous alkali activators</i>	32
Table 3.1 <i>Mean values of the mechanical properties of jute and sisal yarns</i>	45
Table 3.2 <i>Mean values of the mechanical properties of jute burlaps and chicken mesh</i>	49
Table 4.1 <i>C-4 Equivalency Conversion Factors, from “The Handbook for Blast Resistant Design of Buildings</i>	55
Table 4.2 <i>The input parameters and the calculated depths of penetration of the projectile into the ferrocement skin and the aerated concrete core of the sandwich composite wall</i>	61
Table 5.1 <i>Calculation of reinforcement ratios for 20 mm thick ferrocement sheets with 1 or 2 layers of different reinforcing fabrics</i>	76
Table 5.2 <i>Calculation of minimum reinforcement ratios for different reinforcing fabrics</i>	77
Table 5.3 <i>Reinforcement volume fractions in 10 mm thick ferrocement sheets with 2 and 3 layers of different reinforcing fabrics</i>	77
Table 5.4 <i>Calculation of the bond strength of reinforcing fabric to the mortar matrix using the measured values of average crack spacing for the 10 mm thick ferrocement with three layers of ‘Jute 2’ burlap</i>	82
Table 6.1 <i>Mix designs (weight proportions) of aerated concrete materials</i>	92
Table 6.2 <i>Initial and secondary sorption rates of Mix #22 with saponin and #30 with liquid soap</i>	101

LIST OF FIGURES

Figure 1.1 <i>Natural fibers and fabrics used as reinforcement in organic building materials</i>	3
Figure 1.2 <i>Sandwich composite comprising indigenous ferrocement skin and indigenous aerated concrete core</i>	4
Figure 1.3 <i>Manual assembly and joining of indigenous sandwich composite panels into building systems</i>	4
Figure 1.4 <i>The Distributed damage mechanism of ferrocement</i>	5
Figure 2.1 <i>Major deposits of sodium carbonate (soda ash), soluble potassium salts (potash), gypsum, limestone and other mineral deposits in Africa and Middle East</i>	8
Figure 2.2 <i>Active volcanoes of Africa and Middle East</i>	8
Figure 2.3 <i>Laterite clay deposits in Africa and Middle East</i>	9
Figure 2.4 <i>Natron deposits in Africa</i>	9
Figure 2.5 <i>Plants which are sources of chemical additives for enhancement of cementitious Materials</i>	10
Figure 2.6 <i>Examples of ancient buildings employing different classes of hydraulic binders</i>	11
Figure 2.7 <i>Reaction of dissolved aluminosilicate with lime to form calcium aluminosilicate hydrate (C-A-S-H)</i>	13
Figure 2.8 <i>Hydration of dissolved calcium silicate to form calcium silicate hydrate (C-S-H)</i>	13
Figure 2.9 <i>Formation of Portlandite in the course of hydration of calcium silicates in Portland cement</i>	13
Figure 2.10 <i>The volcanic powders used in the experimental work</i>	14
Figure 2.11 <i>The scanning electron microscope (left) and the Emscope Sputter Coater analyzer (right) used in the project</i>	16
Figure 2.12 <i>X-ray <u>D</u>iffractometer</i>	16
Figure 2.13 <i>Compressive strength test results for volcanic deposit-based mortars at 7 and 14 days of age</i>	17
Figure 2.14 <i>SEM images of the pumice-based indigenous binder</i>	18
Figure 2.15 <i>Secondary electron images and EDS spectrum of the pumice-based binder</i>	18

Figure 2.16 <i>X-ray diffraction spectra for pumice and the pumice-based binder</i>	19
Figure 2.17 <i>Gypsum binder comprising entangled needles of gypsum crystals [92]</i>	20
Figure 2.18 <i>Compressive strength test results for gypsum-based mortars at age of 7 days</i>	22
Figure 2.19 <i>SEM image of the mortar with refined gypsum-based binder</i>	23
Figure 2.20 <i>Secondary electron images and EDS spectrum of the refined gypsum-based binder</i>	23
Figure 2.21 <i>X-ray diffraction spectrum of the refined gypsum-based binder</i>	24
Figure 2.22 <i>Transformation of calcined kaolinite clay (metakaolin) into a high-performance geopolymers binder using NaOH without or with waterglass [93]</i>	25
Figure 2.23 <i>Schematics of crosslinked and non-crosslinked tobermite which represent the generalized structures of the C-(N)-A-S-H and C-S-H type gels [42]</i>	30
Figure 2.24 <i>Laterite clay</i>	32
Figure 2.25 <i>An alkali-activated laterite clay cube specimen</i>	33
Figure 2.26 <i>Seven-day compressive strength test results for alkali-activated laterite clay (Mix 9 tested at 3 days of age)</i>	34
Figure 2.27 <i>SEM image of the laterite-based binder</i>	35
Figure 2.28 <i>Secondary electron images and EDS spectrum of the laterite-based binder</i>	35
Figure 2.29 <i>EDX spectra for outer and inner surfaces of laterite-based binder</i>	35
Figure 2.30 <i>X-ray diffraction spectra for laterite and the laterite-based binder</i>	36
Figure 3.1 <i>Indigenous reinforcement systems</i>	37
Figure 3.2 <i>Ferrocement trowel, spray and precast production</i>	37
Figure 3.3 <i>Some abundantly available plant fibers [99]</i>	38
Figure 3.4 <i>Location maps of some common plant fibers</i>	38
Figure 3.5 <i>Processing of natural plant fibers into yarn and fabric</i>	39
Figure 3.6 <i>The jute burlaps and the chicken mesh selected for use in Phase I project</i>	41
Figure 3.7 <i>Fabric tension test specimens and setup</i>	42
Figure 3.8 <i>Natural fiber yarns</i>	43
Figure 3.9 <i>Optic microscope image of the jute fiber yarn</i>	43
Figure 3.10 <i>The single yarn tension test setup</i>	43

Figure 3.11 <i>Typical tensile load-deflection (left) and stress-strain (right) behavior of jute fiber yarns</i>	45
Figure 3.12 <i>Typical tensile load-deflection (left) and stress-strain (right) behavior of sisal fiber yarns</i>	45
Figure 3.13 <i>Failure modes of fabric specimens in tension</i>	46
Figure 3.14 <i>Typical tensile load-deflection and stress-strain behavior of chicken mesh</i>	47
Figure 3.15 <i>Typical tensile load-deflection and stress-strain behavior of the 'Jute 1' burlap</i>	48
Figure 3.16 <i>Typical tensile load-deflection and stress-strain behavior of the 'Jute 2' burlap</i>	48
Figure 4.1 <i>Sandwich composite</i>	51
Figure 4.2 <i>Structural efficiency of sandwich composites subjected to flexure</i>	51
Figure 4.3 <i>Structural design requirements of sandwich composites</i>	52
Figure 4.4 <i>Structural damage and failure mechanisms of sandwich composites under flexural loading</i>	52
Figure 4.5 <i>Examples of military building systems</i>	53
Figure 4.6 <i>Out-of-plane and in-plane loading of wall panels</i>	54
Figure 4.7 <i>Blast wave propagation [104]</i>	55
Figure 4.8 <i>Conversion of scaled distance to pressure (Fig 6.6 in Handbook of Blast Resistant Design)</i>	55
Figure 4.9 <i>Wall panel subjected to out-of-plane blast pressure</i>	56
Figure 4.10 <i>Simplified flexural forces assumed to develop (only) in skins at failure</i>	57
Figure 4.11 <i>A single unit of the beehive shelter</i>	59
Figure 4.12 <i>In-plane blast loading on a beehive wall of 220 mm total thickness with 20 mm thick ferrocement skins</i>	59
Figure 4.13 <i>Global seismic hazard map</i>	60
Figure 4.14 <i>The projectile considered for assessment of penetration resistance (with mass of 25.7 g, traveling at a speed of 77.2 m/sec) [107]</i>	61
Figure 4.15 <i>Preliminary thicknesses of the indigenous sandwich composite constituents</i>	64
Figure 4.16 <i>Viable sandwich composite design for the B-hut walls</i>	67
Figure 5.1 <i>Multiple cracking of the tension face of a ferrocement panel under flexural loading</i>	69
Figure 5.2 <i>Geometric attributes of fabric reinforcement</i>	69

Figure 5.3 <i>Contribution of the reinforcing fabric to the tensile load-carrying capacity of ferrocement at a crack [100]</i>	70
Figure 5.4 <i>Preparation of ferrocement specimens</i>	71
Figure 5.5 <i>Ferrocement test specimen</i>	71
Figure 5.6 <i>Ferrocement tension test setup</i>	72
Figure 5.7 <i>The projectile penetration test rifle, and the projectile</i>	72
Figure 5.8 <i>Bond test specimen</i>	73
Figure 5.9 <i>Pullout test setup</i>	74
Figure 5.10 <i>Typical tensile load-deflection behavior of ferrocement sheets with 20 mm thickness and 2 layers of chicken mesh</i>	75
Figure 5.11 <i>Failure of the first-generation ferrocement specimens with formation and growth of a single crack</i>	75
Figure 5.12 <i>Tensile load-deflection and stress-strain curves for 10 mm thick ferrocement specimen reinforced with 3 layers of 'Jute 2' burlap</i>	79
Figure 5.13 <i>Multiple cracking of the 10 mm thick ferrocement specimen reinforced with 3 layers of 'Jute 2' in tension</i>	79
Figure 5.14 <i>Tensile failure modes of under-reinforced ferrocement sheets with chicken mesh and 'Jute 2' burlap reinforcement</i>	80
Figure 5.15 <i>Delamination of the mortar coating on the outer layer of the 'Jute 1' burlap with fine opening size</i>	80
Figure 5.16 <i>Tensile load-deflection and stress-strain curves for a 10 mm thick ferrocement sheet with two layers of 'Jute 1' burlap with fine opening size</i>	81
Figure 5.17 <i>Crack spacing in two ferrocement tension test specimens with 10 mm thickness and three layers of the 'Jute 2' burlap reinforcement</i>	82
Figure 5.18 <i>Tensile load-deflection and stress-strain behavior of an indigenous ferrocement skin with two layers of 'Jute 2' fabric reinforcement and indigenous pumice-lime matrix</i>	83
Figure 5.19 <i>Pictures depicting the front and back of the ferrocement sheet where two projectiles entered and exited the specimen</i>	83
Figure 5.20 <i>Failure modes of pullout test specimens</i>	85
Figure 5.21 <i>Failed bond test specimens with different embedment lengths</i>	85
Figure 5.22 <i>Experimental load-deflection curve in bond test with 130 mm embedment length of 'Jute 2' fabric</i>	86

Figure 5.23 <i>Failure by splitting of the ferrocement half of the bond test specimen with 50 mm embedment length</i>	86
Figure 6.1 <i>Examples of foam applications</i>	89
Figure 6.2 <i>Formation of stable air bubbles in water in the presence of surfactant molecules</i>	89
Figure 6.3 <i>Stabilization of larger air bubbles by surfactant molecules which orient themselves on the interfaces of larger air bubbles with water</i>	89
Figure 6.4 <i>A saponin molecule, and the foaming effects of plants caused by the presence of saponin</i>	90
Figure 6.5 <i>The egg white surfactant proteins and foaming effect</i>	91
Figure 6.6 <i>The cleaning actions of surfactants in liquid soap</i>	91
Figure 6.7 <i>Mixing of aerated concrete</i>	93
Figure 6.8 <i>Examples of aerated concrete specimens</i>	94
Figure 6.9 <i>Compression testing of cube specimens with instrumentation for measurement of longitudinal force and deformation as well as transverse deformation</i>	95
Figure 6.10 <i>Thermal conductivity test setup (insulation removed to show the specimens)</i>	96
Figure 6.11 <i>(A) Split tension test setup (B) failure mode</i>	97
Figure 6.12 <i>(A) Flexural test setup (B) failure mode</i>	97
Figure 6.13 <i>Sorption test specimens with one surface exposed to water</i>	98
Figure 6.14 <i>Compression test cube prior to (A) and after (B) failure</i>	99
Figure 6.15 <i>Compressive strength and density test results for different aerated concrete formulations</i>	99
Figure 6.16 <i>Flexural load-deflection behavior of the Mix #22 aerated concrete</i>	100
Figure 6.17 <i>Sorption versus square root of time for Mix #22 (A) and Mix #30 (B)</i>	101
Figure 6.18 <i>Entry and exit points of two projectiles shot at the same specimen</i>	102
Figure 7.1 <i>The first-generation sandwich composite specimen</i>	103
Figure 7.2 <i>Sandwich composite flexure test setup</i>	105
Figure 7.3 <i>Failure mode in flexure of the first-generation sandwich composite</i>	106
Figure 7.4 <i>Flexural load-deflection behavior of the sandwich composite</i>	107

Figure 8.1 <i>Primary modes of the indigenous sandwich composite structural behavior</i>	108
Figure 8.2 <i>The shear connector and web options for ensuring the integrated action of composite skins and the lightweight core in sandwich composites [111]</i>	109
Figure 8.3 <i>Chicken mesh as indigenous shear connector</i>	110
Figure 8.4 <i>Schematic depiction of the test specimen and loading condition for measurement of the interfacial shear strength</i>	110
Figure 8.5 <i>Interfacial shear test setup</i>	111
Figure 8.6 <i>Damage mechanism during shear failure of the ferrocement skin-aerated concrete core interface with shear connector</i>	112
Figure 8.7 <i>A simplified approach to interfacial shear stress calculation in four-point flexure testing of a sandwich composite panel with width (perpendicular to plane) of 300 mm</i>	113
Figure 8.8 <i>Schematic depiction of the sandwich composite flexure test component and loading condition</i>	113
Figure 8.9 <i>Production of the sandwich composite flexure test component</i>	114
Figure 8.10 <i>The indigenous sandwich composite panel</i>	114
Figure 8.11 <i>Long-span indigenous sandwich composite panel test setup</i>	115
Figure 8.12 <i>Failure mode of the long-span indigenous sandwich composite panel</i>	115
Figure 8.13 <i>The short-span indigenous sandwich composite panel test setup and failure mode</i>	116
Figure 8.14 <i>Typical load-deflection behavior of indigenous sandwich composite panels under out-of-plane loading</i>	116
Figure 8.15 <i>Schematics of the sandwich composite panel subjected to out-of-plane loading</i>	118
Figure 8.16 <i>Sandwich composite wall subjected to in-plane shear and gravity loads</i>	119
Figure 8.17 <i>The sandwich composite in-plane shear test component and loading condition</i>	119
Figure 8.18 <i>Interpretation of the diagonal compression test: stress at the center of the panel in Mohr's representation</i>	121
Figure 8.19 <i>Production of square sandwich composite component for performance of diagonal compression tests</i>	122
Figure 8.20 <i>Diagonal compression test setup, and failure mode of the indigenous sandwich composite</i>	123
Figure 8.21 <i>Load-deflection behavior of the indigenous sandwich composite panel subjected to diagonal compressive loading</i>	123

Figure 8.22 *Cutting of the indigenous sandwich composite using a circular saw with diamond blade*

125

INTRODUCTION

Use of locally available materials for construction of buildings offers important economic and sustainability benefits. The building systems designed to make maximum use of indigenous materials should still provide adequate safety, serviceability, energy-efficiency, and durability characteristics. Seismic, blast, impact and wind resistance are among the considerations in development of these building systems. The technology would have applications in sustainable and/or low-cost construction with locally available materials in both developed nations [1]. The new building systems would also improve the safety (e.g., earthquake and fire resistance), energy-efficiency and sustainability of dwellings which house a major fraction of the world population in developing nations [2].

Modern buildings are generally constructed with materials such as Portland cement concrete, steel, timber, pre-fabricated gypsum panels, masonry units, asphalt, plastics, polymer composites, and insulating foams. Building systems incorporating these materials are designed to meet structural safety, fire resistance, energy-efficiency, quality of life, and durability requirements. The prevalent indigenous materials in developing nations, including those in the tropical region of Africa, Sahel region of Africa and Middle East, include adobe, rammed earth, cob, stabilized soil, stone, brick, concrete block, lime, gypsum, natural pozzolans, biomass ash, vegetable fibers (and their fabrics/ropes), straw, bamboo, tree trunks/stems/leaves, corrugated sheets, ferrocement, and asphalt [2-34]. These indigenous construction materials are commonly used in the context of traditional building systems which provide basic shelter under regularly encountered load and environmental effects at minimum cost. Their inability to withstand extreme events (e.g., earthquakes and storms), however, has led to a significant disparity in death tolls caused by natural disasters in developing nations versus those in developed nations where modern building materials and systems are prevalent [35]. Traditional building systems are not generally prepared to withstand the blast and projectile impact effects [36].

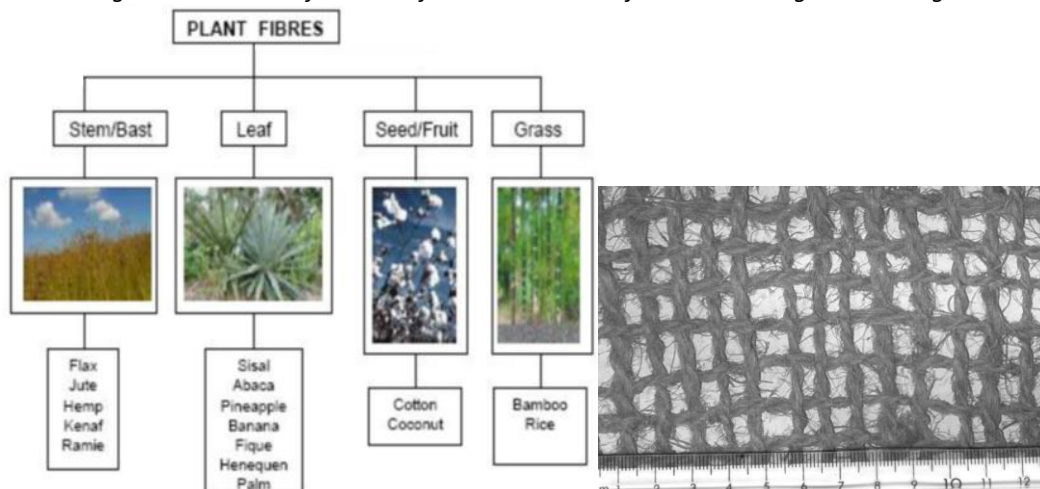
A robust approach is undertaken for scalable and reconfigurable construction of safe, sustainable, energy-efficient, economically viable, structurally efficient and durable building systems using indigenous materials and locally available resources in developing nations. This approach makes synergistic use of the following materials and principles:

- Inorganic binders which can be optionally formulated without Portland cement, and
 - use locally available materials (volcanic deposits, lime, soda ash, laterite clay, gypsum, etc.) [14, 18, 20, 37], and render binding effects relying primarily upon aluminosilicate hydrates or integrated carbonated lime and gypsum [37-39]
 - require limited quantities of water (in mix and for curing), and can use water of relatively low quality in mix [40, 41]
 - provide high rates of strength development for rapid construction [42]
 - suit utilization as binder in ferrocement [43-45], aerated concrete [46], and concrete for footing construction [47]
- Use of diverse locally available plant fibers (Figure 1.1a) as
 - reinforcing fabric (Figure 1.1b) to replace wire mesh in ferrocement [27, 28, 48]
 - yarn for shear transfer, and reinforcement of inorganic binders [49-53]
 - discrete reinforcement in inorganic binders [30, 50, 54, 55]
 - use as insulation layer in building walls and roof [21, 56]
- Development of sandwich composites comprising exterior layers (skins) of ferrocement made with indigenous binders and fabrics, and
 - Interior layer (core) of aerated concrete (Figure 1.2a) made with indigenous binders and indigenous foaming agents extracted from abundant plants [57] or animal proteins [58]
 - interior layers of locally available fibers (Figure 1.2b), where the sandwich composite provides a desired balance of thermal insulation, fire resistance and (with proper shear

stress transfer through the core) structural performance in roof and wall applications [19, 21-23, 59, 60]

- interior layers of adobe, rammed earth, cob and wood/bamboo, where the indigenous ferrocement layers render enhanced weathering resistance and structural performance in building wall and roof applications [6, 61]
- ferrocement webs acting as shear ties (Figure 1.2c), with either of core materials noted above
- Building systems comprising sandwich composite wall, roof and floor panels which are manually assembled (Figure 1.3a) and joined using the extended reinforcement of skins and locally applied indigenous binder (Figure 1.3b) to form building systems (Figure 1.3c) which can be tailored towards different loading and climatic conditions. These building systems can be designed to withstand extreme (blast, projectile penetration, earthquake, etc.) effects, which could require integration with an indigenous concrete footing. They can also be designed for common (gravity, wind) loads, yielding very lightweight buildings that could be feasibly supported on a layer of gravel in the targeted climatic conditions.

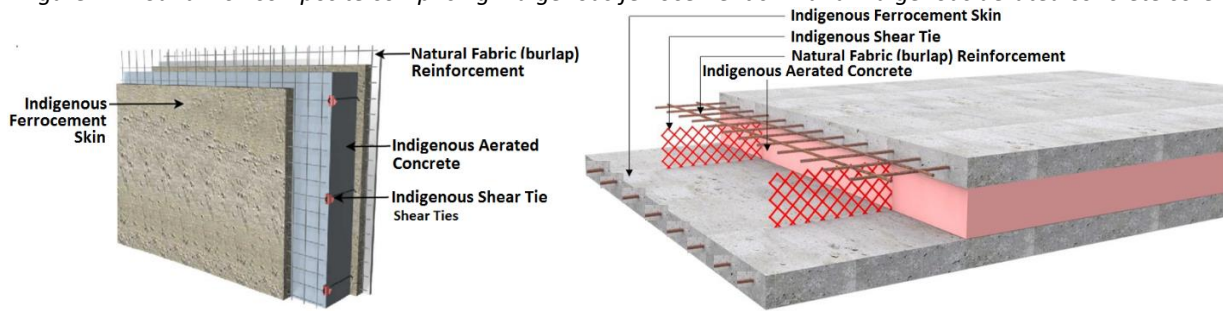
Figure 1.1 Natural fibers and fabrics used as reinforcement in organic building materials



(a) Categories of natural (plant) fibers [62]

(b) Example of natural fiber (coir) fabric [63]

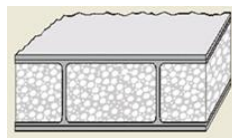
Figure 1.2 Sandwich composite comprising indigenous ferrocement skin and indigenous aerated concrete core



(a) Sandwich composite with aerated concrete core



(b) Sandwich composite with natural fiber core

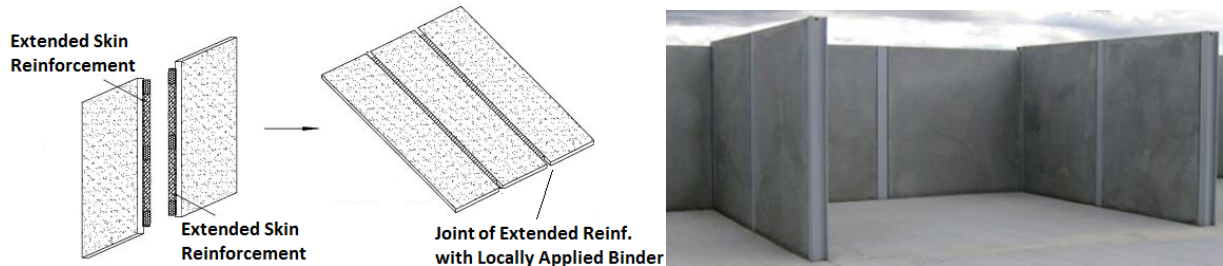


(a) Ferrocement web (and skin)

Figure 1.3 Manual assembly and joining of indigenous sandwich composite panels into building systems



(a) Manual assembly of sandwich composite panels into a building system



(a) Joining of sandwich composite panels

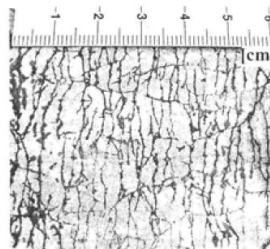
Figure 1.3(cont'd)



(b) Building systems comprising indigenous sandwich composite panels

Ferrocement skins constitute the primary load-bearing constituents of the building system introduced above. One key advantage of ferrocement, which is of particular value in dissipating seismic and blast energy, is its inherent ability to mitigate localization of damage through multiple cracking (Figure 1.4) [64]. This feature, which results from the high specific surface area, volume fraction and mechanical interlocking of reinforcement in ferrocement, enables effective mobilization of large structural volumes for distributed energy dissipation. The binder in ferrocement can be applied manually after placement of the reinforcement. Simple equipment have also been adopted in developing nations for high-speed spray application of the inorganic binder in ferrocement construction [19]. Applications of ferrocement and sandwich composites incorporating them go beyond buildings, and cover many other systems which are required to sustain life. Examples include water tanks and pipes.

Figure 1.4 The distributed damage mechanism of ferrocement [65]



The goal of the Phase I project reported herein was to verify the merits of the principles introduced above for design and construction of safe, serviceable, sustainable, energy-efficient and economically viable building systems with materials and resources that are locally available in developing nations. The following tasks were executed in Phase I project.

- Identify the indigenous materials, specifics of the building systems, and the relevant design requirements.
- Develop design methods for the selected building system.
- Formulate, synthesize and characterize representative building materials using indigenous raw materials and resources.
- Design, fabricate and characterize major building subcomponents using indigenous materials and resources.
- Assess the viability of the proposed approach to rapid construction of safe and serviceable building systems with indigenous materials and resources.

DEVELOPMENT OF INDIGENOUS CEMENTITIOUS BINDERS

2.1 Introduction

An indigenous cementitious binder is the primary material devised for construction of buildings and infrastructure systems, which meet modern safety, serviceability, sustainability and quality of life requirements using indigenous materials. The indigenous binder enables development of building components and systems with a desired balance of structural (load-bearing) and protective (projectile penetration resistance and energy absorption) qualities, moisture barrier and weathering resistance, thermal insulation, fire resistance, and health and sustainability attributes.

Alternative cementitious binders were devised considering the availability of mineral resources in different regions of Africa and Middle East (and elsewhere). These inorganic binders make use of some abundant (indigenous) mineral resources either directly or with minimal processing as raw materials. The mineral resources selected for use in Phase I project include volcanic deposits, laterite clay, gypsum, lime, and soda ash. Figure 2.1 shows major deposits of gypsum, soda ash, limestone and potash in Africa and the Middle East. Figures 2.2, 2.3 and 2.4 show major sources of volcanic deposits, laterite clay and (sodium carbonate-rich) natron, respectively, in Africa and the Middle East. Sodium sulfate (thenardite) and its hydrate (mirabilite) are other common minerals that could contribute to development of alternative (indigenous) cementitious binders.

Figure 2.1 Major deposits of sodium carbonate (soda ash), soluble potassium salts (potash), gypsum, limestone and other mineral deposits in Africa and Middle East

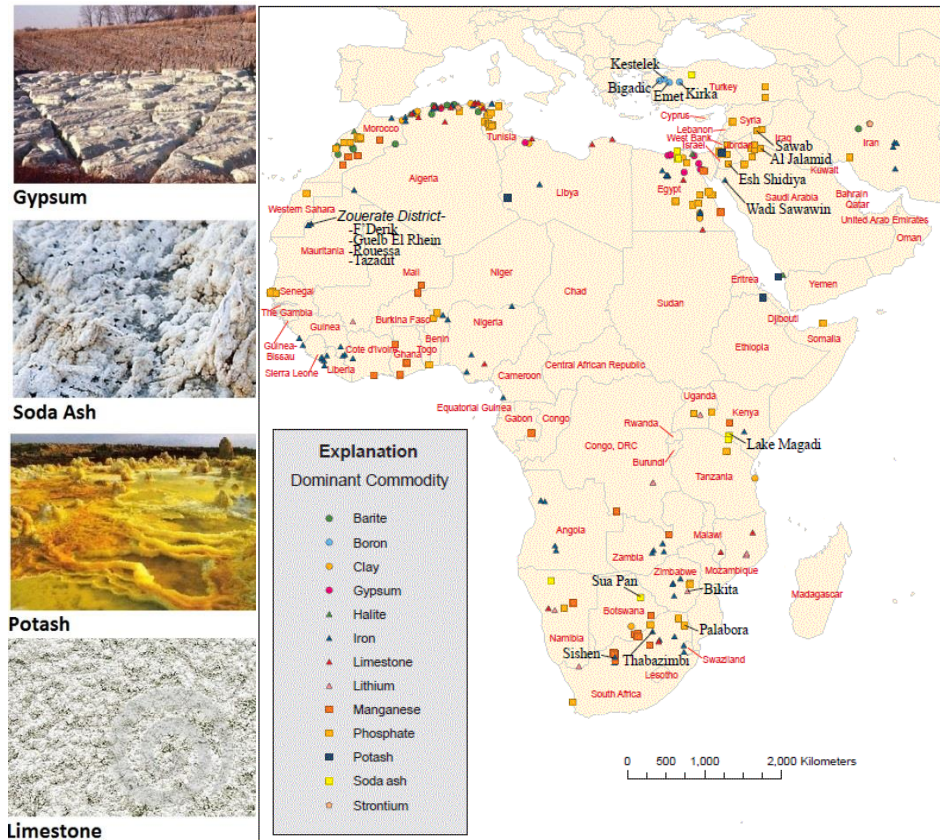


Figure 2.2 Active volcanoes of Africa and Middle East

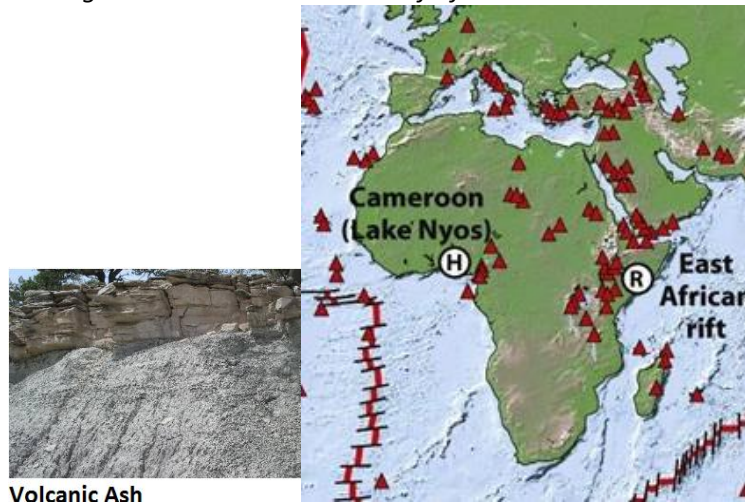


Figure 2.3 Laterite clay deposits in Africa and Middle East

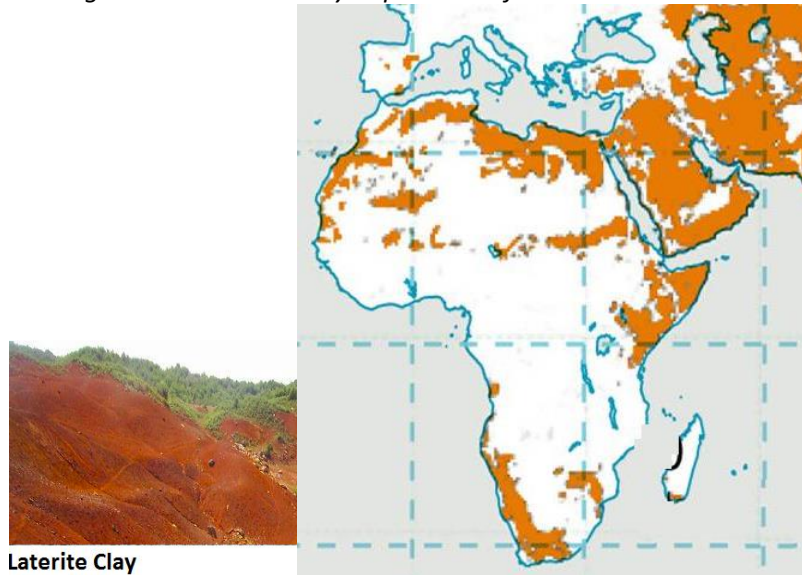
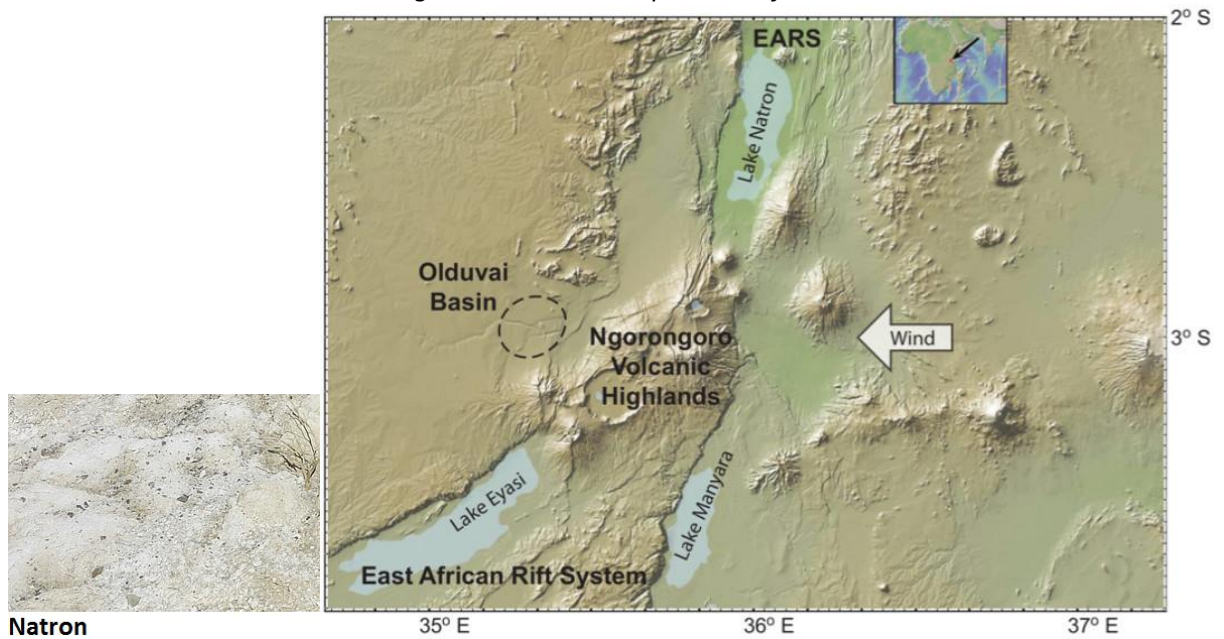


Figure 2.4 Natron deposits in Africa



In addition to natural mineral deposits, some abundant plants can also be sources of chemicals which, as additives, add value to various cementitious materials. For example, citric acid constitutes up to 70% of the sap of such succulent plants as agave (Figure 2.5a) and opuntia (Figure 2.5b); acetic acid can be extracted from capsella boursapastris (Figure 2.5c), oxalic acid from rumex (Figure 2.5d), and saponin (a

foaming agent) from caryophyllaceae (Figure 2.5e), sapindus (Figure 2.5f), aceraceae, hippocastanaceae, gynostemma pentaphllum and ginseng.

Figure 2.5 Plants which are sources of chemical additives for enhancement of cementitious Materials



Some historic infrastructure systems provide convincing evidence that abundant natural resources can, with minimal or no processing, be transformed into high-performance construction materials. Clay followed by gypsum are the simplest binders used in ancient buildings [68-71]; their moisture-sensitivity, however, prompted the historic search for hydraulic cements. While Portland cement eventually emerged as the prevalent hydraulic binder, simpler and more sustainable formulations were developed in history, some of which are now being revisited as replacements for Portland cement [72]. Some surviving ancient buildings point at the improvements made in the moisture resistance and durability of gypsum binders via introduction of calcium and aluminum compounds which transform into moisture-resistant calcite and ettringite [68]. Parallel with gypsum, lime produced by calcination of limestone emerged as another binder used in construction of ancient buildings [71]. Improvements were made over time in the mechanical performance and moisture resistance of lime by introduction of organic matter. This concept was developed in southern Syria and northern Jordan in the period from 6500 BC to 700 BC (Figure 2.6a). Breakthrough developments in this field, which led to development of hydraulic binders matching or even surpassing the moisture resistance, durability and mechanical qualities of today's Portland cement, occurred when lime was combined with pozzolans such as volcanic deposits or various forms of calcined clay (e.g., brick dust or crushed brick) [68, 73]. Pantheon in Rome used this class of historic concrete (Figure 2.6b). Calcined clay was later used as a replacement for volcanic ash, to be blended with lime and

other additives to yield hydraulic binders with higher levels of moisture resistance and strength. More reactive (e.g., laterite) clays were also used in combination with soda ash and lime to produce hydraulic binders for concrete [74]. One can consider these classes of historic hydraulic binders as the forerunners of modern geopolymer binders [72].

Figure 2.6 Examples of ancient buildings employing different classes of hydraulic binders



(a) lime-based concrete building in Middle-East (b) Pantheon in Rome made with volcanic ash/lime-based concrete

Development of hydraulic binders using abundant indigenous raw materials is a key step in this project towards development of indigenous building components and systems. Three categories of hydraulic binders were developed in Phase I project using combinations of raw materials that are available broadly in the targeted geographic areas. These three categories of hydraulic binders are: (i) calcium aluminosilicate-based binders; (ii) refined gypsum-based binders with improved moisture resistance; and (iii) alkali aluminosilicate-based binders. These three indigenous binder categories and the progress made in Phase I project towards their development are reviewed in the following.

2.2 Calcium Aluminosilicate-Based Binders

2.2.1 Introduction

Volcanic deposits are aluminosilicates with different calcium and iron oxide contents and different degrees of crystallinity. Table 2.1a presents the ranges of chemical compositions covered by the volcanic deposits classified as pumice and lava. The reactivity of volcanic deposits varies with their degree of

crystallinity which, depending on the cooling rate and mineralogy, can range from as low as 10% to more than 60% [75]. The pumice used in this project was subjected to x-ray fluorescence (XRF) spectroscopy for the purpose of elemental analysis. The results presented in Table 2.1b indicate that the pumice used here is rich in SiO₂ and K₂O; its Al₂O₃ content is near the lower range expected for pumice. The volcanic deposits introduced in Table 2.1 are essentially aluminosilicates (the primary constituents of the earth crust) with varying contents of calcium/magnesium and iron compounds as well as alkalis. Such aluminosilicate compounds can be transformed into inorganic, cementitious binders via dissolution and precipitation steps using different activators [76]. Various indigenous activators could be used with volcanic deposits, including soda ash and natron (in combination with lime) which, due to their higher alkalinity, offer greater capabilities for dissolution of volcanic ash and precipitation of inorganic binders including alkali aluminosilicate hydrate. In order to expand the range of indigenous ‘cementitious’ binders for broad regions of Africa, Middle East and the rest of the world, the more challenging task of activating volcanic deposits with lime [77] was undertaken in Phase I project.

Table 2.1 Ranges of chemical compositions (wt.%) covered by pumice and lava [78, 79], and the chemical composition of the pumice used in the project obtain via XRF spectroscopy

	SiO ₂	Al ₂ O ₃	Fe ₂ O ₃ +FeO	MgO	CaO	Na ₂ O	K ₂ O	TiO ₂	MnO
Pumice	54-72	11-20	2-10	0.5-4	2-9	2-5	0.5-10	0.3-0.8	0.15-0.25
Lava	50-52	12-14	10-15	4-7	9-11	2-2.5	0.4-0.7	2-3.5	0.15-0.25

(a) Ranges of the chemical compositions of pumice and lava

	Fe ₂ O ₃	SiO ₂	Al ₂ O ₃	CaO	TiO ₂	K ₂ O	MgO
Pumice	3.6	68.4	11.1	2.7	-	9.5	1.4

(b) Chemical composition of the pumice used in this project

Aluminosilicates such as volcanic deposits can, in a lime solution, undergo dissolution and precipitation processes which yield a 3D calcium aluminosilicate hydrate (C-A-S-H) structure (Figure 2.7) with desired binding attributes [80]. The 3D structure of C-A-S-H provides it with enhanced mechanical, stability and

binding qualities when compared with calcium silicate hydrate (C-S-H), the primary binder in Portland cement concrete (Figure 2.8) or Portlandite ($\text{Ca}(\text{OH})_2$) formed in the course of Portland cement hydration (Figure 2.9). It should be noted that lime activation of aluminosilicates also generates C-S-H via the reaction shown in Figure 2.8. Successful lime activation of volcanic deposits is projected to yield a cementitious binder comprising a combination of C-A-S-H and C-S-H (see Figures 2.7 and 2.8).

Figure 2.7 Reaction of dissolved aluminosilicate with lime to form calcium aluminosilicate hydrate (C-A-S-H)

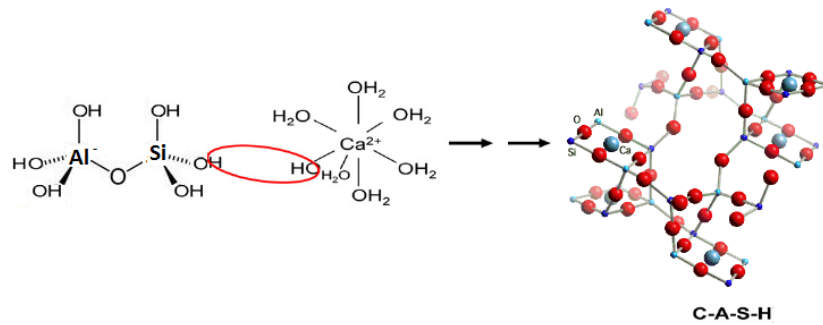


Figure 2.8 Hydration of dissolved calcium silicate to form calcium silicate hydrate (C-S-H)

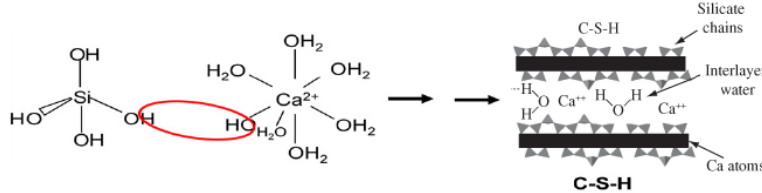
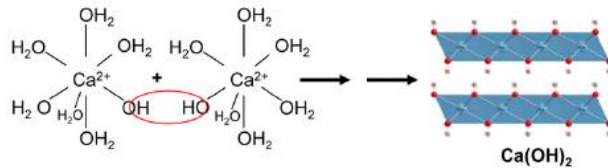


Figure 2.9 Formation of Portlandite in the course of hydration of calcium silicates in Portland cement



2.2.2 Experimental Program

Volcanic powders of pumice and red lava (Figure 2.10) with less than 125 μm particle size were used in this investigation. Lime and quick lime were used as activators. The weight ratio of volcanic powder: lime was mostly in the range of 0.7-0.77: 0.3-0.23 [81, 82], and the water/binder ratio ranged from 0.6 to 0.74 for achieving a workable fresh mix. Soda ash (Na_2CO_3) was used as an additive in some mixtures. Soda ash as well as sodium sulfate (another natural material that is indigenous to the targeted geographic areas)

have been used as accelerators for lime-aluminosilicate binders [83]; it is feasible that they raise the alkalinity of the solution, thereby enhancing the dissolution of aluminosilicate precursors and formation of precipitate binders (C-A-S-H and probably N,C-A-S-H) [84] which benefit both the short- and long-term properties of the inorganic binder. Gypsum was the other additive used in some mixture for enhancing the dissolution of alumina-bearing compounds. Natural sand was used as filler in the lime/volcanic powder mixtures. The mix designs considered in this investigation are introduced in Table 2.2. These mixtures were prepared using a mortar mixer. Set time was measured following ASTM C191 procedures. The fresh mixtures were molded into 50-mm cubes, demolded after 24 hours (during which they were stored under wet burlap), sealed and moist-cured for 3 days. The specimens were then stored at 50% relative humidity and room temperature for compression testing at 7 and (in some cases) 14 days of age. Specimens made with Mixes No. 8, 9 and 10 in Table 2.2 were sealed continuously after demolding, and tested at 7 days of age once they were removed from sealed bags.

Figure 2.10 The volcanic powders used in the experimental work



(a) Pumice



(b) Red lava

Table 2.2 The mix designs (weight ratios) considered for volcanic deposit/lime binders

Mix	Volcanic Deposit Type	Volcanic Deposit	Lime	Additive	Water	Sand
1	Red Lava	0.7	0.3	0	0.6	3
2	Red Lava	0.7	0.3	0.07 (sodium sulfate)	0.6	3
3	Pumice	0.7	0.3	0	0.6	3
4	Pumice	0.7	0.3 (quick lime)	0	0.6	3
5	Pumice	0.7	0.3	Soda Ash: lime 1:1	0.6	3
6	Pumice	0.7	0.3	0.04 (soda ash)	0.6	3
7	Pumice	0.7	0.3 (quick lime)	0.04 (soda ash)	0.6	3
8	Pumice	0.77	0.23 (quick lime)	0.04 (soda ash)	0.71	3
9	Pumice	0.77	0.23 (quick lime)	0.04 (soda ash) + 0.1 (gypsum)	0.71	3
10	Pumice	0.2	0.2 (quick lime)	0.6 (gypsum)	0.74	3

Scanning electron microscope observations were made on the indigenous binders using a JEOL JSM-6610LV scanning electron microscope (JEOL Ltd., Tokyo, Japan). For the purpose of scanning electron microscopy, the binder specimens were gold-coated in an Emscope Sputter Coater model Sc 500 (Ashford, Kent, England) purged with Argon gas. Figure 2.11 shows the scanning electron microscope and the sputter coater analyzer used in this investigation. For EDX analysis, uncoated samples were tested and analyzed under low vacuum.

Figure 2.11 The scanning electron microscope (left) and the Emscope Sputter Coater analyzer (right) used in the project



The mineralogy of indigenous binders was analyzed via x-ray diffraction (XRD) using a Bruker D8 daVinci diffractometer equipped with Cu x-ray radiation operating at 40 kV and 40 mA (Figure 2.12). The XRD method allows for evaluation of the degree of crystallinity and identification of the crystalline phases in raw materials and binders. For the purpose of XRD analysis, the ground sample was packed tightly into the sample cup so that the powder was level. Peak intensities were obtained by counting, with a Lynxeye detector, every $0.05^\circ 2\theta$ /min. For this purpose, the sample was placed in a PVMA sample holder, and was rotated at a rate of 5° /min. Powder XRD was carried out at a reflection angle range of $2\theta = 10\text{--}80^\circ$. Qualitative analysis of XRD patterns yielded the mineral phases present in ash samples.

Figure 2.12 X-ray Diffractometer



2.2.3 Test Results and Discussion

Mixtures with red lava did not set within 24 hours, and thus were not evaluated any further. Pumice mixtures activated with lime ($\text{Ca}(\text{OH})_2$) had set times exceeding 24 hours, and thus do not suit high-speed

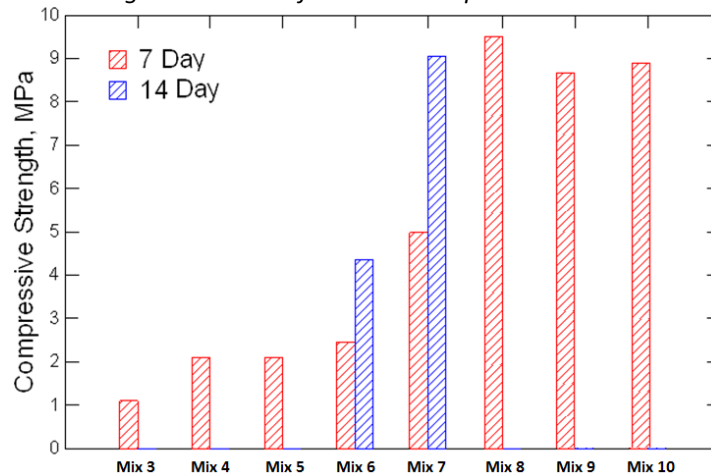
production. The use of quick lime (CaO) reduced the set time to about 135 minutes, and the addition of soda ash further reduced set time to below 1 hour. The set times achieved with quick lime (without and with soda ash) meet the ASTM C1157 performance-based specifications for hydraulic cements.

The compressive strength test results (average of 2 specimens at each age) are summarized in Figure 2.13.

Mix No. 8, with soda ash used as an additive, is observed to provide the highest compressive strength.

The 7-day compressive strength approaching 10 MPa provided by this formulation is acceptable, per ASTM C1157, for the low heat of hydration (LH), moderate heat of hydration (MH) and high sulfate resistant (HS) hydraulic cements. It should be noted that the mix design used here is unfavorable to compressive strength when compared with that recommended by ASTM C1157 (and ASTM C109). Minor heat treatment of pumice, in milder conditions than those used for production of lime, is expected to significantly benefit the strength and other properties of the pumice-based indigenous cement.

Figure 2.13 Compressive strength test results for volcanic deposit-based mortars at 7 and 14 days of age



(Mix 7 in Table 2.2). Calcium hydroxide crystals could be identified within a matrix comprising (based on XRD data presented later) amorphous constituents and crystalline carbonate compounds. Figure 2.15 shows the EDX spectrum of the pumice-based binder. Calcium, carbon silicon and aluminum appear as the primary elements of this binder, with small amounts of sodium, magnesium and iron detected. The XRD spectra for pumice and the binder based on it are presented in Figure 2.16. Pumice, as a raw material,

is observed to be highly amorphous, with an amorphous hump at 2θ 15-35 degrees. Analysis of the XRD data indicated that pumice has a degree of crystallinity of less than 15%. The pumice-based binder embodies different crystalline peaks, associated with calcite, portlandite, and iron carbonate hydroxide.

Figure 2.14 SEM image of the pumice-based indigenous binder.

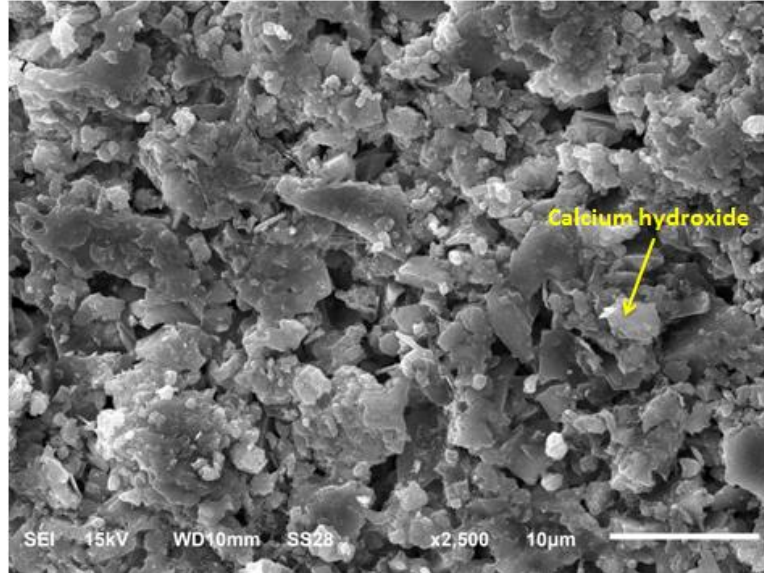


Figure 2.15 Secondary electron images and EDS spectrum of the pumice-based binder

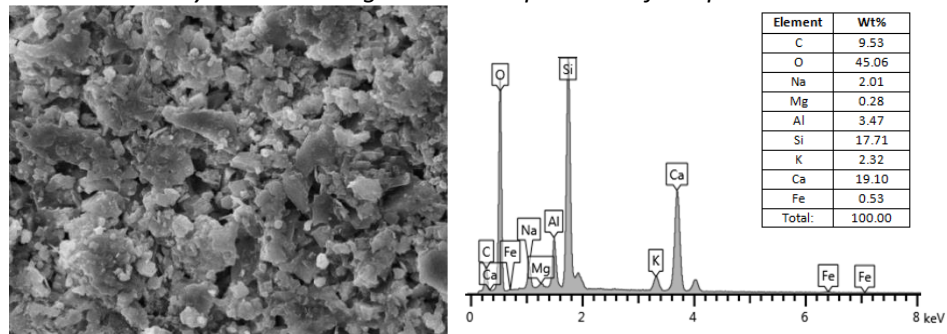
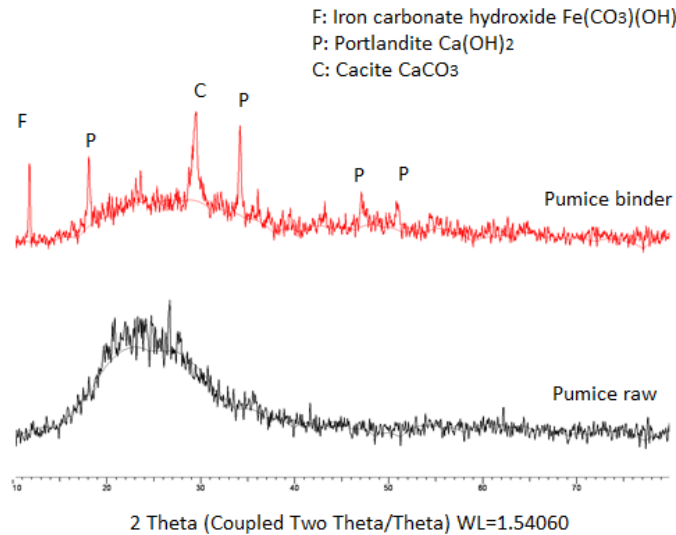


Figure 2.16 X-ray diffraction spectra for pumice and the pumice-based binder



2.3 Refined Gypsum-Based Binders with Improved Moisture Resistance

2.3.1 Introduction

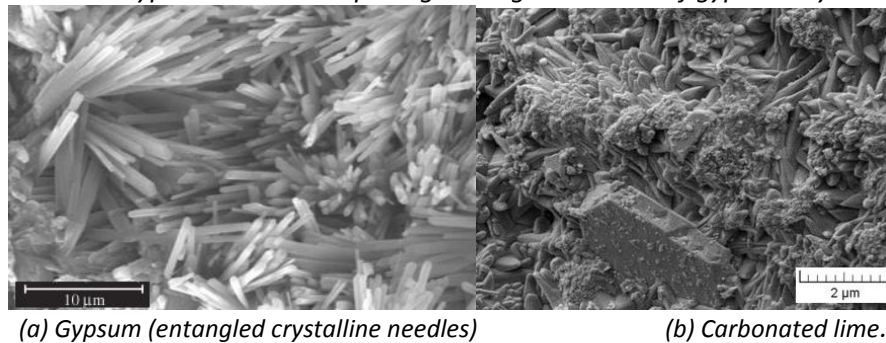
The abundance of gypsum natural resources, and the simplicity and sustainability of its conversion into a hydraulic binder (via dehydration at 170°C versus processing of Portland cement at 1480°C) explain the popularity of gypsum as an inorganic binder across the world [85]. Gypsum binders are entangled needles of gypsum crystals ($\text{CaSO}_4 \cdot 2\text{H}_2\text{O}$) (Figure 2.17a) produced via a solution-mediated phase transition of calcium hemihydrate ($\text{CaSO}_4 \cdot 0.5\text{H}_2\text{O}$). The cohesion and mechanical strength of the solid are due to both entanglement and inter-crystalline interaction. Water adsorption, however, weakens the bonds between faces of crystals; the water adsorbed at grain boundaries also allows crystals to slip against each other under stress [86]. Various strategies have been developed for enhancing the moisture and weathering resistance of gypsum binders. Developments that are relevant to construction with indigenous raw materials in Africa and Middle East include:

1. Blending of calcium hemihydrate with lime (another indigenous binder produced via calcination of limestone) to produce Portlandite ($\text{Ca}(\text{OH})_2$) in addition to gypsum. Reaction of Portlandite with

the carbon dioxide in air yields, over time, stable calcite (CaCO_3) shown in Figure 2.17b. Formation of calcite enhances the mechanical performance, density, barrier attributes, moisture resistance, durability and bond strength (to aggregates) of the gypsum matrix [87, 88].

2. Blending of calcium hemihydrate with sources of aluminosilicate (e.g., volcanic deposits) and lime to produce calcium aluminosilicate hydrate and calcium aluminate hydrate for enhancing the engineering properties of gypsum [89].
3. Use of additives such as citric acid (from indigenous plant extracts) and sodium carbonate (indigenous soda ash or natron) to yield desired set retardation and moisture resistance effects by altering the crystallization kinetics and the morphology of gypsum crystals [85, 86, 90, 91].

Figure 2.17 Gypsum binder comprising entangled needles of gypsum crystals [92]



2.3.2 Experimental Program

The option selected for development of stable hydraulic binders based on gypsum emphasized enhancement of gypsum using lime (to transform into calcite) and citric acid or sodium carbonate (to control set time and further enhance material properties). The mix designs considered in the experimental program are introduced in Table 2.3. Natural sand satisfying the ASTM C33 requirements for fine aggregate was the sand used in these mixtures.

Table 2.3 Mix designs (weight ratios) evaluated for development of stable hydraulic binders based on gypsum.

Mix	CaSO ₄ .½H ₂ O	Lime	Additive	Water	Sand
1	1	0	0	0.6	3
2	0.8	0.2	0	0.6	3
3	0.5	0.5	0	0.6	3
4	0.8	0.3	0.025 (Na ₂ CO ₃)	0.6	3
5	0.8	0.2	0.05 (Na ₂ CO ₃)	0.6	3
6	0.8	0.2	0.02 (Citric Acid)	0.6	3

The gypsum-based mortar mixtures were prepared in a mortar mixer. The fresh mix was molded into 50 mm cubes, and demolded after 24 hours. The specimens were stored at 50% relative humidity and room temperature; given the time constraints of Phase I project, they were subjected to compression tests at 7 days of age. Two specimens were tested with their moisture content stabilized at 50% relative humidity, and two other were tested in wet condition after 24 hours of immersion in water at room temperature. Longer-term storage would have enhanced carbonation of lime which benefits the strength and moisture resistance of the specimens.

2.3.3 Test Results and Discussion

The seven-day compressive strength test results (average of two specimens) for air-dried and wet specimens are presented in Figure 2.18. It should be noted that early-age testing of specimens is particularly unfavorable to mixtures incorporating lime, because reaction of lime with carbon dioxide generates calcite over time, which enhances the mechanical performance and moisture resistance of these specimens. The 7-day test results presented in Figure 2.18 indicate that: (i) introduction of lime (at hemihydrate: lime ratio of 0.8: 0.2) yields beneficial effects (Mix 1 vs. Mix 2); (ii) increasing the lime

content (from hemihydrate: lime ratio of 0.8: 0.2 to 0.5: 0.5) adversely influences the early-age strength of the gypsum-based binder (Mix 2 Vs. Mix 3); (iii) sodium carbonate is not an effective additive for enhancing the early-age strength of gypsum-based binders (Mix 2 Vs. Mixes 4 & 5); (iv) citric acid is an effective additive for enhancing the early-age strength of gypsum-based mortars, with a 7-day compressive strength of about 11.5 MPa achieved in air-dried condition with gypsum: lime: citric acid weight ratios of 0.8: 0.2: 0.02; and (v) the viable gypsum-based mixtures developed in the project (Mixes 2 & 6) experienced about 50% loss of compressive strength upon saturation, noting that further generation of calcite via reaction of Portlandite with the carbon dioxide in air is anticipated to enhance the moisture resistance of these mixtures over time. The gypsum-based mix selected based on these test results comprises gypsum: lime: citric acid at weight ratios of 0.8: 0.2: 0.02. The 7-day compressive strength of 11.5 MPa exceeds those specified by ASTM C1157 for the low heat of hydration (LH), moderate heat of hydration (MH) and high sulfate resistance (HS) hydraulic cements.

Figure 2.18 Compressive strength test results for gypsum-based mortars at age of 7 days

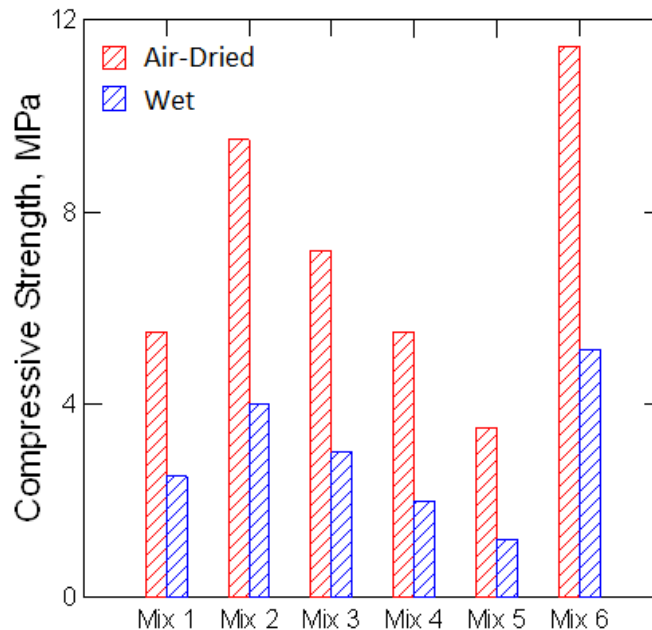


Figure 2.19 shows an SEM image depicting the surface topography of the refined gypsum-based binder (Mix 6 in Table 2.3). The needle-like structure of gypsum as well as the calcium hydroxide crystals and the

sand particles can be identified in this image. The SEM image indicates that gypsum is the binding material in the young gypsum-lime mortar. The SEM image and EDX analysis depicted in Figure 2.20 indicate that, besides calcium and sulfur, carbon is also a primary element which could point at carbonation reactions which would be even more prevalent at later ages. The resulting carbonates enhance the binding qualities and the moisture stability of the refined gypsum-based binder.

Figure 2.21 shows the XRD spectrum of the refined gypsum-based binder. Gypsum is observed to be the primary crystalline phase. Small amounts of calcite and portlandite were also detected in the binder. The purpurine hydrate peak is probably indicative of the use of citric acid as an additive (for set retardation and enhancement of moisture resistance) in this refined gypsum-based binder.

Figure 2.19 SEM image of the mortar with refined gypsum-based binder

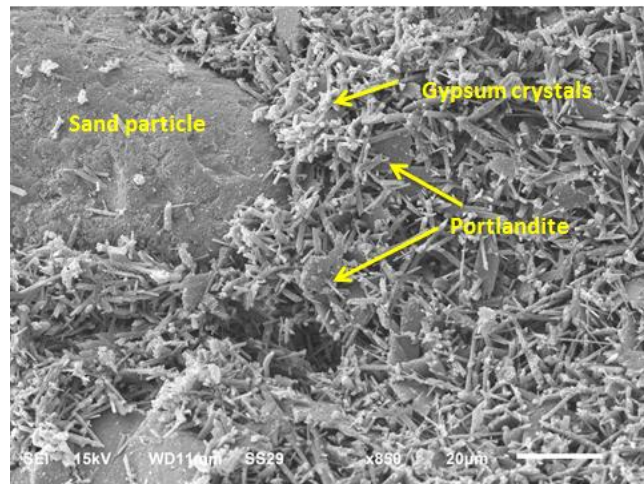


Figure 2.20 Secondary electron images and EDS spectrum of the refined gypsum-based binder

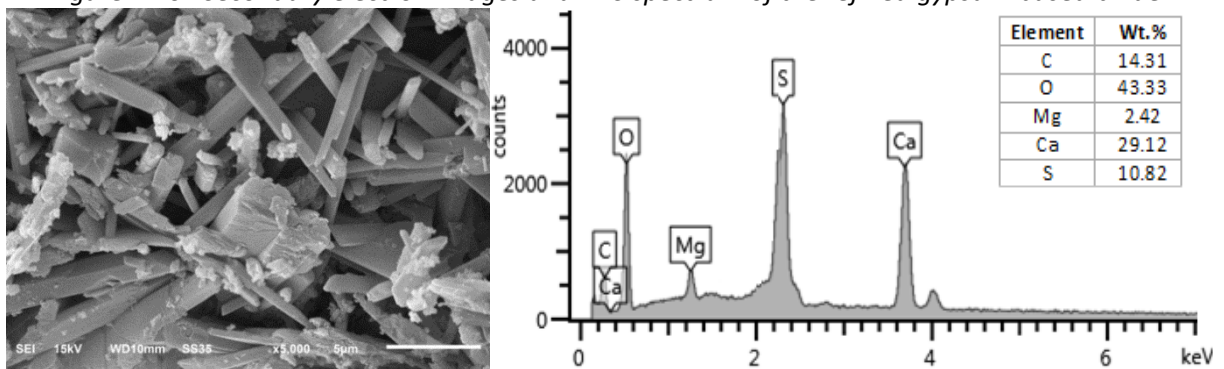
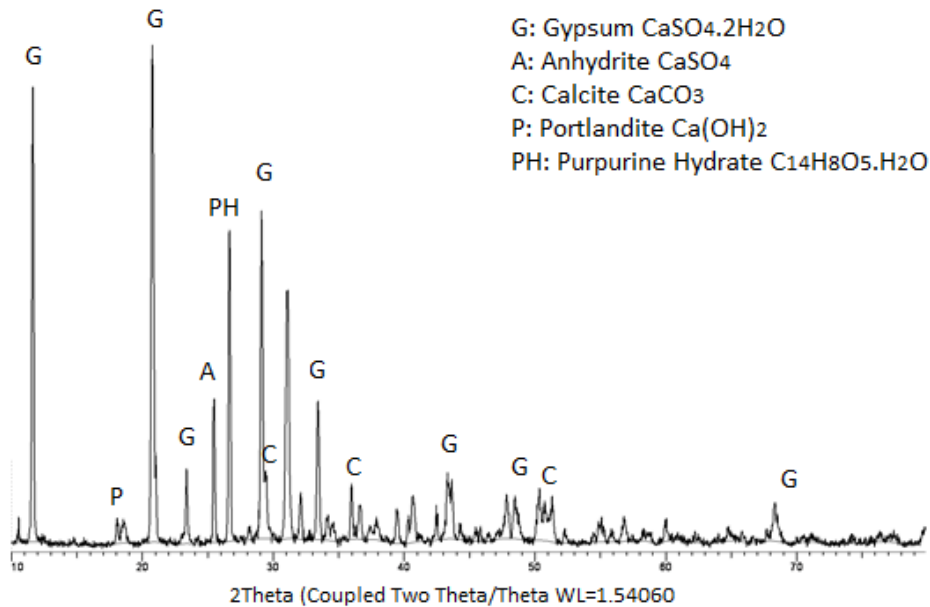


Figure 2.21 X-ray diffraction spectrum of the refined gypsum-based binder



2.4 Alkali Aluminosilicate-Based Binders

2.4.1 Introduction

Calcined (thermally treated) clays act as aluminosilicate precursors which, upon exposure to alkaline solutions, transform into a high-performance inorganic binder (alkali aluminosilicate hydrate) [93]. Metakaolin is a calcined clay which can be transformed into alkali aluminosilicate hydrate (geopolymer) via: (i) alkalination and formation of tetravalent Al in the side group silage $-\text{Si-O-Al}(\text{OH})_2\text{-Na}^+$ (Figure 2.22a); (ii) alkaline dissolution via attachment of the base OH^- to the silicon atom, enabling it to extend its valence sphere to the penta-covalent state (Figure 2.22b); (iii) cleavage of the siloxane oxygen in Si-O-Si through transfer of electron from Si to O, forming intermediate silanol Si-OH on the one hand and basic siloxo Si-O^- on the other hand (Figure 2.22c); (iv) further formation of silanol Si-OH groups and isolation of the ortho-sialate molecule, the primary unit in geopolymerization (Figure 2.22d); (v) reaction of the basic siloxo Si-O^- with the sodium cation Na^+ , and formation of Si-O-Na terminal bond (Figure 2.22e); (vi a) condensation between ortho-sialate molecules, reactive groups Si-O-Na and aluminum hydroxyl OH-Al , with production of NaOH and formation of cyclo-tri-sialate structure, liberating the alkali NaOH which

reacts again to enhance polycondensation into Na-poly(sialate) nepheline framework (Figure 2.22f); (vi b) condensation, in the presence of waterglass (soluble Na-polysiloxonate, between di-siloxonate Q₁ and ortho-sialate molecules, reactive groups Si-O-Na, Si-OH and aluminum hydroxyl OH-Al- to form ortho-sialate-disiloxo cyclic structure and liberate NaOH for further reaction (Figure 2.22g); and (vii) further polycondensation into Na-poly(sialate-disiloxo) albite framework with typical feldspar crankshaft chain structure (Figure 2.22h).

Figure 2.22 Transformation of calcined kaolinite clay (metakaolin) into a high-performance geopolymer binder using NaOH without or with waterglass [93]

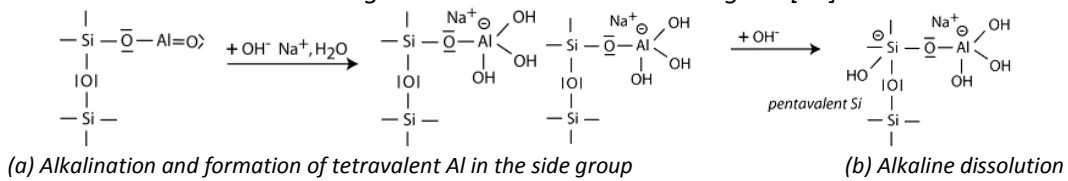
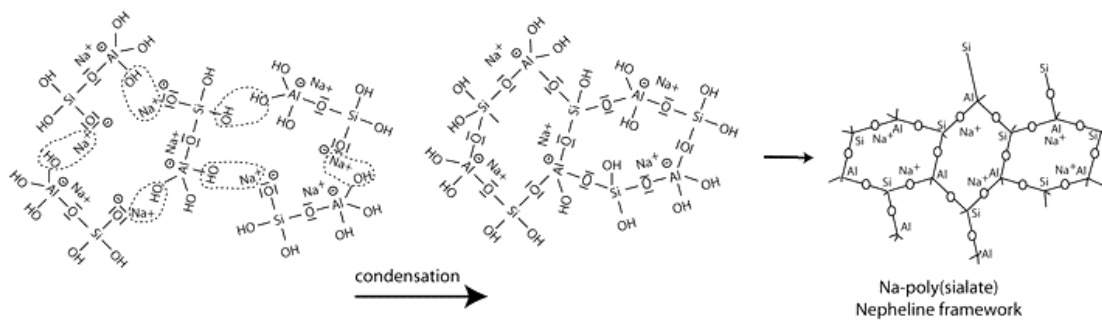
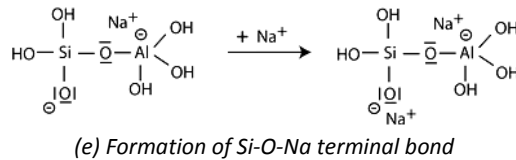
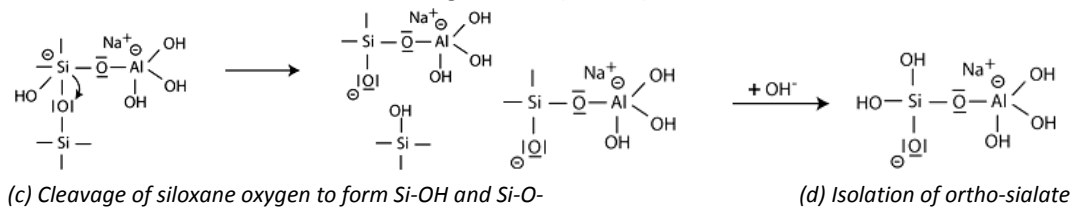


Figure 2.22(cont'd)



ferromagnetic minerals, removal of silica and base (Na₂O, K₂O, MgO), and concentration of iron and magnesium oxides. Tropical weathering is a prolonged process of chemical weathering. Laterite soils generally occur at hillsides, and therefore provide excellent extraction sites for extensive use in various construction activities. Due to their inherent binding qualities, laterite soils can harden in-situ, where they can be cut into brick-like shapes for building construction [94, 95]. A typical chemical composition of laterite clay is presented in Table 2.4a. The laterite clay used in this investigation was subjected to x-ray fluorescence (XRF) spectroscopy, the results of which are presented in Table 2.4b. Laterite clays have a relatively low pH (~5 at a liquid-to-solid ratio of 2.5) [96]. The mineral constituents of laterites include kaolinite, hematite, goethite, quartz, ilmenite and limestone [97].

Table 2.4 Typical chemical composition (wt.%) of laterite clays [95-97], and the chemical composition of the laterite clay used in this investigation obtained via XRF spectroscopy.

Oxide	SiO ₂	Al ₂ O ₃	Fe ₂ O ₃	Na ₂ O	K ₂ O	TiO ₂	MgO	P ₂ O ₅	SO ₃	LOI
Weight%	20-45	10-30	10-45	0.1-2.5	0.1-2	1.5-4.5	0.05-0.1	1-15	1-5	5-18

(a) Typical chemical composition of laterite clays

	Fe ₂ O ₃	SiO ₂	Al ₂ O ₃	CaO	TiO ₂	K ₂ O	MgO
Laterite clay	42.4	28.1	22.9	0.40	3.2	0.23	-

(b) Chemical composition of the laterite clay used in this investigation

Laterite soils can be described as Fe₂O₃-Al₂O₃-SiO₂-H₂O matrices made from kaolinite in which a high portion of Al³⁺ is replaced with Fe²⁺ or Fe³⁺. This replacement induces important transformation of the structure of kaolinite, which imparts reduced crystallinity and increased vulnerability to chemical attack. There is an antagonism between hematite (Fe₂O₃) and kaolinite (Al₂Si₂O₅(OH)₄) in the matrix of laterite; corrosion of kaolinite is followed by a complete destruction of the crystal, giving place to hematite or goethite (α-FeO(OH)) organized into thin lamellar structures; the crystals of Al-rich hematite or Al-rich goethite formed maintain a clear trace of the shapes of former kaolinite platelets. It is postulated that, in the deep layers of laterites fed by Fe³⁺ solutions, the protons necessary to dissolve kaolinite are generated

by a reaction similar to the oxidation-hydrolysis step of ferrolysis [97]. The protons released by the precipitation of 1 cm³ of ferrihydrite may solubilize about 1.5 cm³ of kaolinite. On the other hand, the precipitation of ferrihydrite from Fe³⁺ solutions has been shown to be accelerated by interfaces such as those of silica or kaolinite particles. In the presence of kaolinite, the release of Al³⁺ species into solution and the precipitation of Fe³⁺ hydroxide are two simultaneous processes. The increase in iron accumulation leads initially to the production of nodule nuclides that progressively grow with the iron content and, finally, laterite 'concrete' is formed with amorphous silica which acts as binder. The induration of laterite soils is specific to tropical regions. The fluctuation of temperature and humidity, grain size, kinetics of precipitation and equilibrium conditions (involving the activity of water) are factors controlling the formation of indurated matrices of laterites. Mottles and concretions with essentially hematite and goethite are of very small size in early states of induration; at later states, the goethite phase evolves into well-formed crystals of about 1 μm size. However, hematite and goethite are commonly present as small particles of 10 nm size due to the predominant effects of dehydration and water activity. Rapid release of Fe and low concentrations of organic compounds favor hematite formation; high concentrations of organic compounds, on the other hand, favor goethite formation. For kinetic reasons, goethite is more common than hematite; hematite, once formed, does not rehydrate to form coarse goethite. The driving force in migration and accumulation of iron is suggested to be the difference in size of pores, which tends to be accentuated as concretion proceeds. The primary minerals are generally not fully dissolved, but partially transformed into secondary minerals which are more stable. The iron content of laterites enhances the kinetics of the transformation of kaolinite (the structure of which is already affected). The disordered structure of laterites enhances their dissolution in highly alkaline solutions, offering the potential to yield high-performance inorganic (geopolymer) binders. In tropical regions, laterite generally occurs at the surface. Hence, unlike clays which are covered in most cases by laterites or other soils, extraction of laterites is less detrimental to the environment. It should be noted that laterites cover a

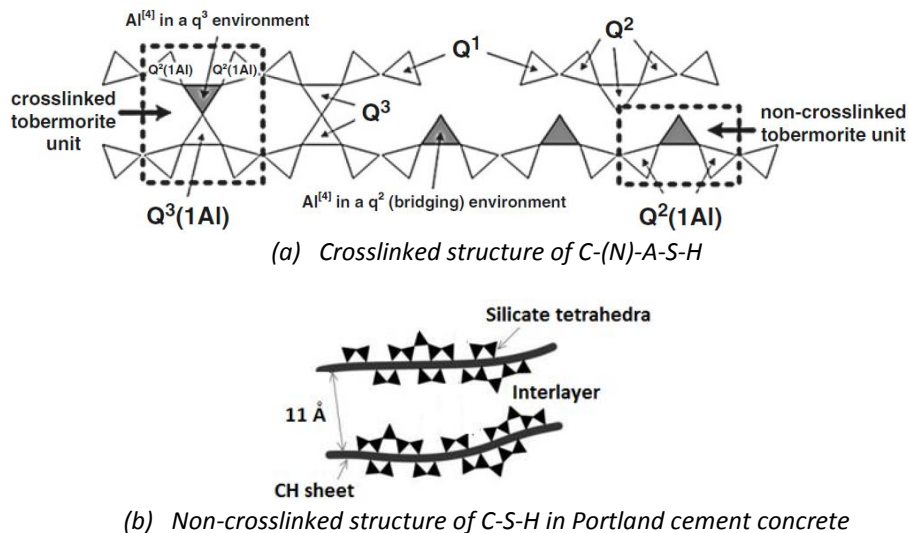
range of aluminosilicates in which iron accumulation could be at the stage of nodule nuclides, nodules or larger and coarser iron crusts. Their reactivity and behavior during the key polycondensation step of geopolymerization should be linked to the degree of iron accumulation. Considering the goethite-diaspore and hematite-corundum profiles as solid solutions of crystallized iron-rich oxihydroxides, substitution of Al^{3+} in goethite (Al-goethite) and hematite (Al-hematite) are additional factors defining the particular features of laterites and aluminosilicates which may affect their geopolymerization. The reactivity of laterites in the course of geopolymerization would also be influenced by their particle size distribution, Si/Al ratio, relative amorphous/vitreous phase contents, the form of iron (ferrihydrite, hematite or goethite), and the degree of laterization [97].

The approach taken in this project uses laterite clay as a chemically active aluminosilicate precursor that can be used for production of an inorganic binder (geopolymer). This approach is an extension of lime stabilization of laterite clay which induces cation exchange as well as chemical reactions that form minerals such as calcium silicate hydrate, calcium aluminate hydrate and calcium aluminosilicate hydrate to impart binding effects [96, 98]. Lime stabilization of laterite clay relies upon chemical phenomena that are similar to those explained earlier for lime/volcanic deposit systems. Use of laterite clay in this investigation as an aluminosilicate precursor for geopolymerization is based on the hypothesis that the structure of kaolinite in laterite soil is already dissolved/destroyed by iron accumulation, and is thus amenable to alkali activation and polycondensation. The resulting inorganic (geopolymer) binder is expected to comprise alkali aluminosilicate hydrate with Al partially replaced with Fe.

The option of lime activation (similar to that practiced with volcanic deposits) could also be applied to laterite clay. It only requires consideration of the retarding effects of iron (hydr)oxide which tends to coat kaolinite particles [96]. The option exercised here, however, involves alkali activation of laterite clay, which expands the selections of indigenous cementitious binders. This option could better suit laterite soils which, depending on their specific characteristics, could be less reactive than volcanic deposits. There

are also structural differences between lime-activated aluminosilicates which yield calcium aluminosilicate hydrate (C-A-S-H) and calcium silicate hydrate (C-S-H) versus alkali activated aluminosilicates which yield alkali aluminosilicate hydrates (e.g., N-A-S-H). The structure of N-A-S-H tends to be more ordered than that of C-A-S-H. Gels of C-A-S-H type are likely to have a structure comparable to co-existing 11 and 14 Å tobermorite-like phases. A structural model has been developed to describe these gels based on the constraints inherent to the crosslinked and non-crosslinked structures of different tobermorite-like units (Figure 2.23a), noting that crosslinking is a distinct feature which distinguishes C-(N)-A-S-H from the non-crosslinked tobermorite-lime C-S-H gels (Figure 2.23b) in Portland cement concrete. Crosslinking is accomplished via AlO_4 tetrahedra, and improves the properties of C-A-S-H and N-A-S-H when compared with C-S-H.

Figure 2.23 Schematics of crosslinked and non-crosslinked tobermorite which represent the generalized structures of the C-(N)-A-S-H and C-S-H type gels [42]



2.4.2 Experimental Program

Laterite clay (Figure 2.24) was acquired from Planet Clay; its primary constituents are SiO_2 (32.5 wt.%), Al_2O_3 (29%) and Fe_2O_3 (24%). The indigenous alkalis used for activation of laterite clay were soda ash and natron, used alone or in combination with lime or quick lime. The mix proportions considered in this

experimental work are introduced in Table 2.5. Mortar mixtures were prepared with natural sand-to-binder ratio of 3: 1 and water/laterite ratio of 0.65. Activators were dissolved in the mixing water, and added to laterite clay. The binder was mixed with the activator solution in a mortar mixer for one minute to produce a consistent paste. Natural sand was then added, and mixing was continued for two more minutes. Fresh mortar mixtures were molded into 50 mm cubes, which were kept under wet burlap for 24 hours. They were then sealed in bags for three days, after which they were stored at 50% relative humidity and room temperature until the test age of 7 days. Mixes 10 and 11 were sealed upon demolding, and tested at 7 days of age soon after removal from the sealed bag. A typical cube specimen is shown in Figure 2.25. It should be noted that the geopolymerization process reproduces moisture, and thus sealing is adequate for curing of these inorganic binders. Final geopolymer binders incorporate relatively small quantities of chemically bound water when compared with Portland cement hydrates. Some samples were, after demolding, exposed to 110°C over 24 hours in an oven in an effort to demonstrate relatively low-temperature (chemical) brick production via alkali-activation of laterite clay. These 'alkali-activated brick' specimens were then stored at 50% relative humidity and room temperature until the test age of 7 days. It should be noted that all raw materials used in the laterite clay-based binders are indigenous to the targeted geographic areas. Calcined laterite clay has not been introduced so far. This raw material is available in developing nations in the form of brick dust, can be obtained by grinding brick, or can be produced by subjecting laterite clay to a heat treatment (calcination) condition that can be easily performed using facilities that are commonly available in developing nations for limestone calcination (decarbonation) to produce lime.

Figure 2.24 Laterite clay



Table 2.5 The mix designs (weight ratios) considered for production of alkali aluminosilicate hydrate binders using laterite clay and indigenous alkali activators.

Mix	Laterite Clay	Soda Ash (or Natron)	Lime	Additive	Water	Sand
1	0.9	0.1 (soda ash)	0	0	0.59	3
2	0.75	0.25 (soda ash)	0	0	0.49	3
3	0.83	0.1 (soda ash)	0.07	0	0.54	3
4	0.745	0.15 (soda ash)	0.105	0	0.48	3
5	0.745	0.15 (soda ash)	0.105	0.05 hemihydrate	0.48	3
6	0.775	0.15 (soda ash hydrate)*	0.075 (quick lime)	0	0.50	3
7	0.625	0.25 (natron)	0.125 (quick lime)	0	0.41	3
8	0.8	0.1 (soda ash)	0.1 (quick lime)	0	0.65	3
9	0.7	0.15 (soda ash)	0.15 (quick lime)	0	0.52	3
10	0.59	0.12 (soda ash)	0.12 (quick lime)	0.17 (calcined laterite)**	0.41	3
11	0.51	0.117 (soda ash)	0.117 (quick lime)	0.256 (calcined laterite)**	0.37	3

* $\text{Na}_2\text{CO}_3 \cdot 10\text{H}_2\text{O}$

** Laterite clay subjected to 500°C over 3 hours after blending with 30 wt.% soda ash

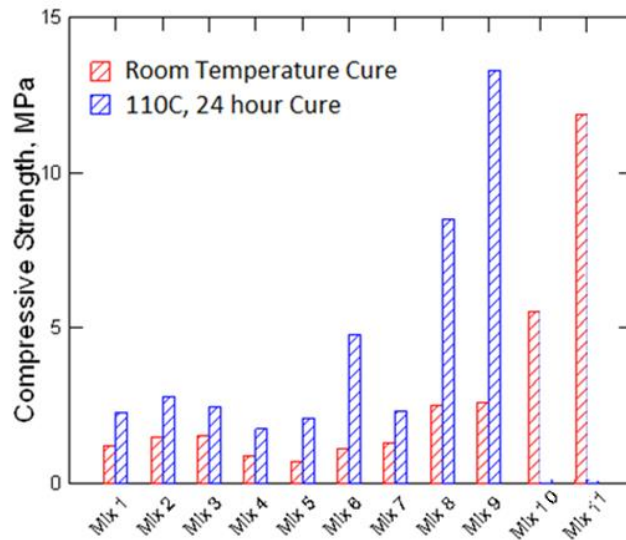
Figure 2.25 An alkali-activated laterite clay cube specimen.



2.4.3 Test Results and Discussion

The 7-day compressive strength test results are summarized in Figure 2.26. Each result is the average of two cube specimens. Mix 11 with laterite calcined at a relatively low temperature, after blending with 30 wt.% soda ash, constituting 30% of the total laterite content produced 7-day compressive strength of 12.1 MPa (when cured at room temperature). This 7-day compressive strength exceeds those specified by ASTM C1157 for the low heat of hydration (LH), moderate heat of hydration (MH) and high sulfate resistance (HS) hydraulic cements. The 3-day compressive strength of Mix 11 (not shown in Figure 2.26) was 9.2 MPa, which meets the ASTM C1157 requirements for above types of hydraulic cement, and is also very close to satisfying the 3-day strength requirement of 10 MPa for General Use (GU) hydraulic cement. It should be noted that the mix design used for measurement of compressive strength in ASTM C1157 favors achievement of higher strengths than that used here. Hence, with further refinement, the indigenous cementitious material (Mix 11) developed in the project using laterite clay, soda ash and lime promises to meet the ASTM C1157 requirements for General Use (GU) hydraulic cement.

Figure 2.26 Seven-day compressive strength test results for alkali-activated laterite clay (Mix 9 tested at 3 days of age).



An SEM image depicting the surface topography of the laterite-based binder (Mix 9) is presented in Figure 2.27. The SEM image with EDX analysis of this binder is presented in Figure 2.28. The key elements of laterite, activators (soda ash and quick lime) and the additive (hemi-hydrate) are apparent in Figure 2.28, including aluminum, silicon, iron, sodium, calcium and carbon. Figure 2.29 shows EDX spectra of the outer (near-surface) and inner regions of the laterite-based binder. In this particular binder, a gradient structure develops with a high sodium concentration near surface. This could be explained by the migration (leaching) of sodium cations towards surface, where they could carbonate and form sodium carbonate; this phenomenon is similar to efflorescence in Portland cement concrete. This observation indicates that the transformation process depicted in Figure 2.22 has not been completed through the polycondensation step which yields a stable moisture-resistant binder. This analysis was performed with Mix 9 in Table 2.5, and Mixes 10 and 11 were devised to overcome this problem.

Figure 2.27 SEM image of the laterite-based binder.

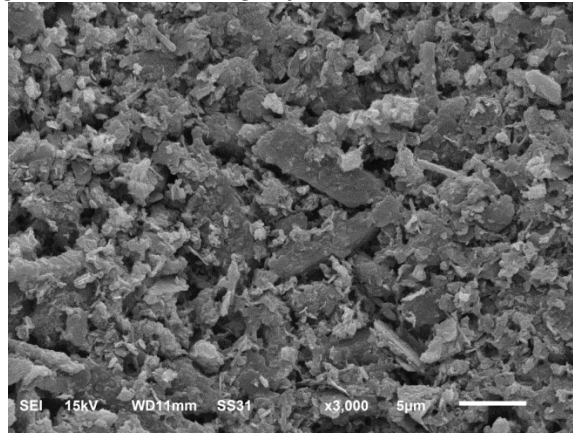


Figure 2.28 Secondary electron images and EDS spectrum of the laterite-based binder.

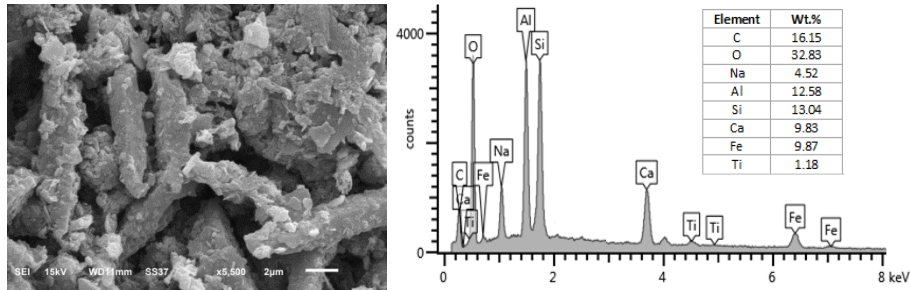


Figure 2.29 EDX spectra for outer and inner surfaces of laterite-based binder.

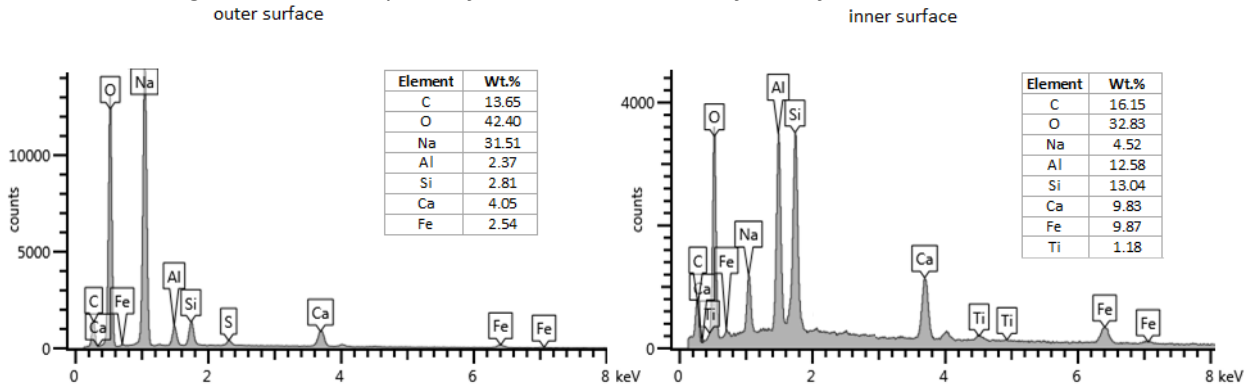
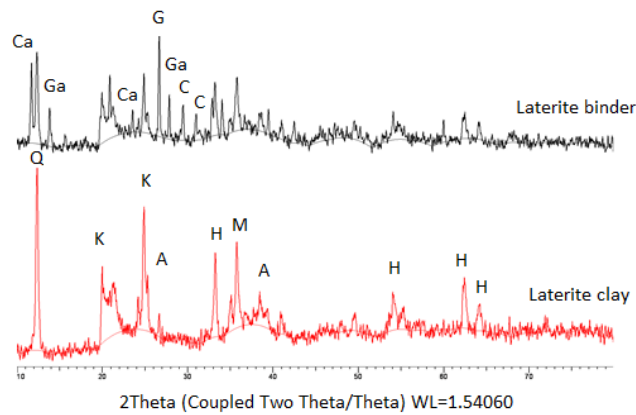


Figure 2.30 shows the XRD patterns of laterite clay and the laterite-based binder. These XRD spectra indicate that quartz, kaolinite and hematite are the main crystalline phases of laterite clay. Anatase and

magnesioferrite were also detected as minor constituents. The degree of crystallinity of laterite was found to be 56%. Upon processing of laterite into laterite-based binder, new peaks of calcium aluminocarbonate hydrate, calcium aluminosilicate hydrate, calcite and gaylussite appear. These findings are consistent with the intention of producing a binder dominated by aluminosilicate hydrate and carbonate constituents; alkali aluminosilicate hydrate, however, tends to be amorphous and thus is not detected in XRD analysis.

Figure 2.30 X-ray diffraction spectra for laterite and the laterite-based binder.

Q: Quartz SiO ₂	A: Anatase TiO ₂	G: Gismondine CaAl ₂ SiO ₈ .4H ₂ O
C: Calcite CaCO ₃	H: Hematite Fe ₂ O ₃	Ga: Gaylussite Na ₂ CO ₃ .CaCO ₃ .5H ₂ O
Ca: Ca ₄ Al ₂ O ₆ CO ₃ .11H ₂ O	M: Magnesioferrite MgFe ₂	K: Kaolinite Al ₂ SiO ₂ O ₅ (OH) ₄



Important Note - The credits to this entire section must be given to Faris Matakah and Weerasiri

IDENTIFICATION AND CHARACTERIZATION OF INDIGENOUS REINFORCEMENT SYSTEMS

3.1 Introduction

The indigenous inorganic, cementitious binders developed in the project require reinforcement to attain the tensile strength and toughness attributes which enable development of efficient structural systems. Fabrics made of natural (e.g., jute, sisal, kenaf) fibers (Figure 3.1a) are readily available in the targeted geographic areas. Hexagonal wire netting (chicken mesh) (Figure 3.1b) is also an option across the developing (and developed) nations. These indigenous reinforcement systems suit production of ferrocement, a thin-sheet reinforced cement product with a distinct balance of qualities that can be processed, using unskilled labor, into structurally efficient configurations (Figure 3.2) [61].

Figure 3.1 Indigenous reinforcement systems



(a) Natural fabric (burlap)

(b) Chicken mesh

Figure 3.2 Ferrocement trowel, spray and precast production.



3.2 Identification of Indigenous Reinforcement Systems

Natural fabric (burlap) that can be potentially used as reinforcement in ferrocement can be produced using a host of abundantly available plant fibers (Figure 3.3). The location maps of some common plant fibers (Figure 3.4) confirm their availability in Africa, Middle East and elsewhere. Given the time

constraints of Phase I project, jute fabric (burlap) was selected for development of the indigenous building modules in Phase I project. Indigenous textile industries in Africa and Middle East can process natural fibers into yarn (Figure 3.5a) and then fabric (Figure 3.5b). The resulting fabric (burlap) as well as chicken mesh are considered in this project as indigenous reinforcement for production of ferrocement.

Figure 3.3 Some abundantly available plant fibers [99].

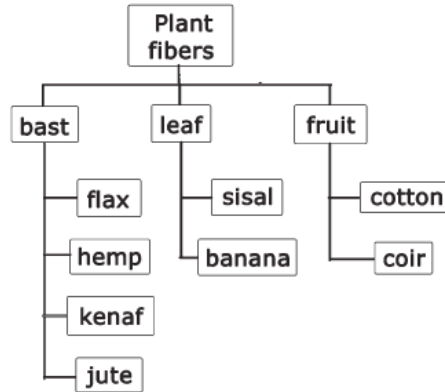
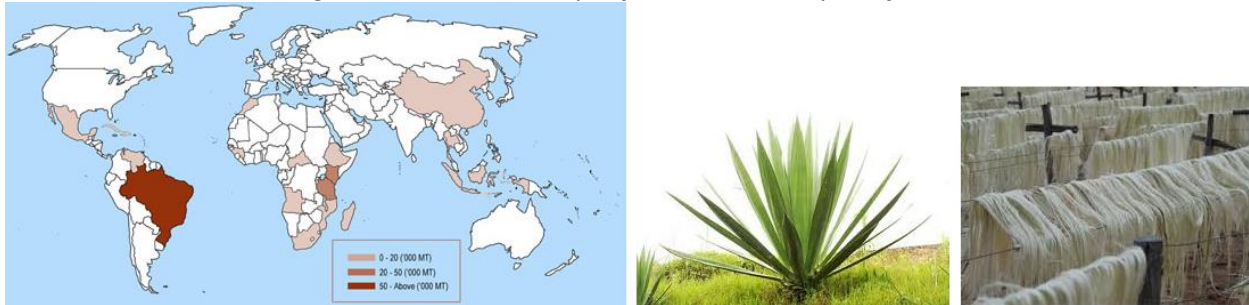


Figure 3.4 Location maps of some common plant fibers.

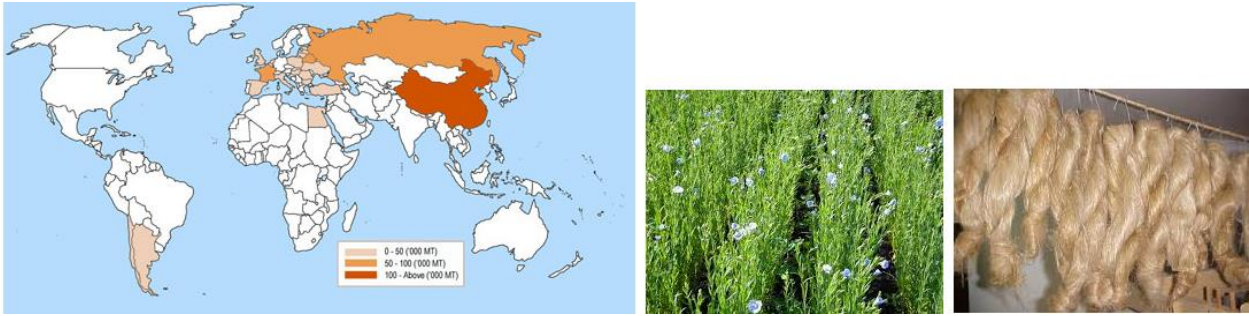


(a) Sisal



(b) Jute

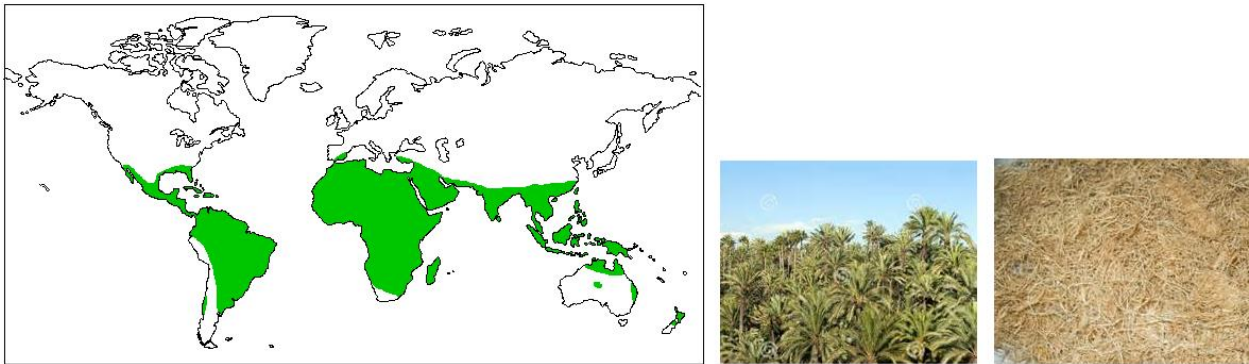
Figure 3.4(cont'd)



(b) Flax

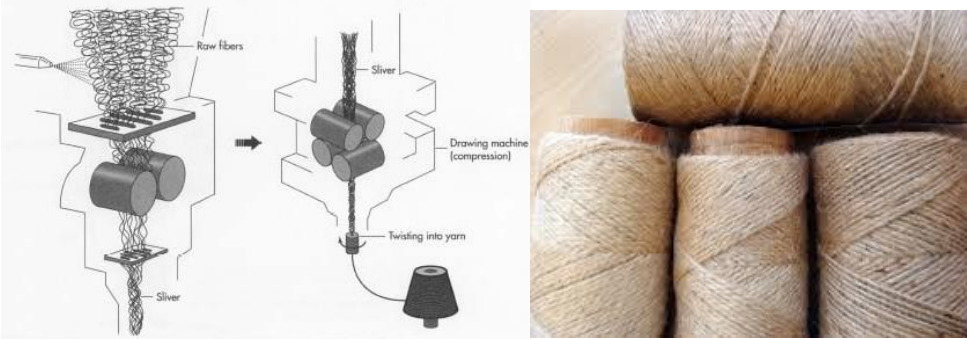


(c) Coir



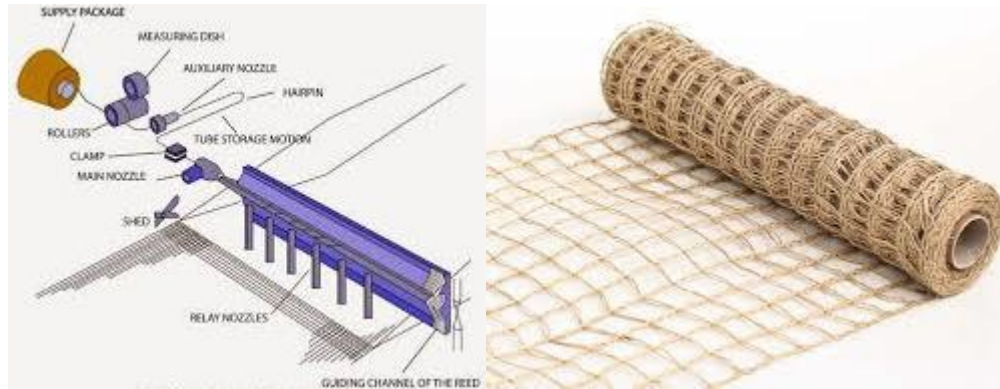
(d) Palm

Figure 3.5 Processing of natural plant fibers into yarn and fabric.



(a) Processing of vegetable fibers into sliver and yarn

Figure 3.5(cont'd)



(b) Processing of yarns into fabric

3.3 Experimental Program

After preliminary screening of a number of natural fabrics, two jute fabrics (burlaps) as well as a commonly available chicken mesh (Figure 3.6) were selected for use in Phase I project. The chicken mesh was made of wires with 1.5 mm average diameter; the hexagonal mesh openings had an average dimension of 25 mm in the direction along which the wires were more aligned. The chicken mesh was purchased from a local hardware store. The 'Jute 1' and 'Jute 2' burlaps shown in Figure 3.6 had square openings of 1.5 and 3 mm, respectively; the corresponding yarn diameters were 1.2 and 0.9 mm, respectively. The 3-mm opening of the 'Jute 2' natural fabric probably makes it more suitable for use as reinforcement in ferrocement. This is because a larger opening prevents the burlap from filtering larger (sand) particles of the mortar used as matrix in ferrocement. In the 'Jute 1' burlap, yarns in perpendicular directions were adhered at their junctures; the 'Jute 2' burlap, on the other hand, comprised woven yarns (which were not adhered together). The jute burlaps were purchased from the A.K. Trading Company via Amazon. The average cross-sectional area per unit width of chicken mesh, 'Jute 1' and 'Jute 2' were 0.071, 0.75 and 0.21 mm² per mm of width. It should be noted that natural fiber yarns (which comprise fabrics) are made of fibers with air space between them. The cross-sectional area of fabrics thus comprises both solid fibers and the spacing between them.

Figure 3.6 The jute burlaps and the chicken mesh selected for use in Phase I project.



(a) General view



(b) Chicken mesh

(c) Jute 1 burlap

(d) Jute 2 burlap

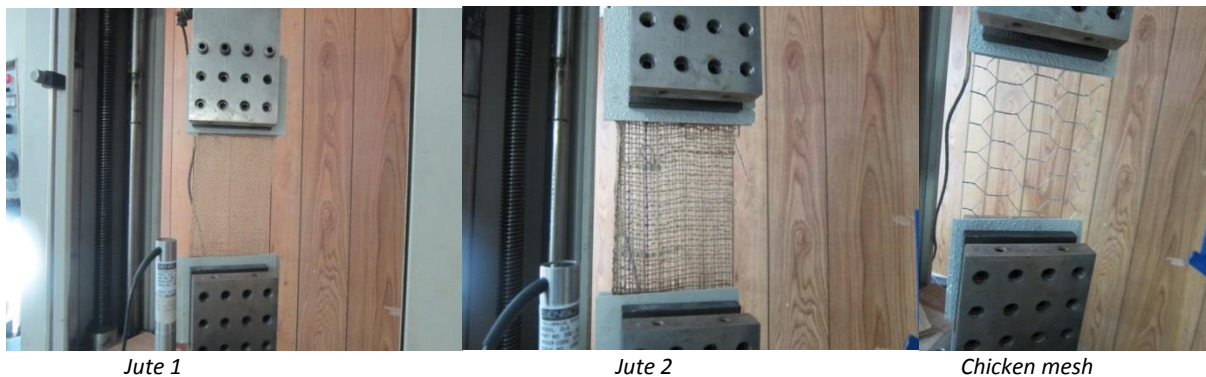
The indigenous reinforcement systems selected for use in ferrocement were characterized in Phase I project by subjecting them to tension tests. The tension test specimens are shown in Figure 3.7a; two chicken mesh specimens were needed in order to apply tension to the mesh in two perpendicular directions. The specimen dimensions were chosen to include a minimum number of hexagonal units of chicken mesh [100]. The tension test specimens were 285 mm long and 115 mm wide. For the purpose of end-gripping the jute burlap (and chicken mesh), after few trials, wooden plates were chosen, which were adhered to the fabric or mesh using the epoxy resin 862 and the Pro-set hardener at 3:1 weight ratio. The tension test procedures followed the guidelines provided in the literature [101]. Tension tests were performed on a screw-driven Instron test system with 7,000 N capacity. Figure 3.7b shows the chicken mesh and jute burlap test specimens installed in the Instron test system. Tension tests were performed

at a displacement rate of 0.2 mm/min; a load cell and a deflection transducer were used to collect the tensile load and deformation test data.

Figure 3.7 Fabric tension test specimens and setup



(a) Tension test specimens of jute burlaps and the chicken mesh in two perpendicular directions



(b) Fabric specimens installed in the tension test system

In addition to the 'Jute 1' and 'Jute 2' burlaps shown in Figure 3.6, jute and sisal yarns (Figures 3.8a and 3.8b, respectively) were also subjected to tension tests in order to gain a better understanding of the tensile behavior of different natural fiber yarns. These yarns are assemblies of aligned and twisted fibers (see Figure 3.5), and their diameter is subject to some variation along length [101]. The diameter of each yarn was measured using an optic microscope (Figure 3.9) at five points along the length [102]. The average diameters of the jute and sisal fiber yarns considered in this investigation were 1.57 and 1.16 mm, respectively. The fiber yarns were subjected to tension tests (Figure 3.10) in a servovalve-controlled

hydraulic test system at a displacement rate of 0.2 mm/min. A load cell and a displacement transducer were used to collect the load and deflection data throughout the test.

Figure 3.8 Natural fiber yarns



Figure 3.9 Optic microscope image of the jute fiber yarn

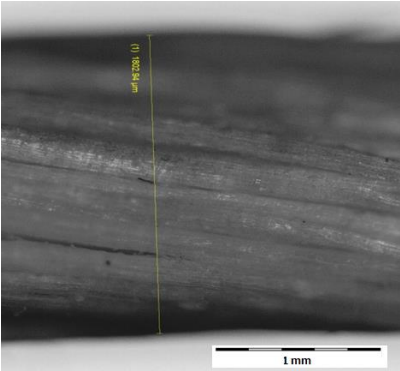


Figure 3.10 The single yarn tension test setup



3.4 Test Results and Discussion

Typical tensile load-deflection and stress-strain behavior of jute and sisal fiber yarns are presented in Figures 3.11 and 3.12, respectively. Tensile deformation of both yarns initiates with a low-modulus

behavior which could, at least partly, be attributed to the realignment and tightening of fibers within the yarn at early stage of tensioning. Beyond this state, both jute and sisal yarns exhibit a linear behavior up to the peak load where sisal yarns ruptured but jute yarns exhibited yielding prior to rupture. The average values of tensile strength, maximum strain at rupture and elastic modulus (beyond the initial state of low-modulus deformation) for jute and sisal yarns are summarized in Table 3.1. Yarns are assemblies of natural fibers; they enable practical use of natural fibers in large structures. Similar to wood, the bulk mechanical properties of yarns are a fraction of the corresponding fiber properties [99]. The tensile strength and elastic moduli of jute and sisal yarns measured here are about 20% and 15%, respectively, of the corresponding fiber properties. The strains at failure of jute and sisal yarns are about 4 times those of individual fibers. Since natural fiber yarns are assemblies of individual fibers, their density tends to be lower than that of their constituent fibers. The jute and sisal yarns used in this investigation had densities of about 0.9 and 0.8 gr/cm³, respectively, compare to 1.4 gr/cm³ density of individual jute and sisal fibers [99].

The natural fiber yarn properties are below those provided by the steels used in ferrocement; the yield strengths of these steels, for example, are about 4 times the tensile strength of jute and sisal fiber yarns considered above. Fabrics made with natural fiber yarns, however, provide closer yarn spacings when compared with the spacing of steel wires in (e.g., chicken) meshes used in ferrocement (see Figure 3.6). The orientations of yarns in natural fabric are also more favorable than those in hexagonal steel wire (chicken) mesh. The higher concentration and favorable orientation of the solid material (natural fiber yarns) can feasibly compensate for the lower mechanical properties of yarns versus steel. Hence, natural fabrics could potentially provide bulk mechanical properties which are competitive against those of the steel wire mesh reinforcement used in ferrocement.

Figure 3.11 Typical tensile load-deflection (left) and stress-strain (right) behavior of jute fiber yarns

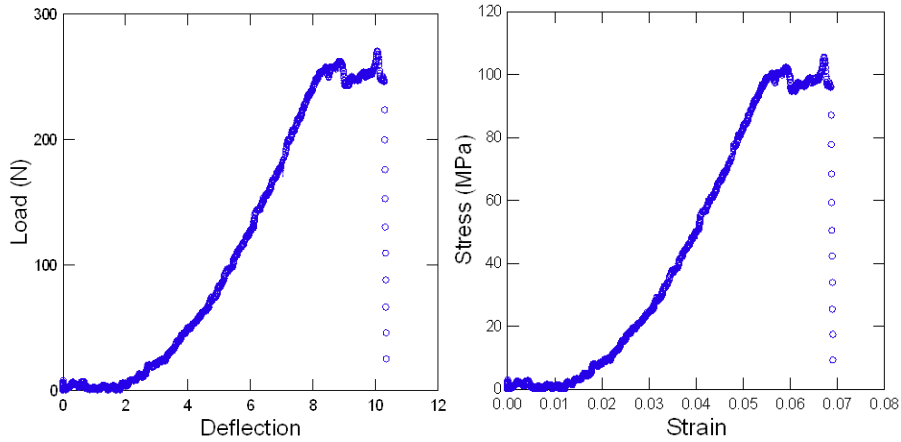


Figure 3.12 Typical tensile load-deflection (left) and stress-strain (right) behavior of sisal fiber yarns

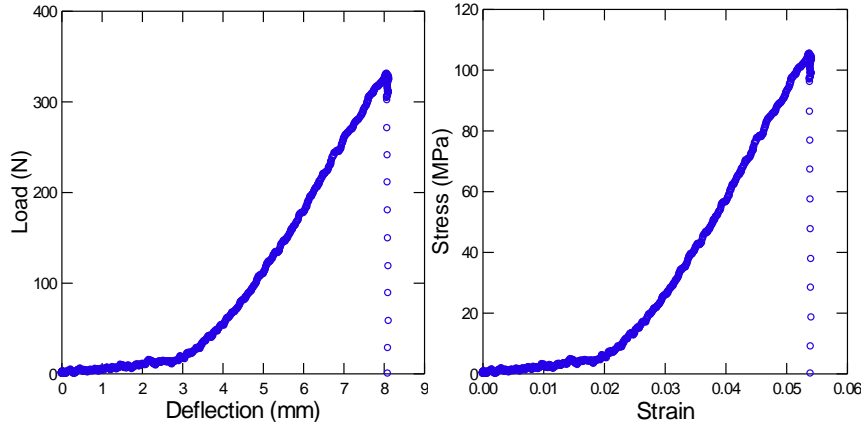


Table 3.1 Mean values of the mechanical properties of jute and sisal yarns

Yarn Fiber	Tensile Strength, MPa	Strain at Failure, %	Elastic Modulus, GPa
Jute	108	7.1	3.2
Sisal	107	5.5	3.05

Figure 3.13 shows the failure modes of the jute yarn burlaps and chicken mesh in tension. Failure of chicken mesh involved significant realignment of wires in the hexagonal units of the mesh. With the proper end grips developed in the project, failure of burlaps occurred away from the end grips near the mid-length of specimens. Typical tensile load-deflection and stress-strain curves for chicken mesh, ‘Jute 1’ burlap and ‘Jute 2’ burlap are presented in Figures 3.14, 3.15 and 3.16, respectively. The burlaps exhibit

strain-hardening behavior marked by initial deformations at low modulus followed by a rise in modulus. As was the case with individual yarns, the initial low-modulus behavior can be attributed partly to the realignment and tightening of the fibers in yarns under tension. The peak load provided by the 'Jute 1' burlap is comparable to (slightly higher than) that of chicken mesh. 'Jute 2' with a lower solid concentration (larger yarn spacing) provides a peak load that is about one-third that of chicken mesh. The mean values of tensile strength and strain at failure of the two burlaps and the chicken mesh are presented in Table 3.2. The yarns used in the particular jute fabrics used here have densities that are less than half that of the jute yarn tested earlier, implying that more fibers were packed more density in the jute yarn than the yarns used for production of the jute fabrics. This partly explains the relatively low tensile strengths of the jute fabrics versus the jute yarn. The relatively high strain at failure of chicken mesh can be largely attributed to the significant realignment under tensile loading of the steel wires configured into hexagonal units. It is worth mentioning that confinement in the cementitious matrix of ferrocement would reduce some of the realignments observed in tension testing of fabrics. This would influence the behavior of fabrics in ferrocement versus their behavior when tested alone (without the confinement of the cementitious matrix).

Figure 3.13 Failure modes of fabric specimens in tension



(a) Jute 1 burlap

(b) Jute 2 burlap

(c) Chicken mesh

Figure 3.13(cont'd)



(d) Failed specimens: Jute 1 (left), Chicken mesh in two perpendicular directions (center), Jute 2 (right)

Figure 3.14 Typical tensile load-deflection and stress-strain behavior of chicken mesh

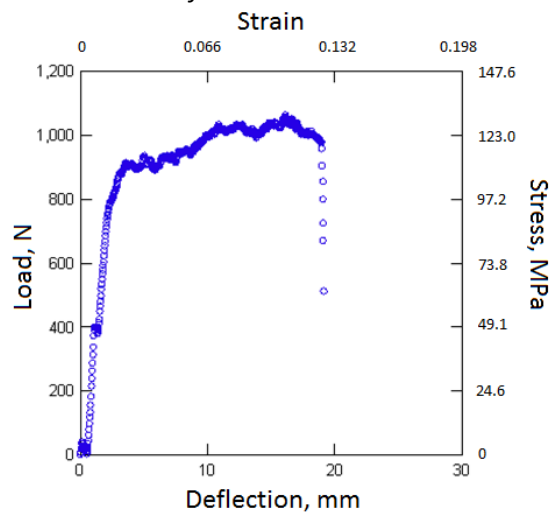


Figure 3.15 Typical tensile load-deflection and stress-strain behavior of the 'Jute 1' burlap.

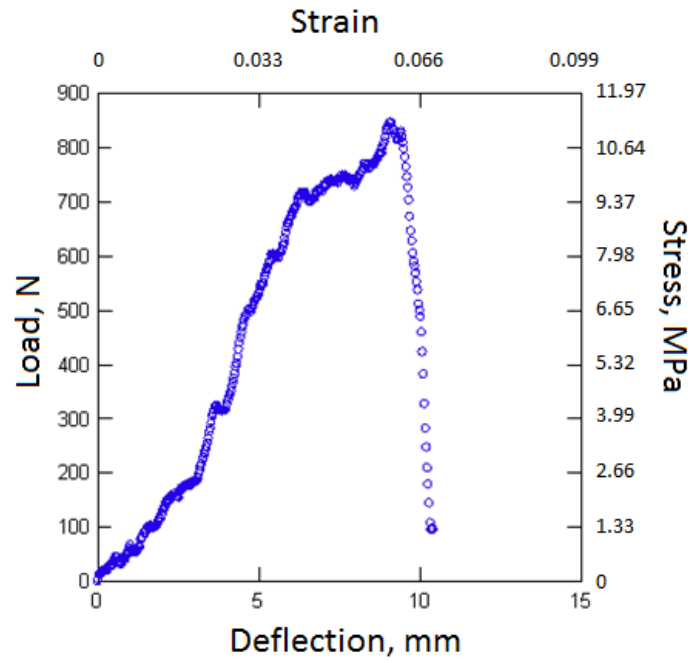


Figure 3.16 Typical tensile load-deflection and stress-strain behavior of the 'Jute 2' burlap

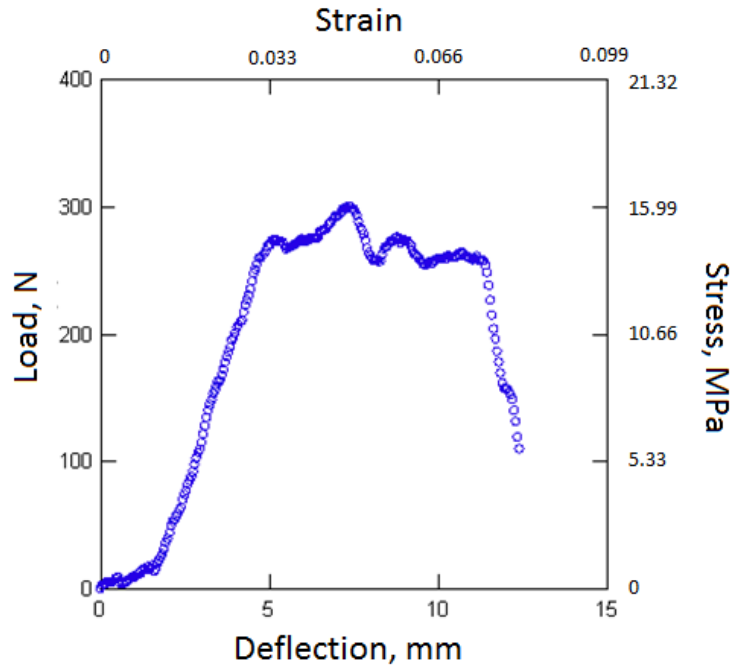


Table 3.2 Mean values of the mechanical properties of jute burlaps and chicken mesh

Fabric	Load at Failure, N	Deflection at Failure, mm	Stiffness, N/mm
Chicken mesh	845	19	150
'Jute 1' burlap	889	10	131
'Jute 2' burlap	301	13	80

(a) Load and deflection

Fabric	Cross-Sectional Area (solid), mm ²	Tensile Strength(MPa)	Strain at Failure (%)
Chicken mesh	10.05	128	13
'Jute 1' burlap	39.33	11.5	7
'Jute 2' burlap	12.46	16.1	8

(b) Strength and Strain

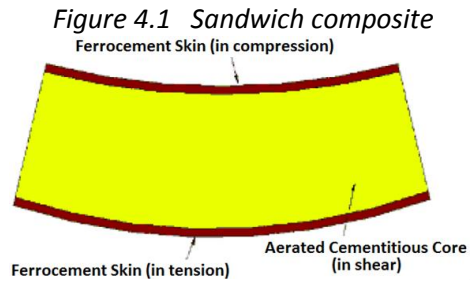
** Nominal stress is used to reflect the misalignment of wires in chicken mesh and the void content of the yarns in jute fabrics*

DEVELOPMENT OF A STRUCTURALLY EFFICIENT INDIGENOUS BUILDING MODULE

4.1 Introduction

The indigenous inorganic binders and reinforcement systems developed in Phase I project provide a solid basis to devise efficient building systems. The function of buildings in general is to provide comfort, serviceability and safety against natural and man-made hazards at viable cost and with a desired service life. Use of indigenous materials and practices, speed of construction, and ease of demolition are also some key considerations in this project. In order to efficiently meet these requirements, an attempt was made to select a multifunctional system which can efficiently meet the requirements relevant to structural load-bearing and energy absorption capacity under gravity and wind loads, blast and seismic effects, and projectile impact, complemented with adequate thermal and sound insulation. Sandwich composites (Figure 4.1) comprising ferrocement skins with an aerated concrete core (both of which can be fabricated with indigenous materials) constitute the system devised to efficiently and effectively meet these requirements using indigenous materials. In this sandwich composite, two thin, stiff, strong and ductile ferrocement skins (faces) are separated by a thick and light aerated cementitious core which provides the minimum shear modulus and strength properties required to induce sandwich behavior. Adequate force transfer capacity should be provided between skins and the core to ensure integrated structural action of the two skins. In sandwich composites, skins carry the in-plane and out-of-plane loads, and the core resists transverse shear (analogous to the web of an I-beam) and keeps the faces in place.

The structural behavior of a sandwich composite is similar to that of an I-beam, which is an efficient structural shape because a large fraction of the structural material is placed in flanges located the farthest from the neutral axis. Only enough material is left in the core (that replaces the connecting web) to make the skins (that replace flanges) work together, and to provide skins with resistance against shear and buckling modes of failure.



The 'sandwich effect' can be explained by considering a homogenous skin material with a given elastic modulus and strength, which is built into sandwich composites of different thickness. A core of negligible weight separates the two skins. Figure 4.2 presents the flexural stiffnesses and strengths of sandwich composites with different thicknesses. These values highlight the merit of sandwich composite as an efficient structural system. Besides high stiffness- and strength-to-weight ratios, sandwich composites can also be designed to efficiently provide improved impact and projectile penetration resistance, energy absorption capacity, wear and weathering resistance, thermal and sound insulation qualities, and fire resistance.

Figure 4.2 Structural efficiency of sandwich composites subjected to flexure

Single Skin - t	Sandwich - $2t$	Sandwich - $4t$
Weight: 1	Weight: 1	Weight: 1
Strength: 1	Strength: 6	Strength: 6
Stiffness: 1	Stiffness: 12	Stiffness: 48





Sandwich composites should be designed to meet the following structural requirements: (i) the ferrocement skins should provide adequate strength to withstand the tensile, compressive and shear stresses induced by loads (Figures 4.3a); (ii) the core and the core-skin interface should have adequate strength to withstand the shear stresses induced by loads (Figure 4.3b); (iii) the core should have adequate shear modulus and thickness to prevent overall buckling of the sandwich composite under structural loads, and to prevent crimping (Figure 4.3c); (iv) the core and skins should have adequate compressive

modulus to prevent wrinkling of skins under structural loads (Figure 4.3d); (v) the core should have adequate compressive strength to resist crushing under loads acting normal to the skin or by compressive stresses induced by flexural action (Figure 4.3e); and (vi) The overall sandwich structure should provide adequate flexural and shear rigidity to avoid excess deflections under service loads (Figure 4.3f). The applications targeted in this project also require design of composites which resist projectile penetration. Sandwich composites experience complex damage and failure mechanisms (Figure 4.4). The approach adopted in this project emphasizes mitigation of various damage phenomena in order to realize the full tensile (or compressive) resistance of ferrocement skins.

Figure 4.3 Structural design requirements of sandwich composites.

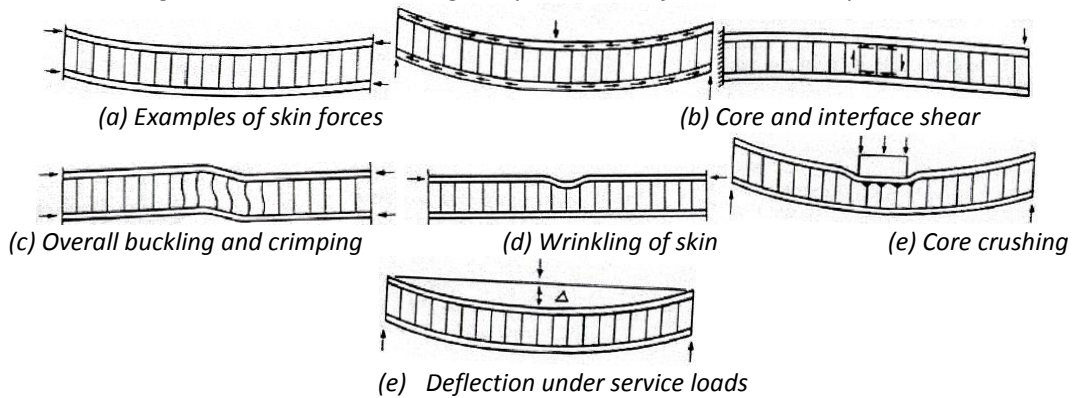


Figure 4.4 Structural damage and failure mechanisms of sandwich composites under flexural loading



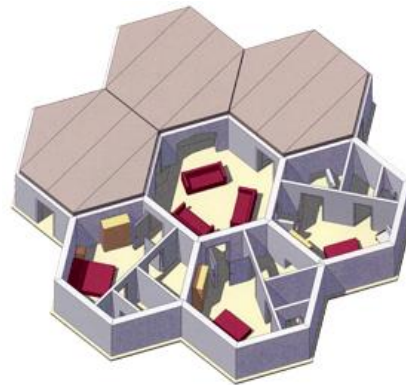
4.2 Preliminary Design of Military Building Systems with Sandwich Composite Module

4.2.1 Introduction

A preliminary design was devised with the objective of verifying the viability of the sandwich composite system introduced above as the principal module for a building system that meets the key requirements of the targeted application. The sandwich composite with ferrocement skins provides a versatile basis for development of diverse building systems. Examples include the beehive shelter (Figure 4.5a) and B-hut (Figure 4.5b). Preliminary designs were developed, using the indigenous sandwich composite introduced

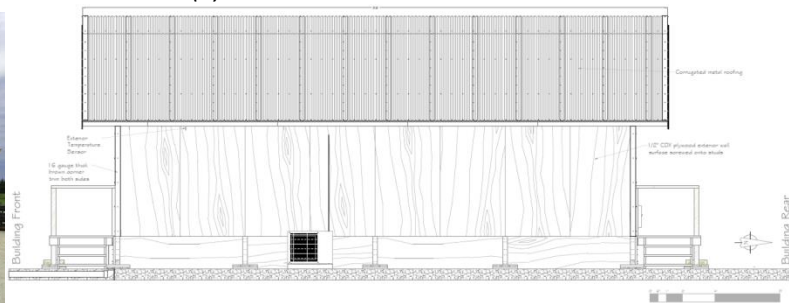
above, for the beehive shelter under extreme (blast and projectile impact) forces, and for B-hut under typical live, dead, wind and earthquake forces. The basic premise is that the indigenous sandwich composite panels enable design of alternatives to these building systems that are safer, more comfortable, serviceable, energy-efficient and sustainable, and can be built rapidly and economically using indigenous materials and resources with local labor. The thin-sheet nature of the primary structural constituents of the new building system also facilitates its demolition.

Figure 4.5 Examples of military building systems



(a) Schematics of the beehive shelter (<http://beehive.erikrowland.com/pre-fab-solutions/the-design/>)

(b)



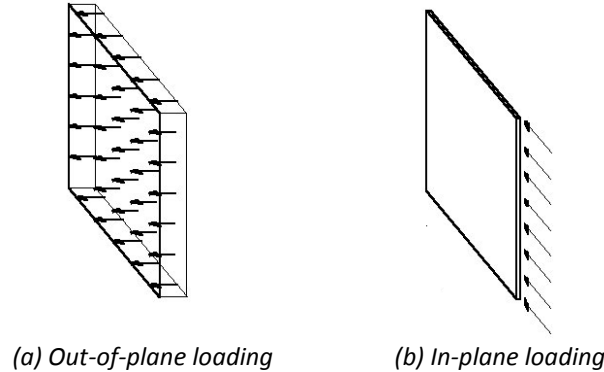
(b) Typical wood-frame B-hut [3, 103]

4.2.2 An Indigenous Alternative to the Beehive Shelter Under Extreme Loads

A preliminary design was developed for the beehive shelter with indigenous sandwich composites. Extreme loading conditions (blast, projectile impact and earthquake) as well as thermal insulation requirements provided the basis for this preliminary design.

Lateral (blast or earthquake) loading of the beehive shelter subjects the (indigenous) sandwich composite walls of the shelter to out-of-plane (Figure 4.6a) or in-plane (Figure 4.6b) loading, depending on their orientation with respect to the primary direction of loading.

Figure 4.6 Out-of-plane and in-plane loading of wall panels



We will understand the structural design for blast loading in this section. Blast loads are pressure waves that propagate spherically, and dissipate with travel distance (Figure 4.7). While blast loading is dynamic in nature, the simplified approach adopted here simulated blast as a static pressure. The blast pressure was calculated for 20 lb of C-4 explosive charge detonated at a distance of 60 ft from the building [104]. Following the procedures outlined in “The Handbook for Blast Resistant Design of Buildings” (Table 4.1), the equivalent mass for pressure calculation was found to be 14.6 lb. Equation $Z = \frac{R}{\sqrt[3]{W}}$ was then used to find the scaled distance (Z), where R is the average explosive (standoff) distance from the target, and W is the equivalent mass of the explosive. The equation yielded a scaled distance of 22.13 ft/lb^{1/3} for a standoff distance of 60 feet (the average distance of the explosive to the closest structural element). Using this information, the peak incident overpressure value was obtained from Figure 4.8 at 6.5 psi (0.045 MPa).

Figure 4.7 Blast wave propagation [104]

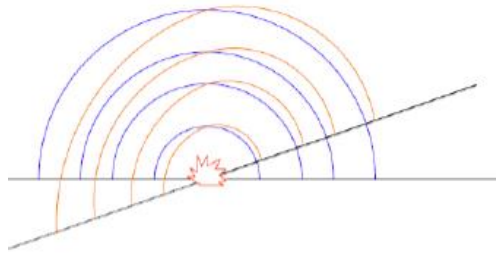
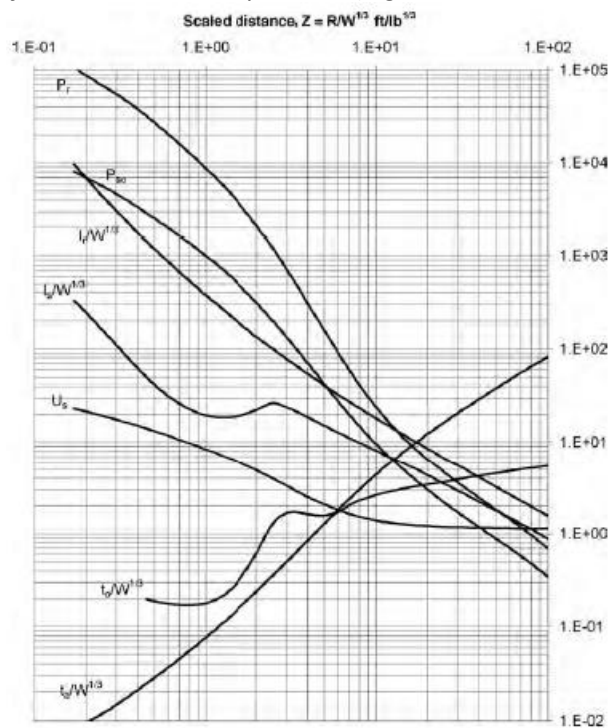


Table 4.1 C-4 Equivalency Conversion Factors, from “The Handbook for Blast Resistant Design of Buildings”.

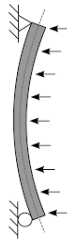
Composition B	1.65	1.11	0.98	0.03 to 0.35
		1.20	1.30	0.69 to 6.90
Composition C-3	1.60	1.05	1.09	NA ¹
Composition C-4	1.59	1.20	1.19	0.07 to 1.38
		1.37	1.19	1.38 to 20.70
Cycloid (75/25 RDX/TNT)	1.71	1.11	1.26	NA ¹
(70/30)	1.73	1.14	1.09	0.03 to 0.35

Figure 4.8 Conversion of scaled distance to pressure (Fig 6.6 in Handbook of Blast Resistant Design)



Wall panels oriented perpendicular to the blast pressure were simulated as simply supported slabs with 2 m span and 1 m width. The wall panel under 0.045 MPa out-of-plane blast pressure (Figure 4.9) experiences a maximum bending moment ($M=wl^2/8$) of 22.5×10^6 N.mm.

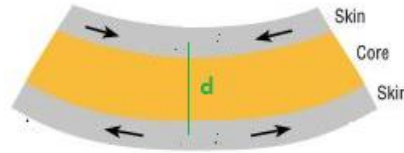
Figure 4.9 Wall panel subjected to out-of-plane blast pressure



In a simplified approach to assessment of the flexural strength of sandwich composite under out-of-plane loading (see Figure 4.6a), one can consider only the skin (tensile and compressive) forces (Figure 4.10), and make the reasonable assumption that the tensile strength of skin is smaller than its compressive strength. It was also assumed that the tensile strength of skin (in the post-cracking region) is equal to the tensile strength of its fabric reinforcement. Flexural strength of the sandwich composite can thus be approximated as the tensile strength of skin times the center-to-center spacing of skins (d in Figure 4.10). Each layer of the reinforcing fabrics considered in this investigation (chicken mesh, 'Jute 1' burlap, and 'Jute 2' burlap) provides, at a width of 115 mm, a tensile strength that is within the 301 - 889 N range (see Table 3.2a). With a width of 1000 mm, which was used in calculation of the blast-induced moment, the tensile strength provided by the selected reinforcing fabrics translates into 2,617 - 7,730 N tensile strength. Assuming a center-to-center skin spacing (d in Figure 4.10) of 200 mm, the skin tensile force developed under blast pressure can be calculated as $M/d=22.5 \times 10^6/200=112,500$ N. 15 layers of the 'Jute 1' burlap, noting that a 1,000-mm width of this burlap provides a tensile strength of 7,730 N. This is a relatively large number of fabric layers in ferrocement. It should, however, be noted that fabrics embedded in ferrocement were found, as discussed in later sections, to provide significantly higher tensile load-carrying capacity than that considered here (for the fabric reinforcement tested alone without the

confinement of the cementitious binder). The simplified approach to flexural strength calculation followed here was also found to be highly conservative. Hence, the required number of fabric layers in skins is over-estimated in this simplified approach. This implies that, as far as the flexural forces induced in wall panels under out-of-plane blast loading are concerned, the proposed sandwich composite module can feasibly provide the required structural performance.

Figure 4.10 Simplified flexural forces assumed to develop (only) in skins at failure



As far as in-plane forces developed in sandwich composites under blast loading are concerned (see Figure 4.6b), considering a single unit of beehive shelter (Figure 4.11), one can assume that two shear walls of about 2 m height need to resist the blast pressure (calculated earlier at 0.045 MPa) applied on a surface area that is about 7 m wide and 2 m high. This translates into a shear load of 158 N per mm of height (Figure 4.12). The total shear force to be resisted by the shear wall is $158 \times 2,000 = 316,000$ N. The maximum bending moment generated at the base of the shear wall is $158 \times 2,000 \times (2,000/2) = 316 \times 10^6$ N.mm. It is worth mentioning that the assumption that walls within beehive act individually as shear walls is rather conservative. Depending on the quality of joints between the walls which constitute a beehive unit, the whole unit could act as a box section under lateral loads.

The design developed under out-of-plane blast pressure comprised two skins with 15 layers of jute burlap. The conservative assumption that shear resistance is provided only by the fabric reinforcement in skins yields the following shear resistance for the two skins [105]:

$$V_n = 2n \cdot A_f \cdot L \cdot f_u = 2n \cdot F_u$$

where, n is the number of fabric layers in each skin, A_f is the area of each fabric per unit length of wall, L is the wall length, f_u is the tensile strength (per unit area) of fabric, and F_u is the tensile strength provided by each fabric layer with a width of L (the smaller of wall length and height, that is 2 m, is used here as L).

For the design parameters determined for out-of-plane flexural action under blast loading, the in-plane shear strength of the sandwich wall is:

$$V_n = 2n.A_f.L.f_u = 2 \times 15 \times F_u = 2 \times 15 \times (2 \times 7,730) = 463,800 \text{ N}$$

The in-plane shear strength provided by the sandwich wall designed for out-of-plane blast loading is thus greater than the required shear strength of 316,000 N for in-plane blast forces. The design developed for out-of-plane flexural action under blast loading is thus satisfactory under the in-plane shear forces generated by the blast loading.

The in-plane flexural strength provided by thin cementitious skins with fabric reinforcement can be calculated as follows [106]:

$$M_n = A_{sv}.f_y.z \leq 0.4 f_k.b_w.d^2$$

where, A_{sv} is the total area of the vertical reinforcement, f_y is the design strength of the vertical reinforcement, f_k is compressive strength, b_w is thickness, d is the length of the wall, and z is the lever arm which (when maximum compression and tension are reached together) may be taken as:

$$z = d.(1 - 0.5 A_{sv}.f_y / (b_w.d.f_k)) \leq 0.95 d$$

For the wall considered here, with two 20-mm thick skins incorporating 15 layers of fabric reinforcement, focusing on the two skin layers which provide the bulk of structural performance,

$$A_{sv}.f_y = 2 \times 15 \times F_u = 2 \times 15 \times (2 \times 7,730) = 463,800 \text{ N}$$

$$0.4 f_k b_w.d = 0.4 (20) (40) (2000)^2 = 128 \times 10^7 \text{ N}$$

$$z = 2000 (1 - 0.5 (463,800) / (40 \times 2000 \times 20)) \leq 0.95 (2000)$$

$$= 1,698 \leq 1,900$$

$$= 1,698 \text{ mm}$$

$$M_n = A_{sv}.f_y.z \leq 0.4 f_k.b_w.d^2$$

$$= 463,800 \times 1,698 \leq 128 \times 10^7$$

$$= 79 \times 10^7 \leq 128 \times 10^7$$

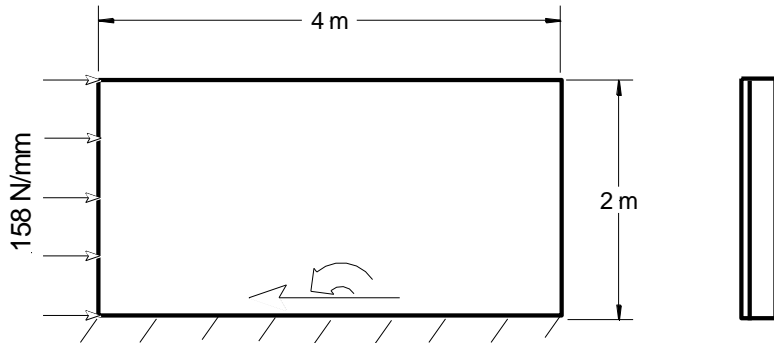
= 79×10^7 N.mm

This flexural strength is larger than the maximum in-plane bending moment of 31.6×10^7 N.mm generated at the wall base under blast loading. The wall design thus meets the requirements for resisting both the in-plane and out-of-plane forces generated under blast loading.

Figure 4.11 A single unit of the beehive shelter



Figure 4.12 In-plane blast loading on a beehive wall of 220 mm total thickness with 20 mm thick ferrocement skins

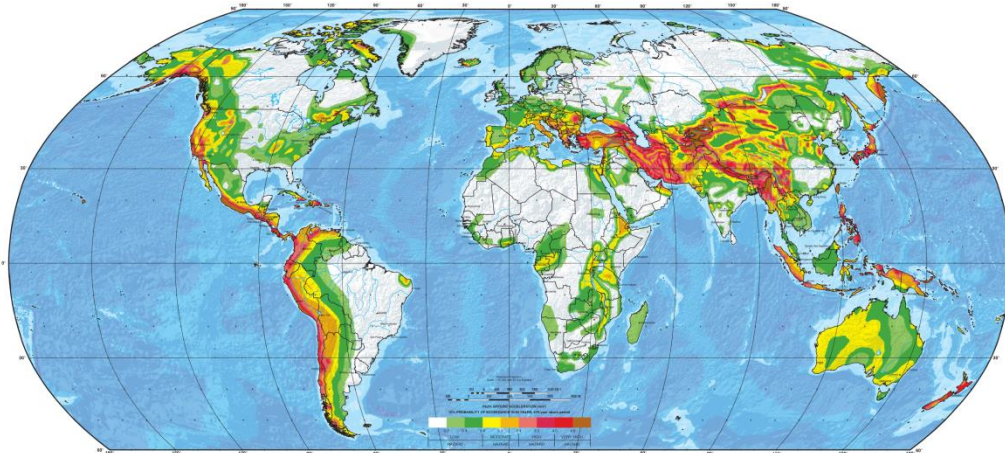


We will briefly evaluate earthquake forces experienced by the structure compared to possible blast loads. Assuming densities of 2,100 and 400 kg/m³ for the skin and the core components of sandwich walls, respectively, the weight of each wall (Figure 4.12) can be approximated at 1,248 kg (~46% of which corresponds to the core weight). Assuming a similar cross-sectional sandwich design for the roof (which is conservative), the beehive unit comprising six walls and the roof would weigh about 14,000 kg.

Figure 4.13 presents the global seismic hazard map. The African continent largely covers low to moderate seismic risk regions, and the Middle East covers regions with very high seismic risk. Considering the worst case of very high seismic risk, the peak ground acceleration with 10% probability of exceedance in 50 years (478-year return period) is 4.8 m/s² (noting that ground acceleration is 9.8 m/s²). Considering the high

rigidity of the one-story beehive shelter made with the (indigenous) cementitious sandwich composite, one can assume that the building would experience the ground peak acceleration in very high-risk seismic zones, that is 4.8 m/s^2 . The peak (total) lateral force under this peak earthquake acceleration would be $14,000 \times 4.8 = 67,200 \text{ N}$, compared to the total blast lateral force of $632,000 \text{ N}$. Therefore, as far as the lateral loads are concerned, blast governs structural design. It should be noted that there are energy dissipation requirements associated with seismic design that need to be addressed.

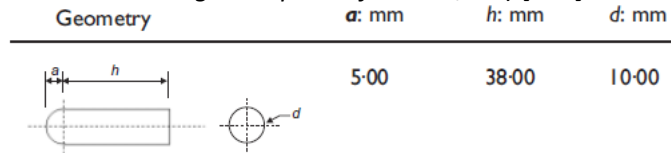
Figure 4.13 Global seismic hazard map



We will discuss some design considerations related to projectile penetration resistance. The sandwich composite walls designed in previous sections for blast (and earthquake) resistance comprise ferrocement skins with a relatively thick aerated concrete core. This is a viable system for providing resistance against projectile penetration. A preliminary analysis was conducted in order to assess the projectile penetration resistance of this sandwich wall system. The projectile used in this analysis, shown in Figure 4.14 with a mass of 25.7 g , when traveling at a speed of 77.2 m/sec , was found in an experimental investigation [107] to penetrate most into aerated concrete when compared with the same projectile traveling at different speeds, or when compared with other projectiles of similar mass but different geometric configurations. The projectile shown in Figure 4.14, when traveling at a speed of 77.2 m/sec , penetrated 195 mm into an aerated concrete with $800\text{-}900 \text{ kg/m}^3$ density. The aerated concrete used as core in the sandwich composite wall designed under blast loading has a thickness of 180 mm . Therefore, without the help of

ferrocement skins, the projectile considered here can penetrate the core. It should be noted that the targeted density of the aerated concrete core (400 kg/m³) is lower than that considered in the projectile penetration tests considered here [107].

Figure 4.14 The projectile considered for assessment of penetration resistance (with mass of 25.7 g, traveling at a speed of 77.2 m/sec) [107]



Since the aerated core alone in the sandwich wall design cannot prevent penetration of the projectile described above, an analysis was conducted in order to assess the resistance of the whole sandwich composite wall against penetration. For this purpose, the following expression was used for predicting the depth of penetration (P_c) of a projectile into concrete (Unified Facilities Criteria – Section 3-340-01):

$$P_c = \frac{56.6 \left(\frac{m}{D^3}\right)^{0.075} N m v^{1.8} \left(\frac{D}{c}\right)^{1.5} f_{age}}{D^2 \sqrt{f_c}} + D$$

where, D and m are the projectile diameter and mass, respectively, v is the projectile velocity, f_c is the concrete compressive strength, c is the maximum aggregate size of concrete, f_{age} is the age factor, and N is the Nose Performance Coefficient. The parameters input into the above equation, and the calculated values of the depth of penetration of the projectile into the ferrocement skin and the aerated concrete core are presented in Table 4.2.

Table 4.2 The input parameters and the calculated depths of penetration of the projectile into the ferrocement skin and the aerated concrete core of the sandwich composite wall

	D(mm)	m (kg)	v (m/s)	c (mm)	f_c (MPa)	P_c (mm)
Skin	10	0.0257	75	1.5	25	64
Core	10	0.0257	75	1.5	1	279

The calculated depths of the projectile penetration into the skin and the core (64 mm and 279 mm, respectively), when considered alone, exceed the thicknesses of the two skins (40 mm) and the aerated

concrete core (180 mm). With the two skins and the core built into a sandwich composite, their combination would dissipate the kinetic energy of the projectile via mechanisms such as fracture, deformation, bending, delamination and hole enlargement. As a first estimate, it was assumed that energy dissipation occurs linearly with the depth of penetration. This implies that the 20 mm outer skin dissipates $20/64=31\%$ of the kinetic energy of the projectile. The remaining kinetic energy would allow the skin penetrate $(1-0.31)\times 279=192\text{mm}$ compared to the core thickness of 180 mm. The projectile thus has barely adequate energy to penetrate the outer skin and the aerated concrete core. Once it reaches the inner skin, it has lost $20/64+180/279=96\%$ of its kinetic energy. It can penetrate only $0.04\times 64=2.56\text{ mm}$ into the inner skin (compared to the 20 mm thickness of the skin) before it stops.

The above preliminary analyses indicate that the sandwich composite wall design that was developed to resist out-of-plane and in-plane forces developed under blast loading is also viable for mitigating projectile penetration.

An assessment of the Insulation Qualities of the Sandwich Composite will be conducted in this section. Typical thermal insulation requirements in warm regions of the United States, representing the climatic conditions of the targeted geographic regions of Africa and Middle East, are R-2.5 for walls, R-39 for ceiling, and R-13 for floor (<http://www.homeenergysavingspro.com/insulation-r-values-indiana.htm>).

The sandwich composite building module introduced above incorporates an aerated concrete core which, in addition to making contributions towards structural performance and projectile penetration resistance, provides viable insulation qualities. An aerated concrete with 400 kg/m^3 density has a thermal conductivity (K) of $\sim 0.1\text{ W/mK}$. The aerated concrete core of the sandwich composite, with a thickness (t) of 180 mm provides a t/K value of $0.18/0.1=1.8\text{ m}^2\text{K/W}$ (or $5.67\times 1.8=10.21\text{ ft}^2\cdot^\circ\text{F/Btu}$), representing an R-10.21 value. This is an acceptable insulation quality for walls and floors of buildings located in the warm regions of the United States, but falls short of the R-39 ceiling insulation requirement in these regions.

One needs to increase the thickness of the aerated concrete insulation layer in ceiling in order to meet this requirement.

Aerated concrete, when compared with polymer-based insulation foams, offers improved fire resistance and safety attributes. As described later, it can also be produced using abundant indigenous raw materials of Africa and Middle East (and elsewhere).

4.2.3 An Indigenous Alternative to B-Hut Under Conventional Loads

The structural analysis and design outlined above considered extreme (primarily blast and projectile impact) loading of a beehive shelter. This extreme loading yielded a relatively thick sandwich composite with a relatively large number of natural fabric reinforcement layers in ferrocement skins. A simpler design is devised in this section for B-hut constructed with the indigenous sandwich composite panels. The focus of this design is on basic (live, dead, wind, etc.) loads, excluding extreme (blast and projectile impact) loading conditions.

The preliminary sandwich composite geometry considered for use in B-hut is depicted in Figure 4.15. This design comprises two 10 mm thick ferrocement skins with an aerated concrete core of 180 mm thickness, yielding a sandwich composite with 200 mm total thickness. The number of natural fabric layers in ferrocement skins will be determined in the course of analysis, and the basic geometry of Figure 4.15 will be refined if necessary. The indigenous binder and reinforcement selected for use in the ferrocement skin are pumice-lime with soda ash additives (Mix 8 in Table 2.2) and 'Jute 2 (see Figure 3.6), respectively. The indigenous aerated concrete selected for use in the sandwich composite comprises lime-gypsum binder with natural saponin foaming agent, introduced later in Chapter 6 (Mix 22 in Table 6.1). A sandwich composite flat roof is considered (in addition to sandwich composite walls) for the indigenous B-hut (in lieu of the truss roofs used in the conventional wood structure of B-hut).

Figure 4.15 Preliminary thicknesses of the indigenous sandwich composite constituents



The test data on the selected ferrocement binder and aerated concrete presented in Chapters 2 and 6, respectively, indicate that the skin and core densities in the selected sandwich composite are 2,200 and 500 kg/m³, respectively. The dead load (self-weight of the sandwich composite), D is thus 1,340 N/m² (28 psf). The live load, L , considered for B-hut is 4,786 N/m² (100 psf), and the snow load, S , is assumed to be 479 N/m² (10 psf), which was assumed to be greater than the rain load. With an assumed wind speed of 100 mph, the wind load is calculated at 479 N/m² (10 psf). The earthquake load, E , was neglected in this analysis. The conventional B-hut design (see Figure 4.5b) essentially isolates the structure from ground using a layer of gravel upon which the structure rests. Adoption of this approach with the indigenous sandwich composite B-hut would rationalize neglecting of the earthquake force in this preliminary analysis.

As far as the factored roof (gravity) load is concerned, the governing load combination is $1.2D+1.6L+0.5S = 9,428 \text{ N/m}^2$ (197 psf). Wind is assumed to be the only source of lateral load, yielding a factored lateral pressure of $1.6W=766 \text{ N/m}^2$ (16 psf) as part of the factored load combination $1.2D+1.6W+0.5S$ or $0.9D+1.6W$. The factored uniform loading applied on the roof ($9,428 \text{ N/m}^2$) far exceeds that applied normal to walls (766 N/m^2). Therefore, in spite of the differences in planar dimensions and boundary conditions, roof loading is more critical for design of the sandwich composite in out-of-plane bending. Roof loading also governs design of walls in compression. Wind loading would determine design of walls under in-plane shear.

As a first step, the flexural action of the (flat) roof panel is used to design the sandwich composite. For a B-hut that is 9.8 m (32) ft long and 4.9 m (16 ft) wide, the roof panel acts as a one-way slab. The vision a

B-hut comprising sandwich composite panels prepared at ground level and assembled into the building system via rigid joints produces nearly fixed boundary conditions for one-way roof slab. The maximum bending moment generated in a 1-m strip of the roof slab with a span of 4.9 m (16 ft) would be $M_u = w_u \cdot l^2 / 12 = 9,428 \times (4.9)^2 / 12 = 18,864$ N.m. With a center-to-center spacing between skins of 190 mm in the sandwich composite design of Figure 4.15, a conservative value of tension force produced in skin under this bending moment would be $18,864 / 0.19 = 99,284$ N (for a one-meter width of skin). The test data presented in Chapter 5 indicate that a ferrocement with 115 mm width and 10 mm thickness that is reinforced with 3 layers of 'Jute 2' fabric provides a tensile strength of 2,000 N, which translates into 17,391 N tensile force over a 1-m width. This implies that, in the conservative approach adopted here, 17 layers of 'Jute 2' fabric would be needed in the skin of the sandwich composite design shown in Figure 4.15. A preliminary experimental investigation of sandwich composites presented in Chapter 7 indicated that, given the high mechanical qualities of the aerated concrete core, the actual flexural strength of the sandwich composite can be twice that calculate using the conservative approach adopted here. The number of 'Jute 2' fabric layers required in skin could thus be reduced to about eight.

As far as compression in B-hut walls is concerned, for a wall height of 2.44 m, the buckling load for a 1-m wide strip of the wall can be calculated as $P_{cr} = \frac{\pi^2 EI}{L^2} = \frac{3.14^2}{2.44^2} \times 0.000185 \times 20 \times 10^9 = 6.11 \times 10^6$ N. The compressive strength of this 1-m strip of the wall can be conservatively estimated as the compressive strength of the two skins, that is $0.02 \times 1 \times 25 \times 10^6 = 0.5 \times 10^6$ N. Hence, the material-based compressive strength of the 1-m wide strip of the wall defines its compressive strength of 0.5×10^6 N. With a roof area of 4.9×9.8 m and a factored uniform load of $9,428$ N/m², the factored compressive load per unit (1 m) width of the wall is: $9,428 \times 4.9 \times 9.8 / (2 \times 4.9 + 2 \times 9.8) = 15,399$ N which is far smaller than the 0.5×10^6 N compressive load-carrying capacity of the 1-m strip of the wall. Hence, the sandwich composite design of Figure 4.15 is more than adequate for resisting the wall compressive forces. One should also consider the wall performance under the combination of axial load and out-of-plane bending moment, noting that the

$P\Delta$ effect tends to increase the bending moment. A factored wind pressure of 766 N/m^2 generates, with the conservative assumption of a simply supported wall along its height, an out-of-plane bending moment of 570 N.m for a 1-m strip of the wall. This bending moment should be increased, due to the $P\Delta$ effect by a factor of $\frac{1}{1-\frac{P}{P_c}} = \frac{1}{1-\frac{15,399}{6.11 \times 10^6}} = 1.0025$; the $P\Delta$ effect in walls is thus minor, and increases the bending moment from 570 N.m to $570 \times 1.0025 = 571.5 \text{ N.m}$. The stress generated under this bending moment in the indigenous ferrocement skin can be calculated, conservatively neglecting any contribution from the core, as $M.c/I = 571.5 \times 0.05 / (2 \times 0.01 \times 1 \times 0.045^2) = 75.6 \times 10^4 \text{ N/m}^2$ (or 0.76 MPa). This stress induced by bending moment is only about 3% of the compressive strength of the ferrocement skin, and would not alter the discussions made above where the bending moment was neglected.

As far as the in-plane shear behavior of sandwich composite walls is concerned, the factored wind pressure of 766 N/m^2 applied on the $2.44 \text{ m} \times 9.6 \text{ m}$ area of the larger wall produces a total lateral shear force of $17,943 \text{ N}$ applied on two walls, or $8,971 \text{ N}$ per wall with 4.9 m width and 2.44 m height.

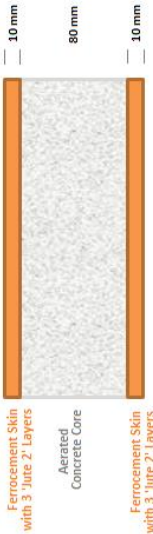
The in-plane shear strength provided by the sandwich composite with n layers of 'Jute 2' fabric in each skin is [105]: $V_n = 2n.A_f.L.f_u = 2n.F_u$ where, A_f is the area of each fabric per unit length of wall, L is the wall length, f_u is the tensile strength (per unit area) of fabric, and F_u is the tensile strength provided by each fabric layer with a width of L (the smaller of wall length and height, that is 2.44 m , is used here as L). In order to provide resistance against the factored shear force of $8,791 \text{ N}$, $2n.F_u = 2n.(2.44 \times 2,609) = 8,791$. Hence, the required number of 'Jute 2' fabrics in each skin, n , is only 0.7 . In other words, even with a reasonable capacity reduction factor, only one layer of 'Jute 2' fabric per skin would be adequate for resisting the in-plane shear forces with the sandwich composite design of Figure 4.15. The in-plane bending moment generated in the wall under factored lateral forces can be estimated at $8,791 \times 2.44 / 2 = 10,725 \text{ N.m}$. The in-plane flexural strength of the wall can be conservatively estimated as [106]: $2n.F_u \cdot 0.95d = 2n(4.9 \times 2,609) \cdot (0.95 \times 4.9) = 119,020n \text{ N.m}$. With a factored in-plane flexural force of $10,725 \text{ N.m}$, the calculated value of n (number of 'Jute 2' fabric layers per skin for resisting in-plane

flexure) would be 0.1. In other words, with any reasonable capacity reduction factor, only one layer of 'Jute 2' fabric per ferrocement skin would be adequate for resisting the in-place flexural forces.

The 180-mm aerated concrete core provides a thermal insulation equivalent to R-10.21, which is acceptable for walls and floors of buildings located in the warm regions of the United States, but falls short of the R-39 ceiling insulation requirement in these regions.

The combination of structural and insulation analyses outlined above indicate that the sandwich composite used as wall panels could have smaller skin and core thicknesses than those shown in Figure 4.15. In the case of the sandwich composite roof panel, however, increased thicknesses would yield a more viable design for meeting relevant structural and insulation requirements. In the case of walls, a sandwich composite comprising 80 mm thick core and 10 mm thick skins (Figure 4.16) with three layers of 'Jute 2' fabric in each skin would meet the structural (compressive, in-plane shear and flexural, and out-of-plane flexural) requirements while providing a viable insulation level. This sandwich composite design was used in structural tests and relevant theoretical analyses conducted in the project.

Figure 4.16 A viable sandwich composite design for the B-hut walls



DEVELOPMENT OF FERROCEMENT WITH INDIGENOUS REINFORCEMENT

5.1 Introduction

As a first step towards development of the sandwich composite module introduced in the previous section, a simplified version of the ferrocement skin of this module was processed and characterized. This work was performed parallel with development of indigenous cementitious materials. Therefore, a conventional Portland cement mortar was used in this early development effort. The reinforcing fabrics used, however, were indigenous systems 'Jute 1', 'Jute 2', and chicken mesh.

5.2 Some Theoretical Considerations

Ferrocement is a thin-sheet cement product where fabrics comprising relatively small-diameter wires with high specific surface area are used as reinforcement in a cementitious mortar matrix. The reinforcement volume fraction in ferrocement is relatively large when compared with that in conventional reinforced concrete. The high reinforcement ratio and specific surface area, and the improved bonding via mechanical anchorage of the 2D fabric (compared to 1D rebar) reinforcement induce multiple cracking in ferrocement (Figure 5.1) under tensile and flexural loading. This phenomenon enables redistribution of internal forces from critically stressed areas, and enhances the ductility and energy absorption capacity of ferrocement structures.

Figure 5.1 Multiple cracking of the tension face of a ferrocement panel under flexural loading

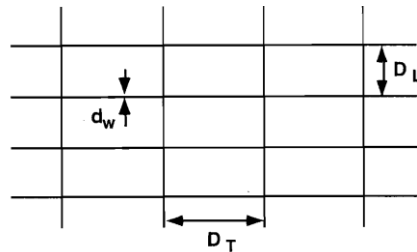


(<http://www.slideshare.net/jayarawman/flexural-behaviour-of-fibre-reinforced-ferrocement-concrete>).

The reinforcement volume fraction (V_r) is an important attribute of ferrocement, which depends upon (Figure 5.2) the number of fabric reinforcement layers (N), diameter of the fabric wires/yarns (d_w), center-to-center spacing of wires/yarns in longitudinal and transverse directions (D_L and D_T , respectively), and the total thickness of ferrocement (h) [100]:

Figure 5.2 Geometric attributes of fabric reinforcement

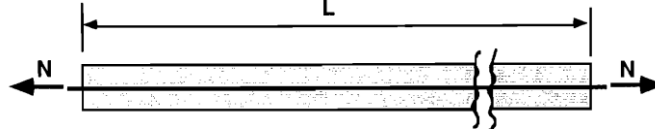
$$V_r = \frac{N \cdot \pi \cdot d_w^2}{4h} \cdot \left(\frac{1}{D_L} + \frac{1}{D_T} \right)$$



In tensile loading of ferrocement (which is key to the sandwich composite performance), the cementitious matrix contributes to tensile load-carrying capacity prior to cracking. Upon cracking, however, the tensile force is largely transferred to the reinforcing fabric (Figure 5.3). Depending on the reinforcement ratio,

specific surface area and bond strength, failure could either occur at the first crack formed, or after formation of multiple cracks.

Figure 5.3 Contribution of the reinforcing fabric to the tensile load-carrying capacity of ferrocement at a crack [100]



A minimum fabric reinforcement volume fraction $(V_r)_{min}$ is required for preventing brittle failure upon cracking (i.e., transfer of the composite tensile force to the reinforcing fabric at the first crack) [100]:

$$(V_r)_{min} = \frac{1}{\frac{\sigma_{ru}}{\sigma_{mu}} + 1 - n}$$

where, σ_{ru} and σ_{mu} are the reinforcement and matrix tensile strengths, respectively, and n is the modular ratio of the reinforcing fabric to cementitious matrix.

With adequate area of fabric reinforcement in the direction of loading and reinforcement-to-matrix bond strength, ferrocement experience multiple cracking. The average spacing between multiple cracks (L_{avg}) can be calculated as follows [100]:

$$L_{avg} = \frac{\sigma_{mu} \cdot \gamma}{\tau \cdot S_{rl}}$$

where, σ_{mu} is the matrix tensile strength, γ is a constant coefficient ranging from 1 to 2 (usually taken as 1.5), τ is bond strength, and S_{rl} is the specific surface area of the reinforcing fabric in the longitudinal direction.

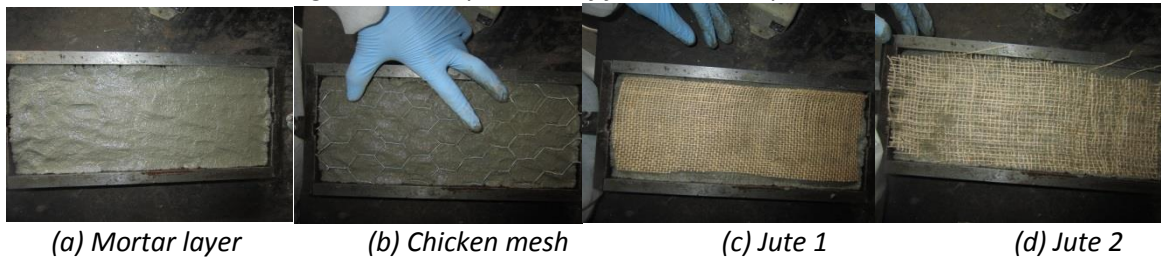
5.3 Experimental Program

The mortar matrix used for preparation of ferrocement sheets comprised Type I Portland cement, silica sand with maximum particle size of 1.5 mm, and water at cement: sand: water weight ratio of 1: 2: 0.5. The reinforcing fabrics used in experimental studies were 'Jute 1', 'Jute 2' and chicken mesh. The ferrocement specimens had length and width of 285 and 115 mm, respectively. Their thicknesses were initially about 20 mm (with 1-2 layers of fabric reinforcement). In order to promote multiple cracking by

raising the reinforcement surface area, the specimen thickness was reduced to 10 mm, and 2-3 layers of fabric reinforcement were used with this smaller thickness.

Preparation of specimens started with placement of a layer of mortar with ~2 mm thickness inside molds (Figure 5.4a), followed by the addition of the first layer of reinforcement (Figures 5.4b, c & d for chicken mesh, 'Jute 1' and 'Jute 2' reinforcement). The sequence of adding mortar and reinforcing fabric was then repeated until the ferrocement sheet with the targeted thickness and number of reinforcement layers was produced.

Figure 5.4 Preparation of ferrocement specimens



The specimens were kept inside molds under wet burlap for 24 hours. They were then demolded and cured in lime-saturated water for 3 days. Subsequently, they were stored at 50% relative humidity and room temperature until the test age of 10 days. Figure 5.5 shows a typical ferrocement test specimen.

Tension tests were performed using a screw-driven Instron test equipment (Figure 5.6) at a deflection rate of 2 mm/min, with a load cell and a deflection transducer used to collect load and deflection data throughout the test. The free length of tension test specimens was 150 mm.

Figure 5.5 Ferrocement test specimen

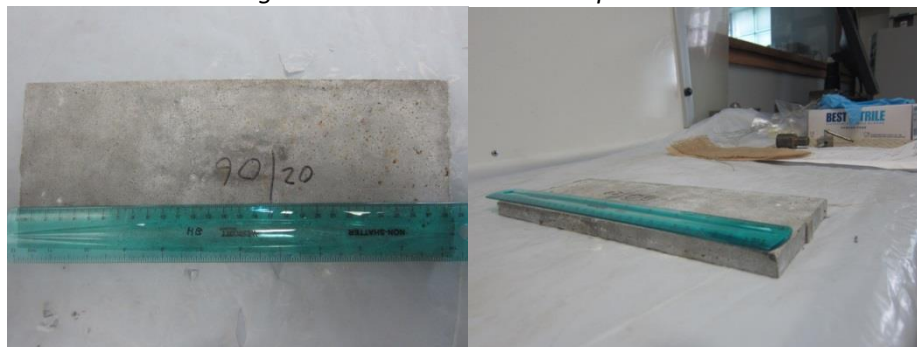


Figure 5.6 Ferrocement tension test setup



Projectile penetration tests were performed on ferrocement specimens that were supported at two ends over a span of 230 mm. A 22-caliber, long-range rifle (Figure 5.7a) was used to shoot projectiles (Figure 5.7b) with 5.7 mm diameter and 2.33 g mass at a speed of 378 m/sec onto the ferrocement specimen. The purpose of this test was to verify that the projectile geometry, mass and speed considered here is capable of penetrating the ferrocement sheet. The specific ferrocement sheet tested here had a thickness of 20 mm, and was reinforced with 1 layer of the 'Jute 2' burlap. The specimen, which had the dimensions of the tension test specimen, was simply supported over a span of 250 mm; two projectiles were shot at the specimen on its left and right sides.

Figure 5.7 The projectile penetration test rifle, and the projectile



(a) 22-caliber, long-range rifle

(b) Projectile.

Bond and pullout behavior of the fabric in binder are important factors governing multiple-cracking of ferrocement. Construction of large structures also requires overlapping of the fabric; the overlap (development) length of fabric also depends upon the bond and pull-out behavior of the fabric in binder. This investigation used the crack spacing in ferrocement tension test specimens which experienced multiple cracking to back-calculate the bond strength of fabric in binder. In addition, experiments were

also performed for direct measurement of the bond strength of the fabric reinforcement in cementitious binder. For this purpose, bond tests were performed on the 'Jute 2' fabric embedded in the indigenous pumice-lime binder with soda ash additive (Mix #8 in Table 2.2). Bond test specimens were prepared by placing one layer of fabric in one half with different embedment lengths (60, 90, 130, 170 mm) into the other half which incorporated two layers of the 'Jute 1' fabric reinforcement along its full length; this second half received the indigenous binder, which transformed it into ferrocement. The fabrics placed for preparation of the bond test specimen are shown in Figure 5.8a, and the test specimen comprising a ferrocement half and a fabric half with different embedment lengths of the fabric in the ferrocement half is shown in Figure 5.8b. Tension (bond) tests on the fabric embedded in ferrocement (Figure 5.9) produce either pullout or rupture of the fabric, depending on the embedment length of fabric. The minimum embedment length which induces rupture of the fabric provides the basis for assessment of the bond strength of the 'Jute 2' fabric in indigenous (pumice-lime with soda ash additive) binder.

Figure 5.8 Bond test specimen



(a) Fabrics placed for preparing the specimen

(b) Bond test specimen

Figure 5.9 Pullout test setup



5.4 Test Results and Discussion

Figure 5.10 presents typical tensile load-deflection and stress-strain curves for the 20 mm thick ferrocement test specimens with two layers of chicken mesh reinforcement, with stress calculated per unit area of the chicken mesh reinforcement. These specimens did not exhibit multiple cracking (Figure 5.11); the width of the first crack grew with increasing deformation on the descending branch of the load-deflection curve. The tensile strength of ferrocement is close to the tensile strength of its chicken mesh reinforcement tested alone. It should be noted that the chicken mesh test specimen exhibited a strain-hardening behavior where force increased above the yield level with increasing deformation. This could be attributed to the realignment of wires in chicken mesh along the direction of tensile loading, which could not happen in the confined condition within matrix in ferrocement. In short, the chicken mesh reinforcement in ferrocement determined the peak tensile load-carrying capacity of ferrocement, which was equal to the yield force of chicken mesh times the number of reinforcing mesh layers.

Figure 5.10 Typical tensile load-deflection behavior of ferrocement sheets with 20 mm thickness and 2 layers of chicken mesh

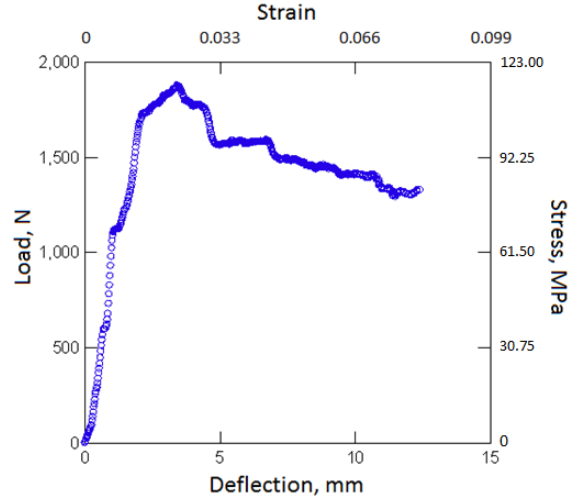


Figure 5.11 Failure of the first-generation ferrocement specimens with formation and growth of a single crack



Ferrocement specimens with 20 mm thickness and 2 layers of reinforcing fabric did not exhibit multiple cracking irrespective of the fabric type (chicken mesh, 'Jute 1' or 'Jute 2'). Table 5.1 shows calculation of the reinforcement volume fraction for 20 mm thick ferrocement sheets with 1 and 2 layers of reinforcement. With steel mesh, the reinforcement ratios of 0.0067 and 0.0134 are obtained here, which are low when compared with typical ferrocement reinforcement ratios [100]. It is thus not surprising that these first-generation ferrocement specimens did not exhibit multiple cracking. In the case of natural fabric, reinforcement ratios are higher than those for chicken mesh. One should, however, consider that the natural fiber (jute) yarns are relatively loose assemblies of fibers. Therefore, the yarns which

constitute the fabric, unlike steel wires in chicken mesh, incorporate a high degree of porosity. The fabric volume fraction is thus higher than the solid reinforcement volume fraction.

Table 5.1 Calculation of reinforcement ratios for 20 mm thick ferrocement sheets with 1 or 2 layers of different reinforcing fabrics

<i>Reinforcement Type</i>	<i>d_w (mm)</i>	<i>D_r (mm)</i>	<i>D_L (mm)</i>	<i>N</i>	<i>h (mm)</i>	<i>V_r</i>
Chicken mesh	1.6	20	60	2	20	0.0134
Chicken mesh	1.6	20	60	1	20	0.00670
Jute 1	1.2	1.5	1.5	2	20	0.151
Jute 1	1.2	1.5	1.5	1	20	0.0755
Jute 2	0.9	3	3	2	20	0.0424
Jute 2	0.9	3	3	1	20	0.0212

One can interpret the minimum reinforcement ratio requirement as the threshold above which a trend towards multiple cracking would be observed. In order to evaluate the reinforcement ratios presented in Table 5.1, approximate calculations of the minimum reinforcement ratios $(V_r)_{\min}$ for different reinforcement systems were performed using the equation presented earlier. The results, summarized in Table 5.2, indicate that minimum reinforcement ratios are about three times those obtained with two layers of different fabric types in 20 mm thick ferrocement sheets. In order to reach the minimum reinforcement ratios, thickness of ferrocement specimens was reduced to half (from 20 mm to 10 mm), and the number of layers was increased by 50% (from 2 layers to 3 layers). For comparison purposes, 10 mm thick specimens with 2 layers of fabrics were also tested. Table 5.3 presents the reinforcement volume fractions in 10 mm thick ferrocement specimens with 2 and 3 layers of different reinforcing fabrics. A comparison of Tables 5.2 and 5.3 suggests that at least three layers of each reinforcing fabric should be used in the 10 mm thick ferrocement sheet in order to exceed the minimum reinforcement ratio.

Table 5.2 Calculation of minimum reinforcement ratios for different reinforcing fabrics

Mesh	σ_{mu}	σ_{ru}	n	$(V_r)_{min}$
Chicken mesh	2.4	85	10	0.0379
Jute 1	2.4	22.6	8	0.421
Jute 2	2.4	25.1	3	0.140

Table 5.3 Reinforcement volume fractions in 10 mm thick ferrocement sheets with 2 and 3 layers of different reinforcing fabrics

Reinforcing Fabric	d_w (mm)	D_T (mm)	D_L (mm)	N (mm)	h (mm)	V_r
Chicken mesh	1.6	20	60	2	10	0.0268
Chicken mesh	1.6	20	60	3	10	0.0402
Jute 1	1.2	1.5	1.5	2	10	0.301
Jute 1	1.2	1.5	1.5	3	10	0.452
Jute 2	0.9	3	3	2	10	0.0848
Jute 2	0.9	3	3	3	10	0.127

Figure 5.12 presents typical load-deflection and stress-strain behavior of the 10 mm thick ferrocement specimen with three layers of 'Jute 2' burlap reinforcement, with stress expressed per unit area of reinforcement; this specimen exhibited multiple cracking (Figure 5.13). The load-deflection curve for this specimen exhibits a strain-hardening behavior followed by a stress plateau that corresponds to development of multiple cracks beyond the first crack. As expected, failure eventually occurs by growth of one of the cracks. Individual 'Jute 1' burlaps with a width similar to that of ferrocement specimens provided about 300 N peak load (see Figure 3.15 and Table 3.2). While the major trend towards nonlinear behavior in Figure 5.12 initiated at about 1,000 N (3 times the tensile load-carrying capacity of individual fabrics, noting that the ferrocement specimen has three 'Jute 2' fabric layers), the strain-hardening behavior of ferrocement almost doubled this load at peak. The tensile strength of ferrocement was more than twice (2.3 times) the tensile strength of its jute fabric reinforcement. One may hypothesize that the

supporting role of matrix (e.g., for redistributing stresses away from critically stressed yarns and regions of fabric, confinement of woven fabrics against realignment which could induce a composite behavior, and filling of the pores within yarns with cement hydrates) could enhance the fabric tensile strength in ferrocement versus the tensile strength of bare fabric. Although tests were conducted at a young age of 7 days, there were indirect indications of filling of yarn pores with cement hydrates; the yarns pulled out of mortar seemed to be stiffer than the as-received yarns.

The reinforcement volume fractions of the 10 mm thick ferrocement sheets with different reinforcement systems were very close to their theoretical minimum values (see Tables 5.2 and 5.3). Therefore, these ferrocement sheets may or may not exhibit multiple cracking. Actually, the ferrocement sheet with three layers of chicken mesh did not experience multiple cracking. Chicken mesh was found to be sensitive to the stress concentration generated at end grips; the single crack which was responsible for failure of ferrocement specimens with chicken mesh reinforcement occurred near the end grip (Figure 5.14a). This was not the case with the 'Jute 2' burlap reinforcement (Figure 5.14b) which seemed to provide a desired toughening effect and the ability to mitigate localization of damage at the highly stressed regions.

In the case of the 'Jute 1' burlap with 1.5 mm opening between yarns, considering that the sand size used in the mortar matrix had a maximum particle size of 1.5 mm, failure occurred by delamination of the mortar coating on the outer layer of burlap while some tendencies towards multiple cracking were also observed (Figure 5.15). This observation indicates that the maximum particle size of sand in mortar should be smaller than the fabric opening size. Reduction of the ferrocement sheet size to 10 mm pronounced the adverse filtering effect of the 'Jute 1' burlap with fine opening size against coarser sand particles. In this case, even with two 'Jute 1' burlaps, a brittle failure mode was observed (Figure 5.16) with a peak load that was smaller than twice the tensile load-bearing capacity of a single 'Jute 1' burlap tested in tension.

Figure 5.12 Tensile load-deflection and stress-strain curves for 10 mm thick ferrocement specimen reinforced with 3 layers of 'Jute 2' burlap

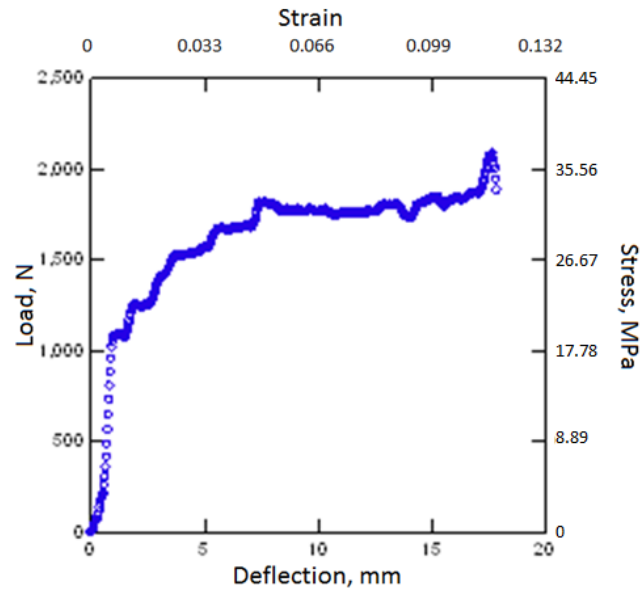


Figure 5.13 Multiple cracking of the 10 mm thick ferrocement specimen reinforced with 3 layers of 'Jute 2' in tension

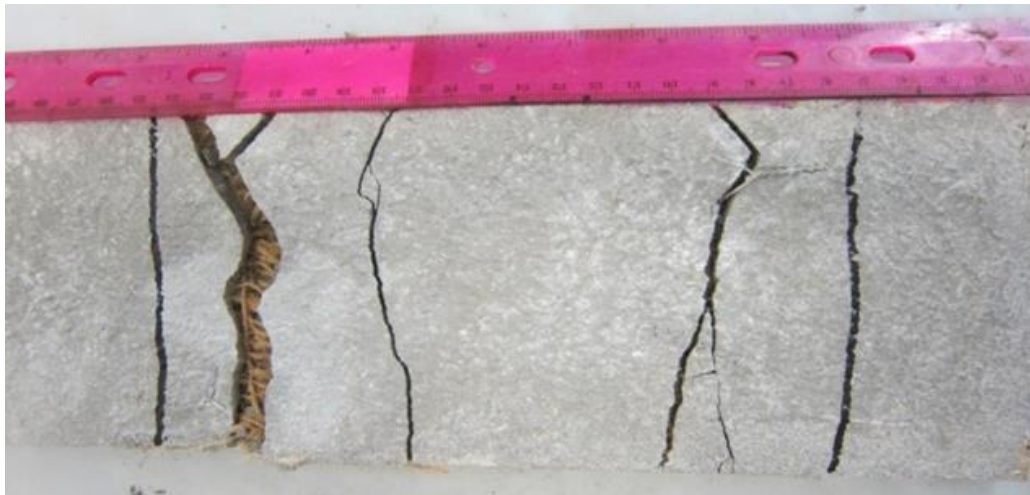


Figure 5.14 Tensile failure modes of under-reinforced ferrocement sheets with chicken mesh and 'Jute 2' burlap reinforcement

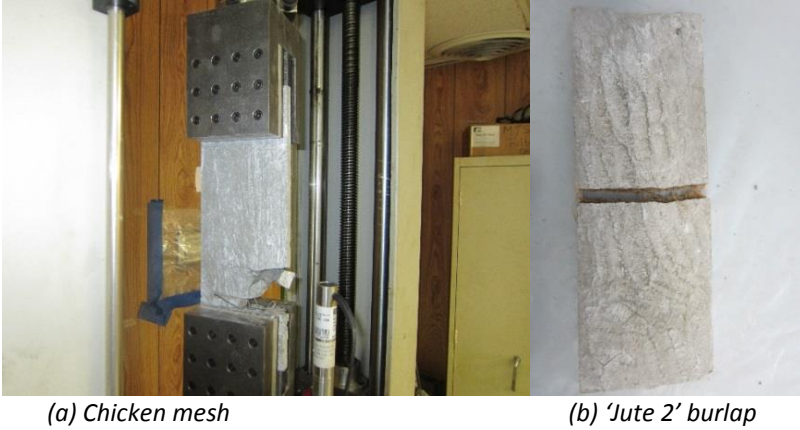
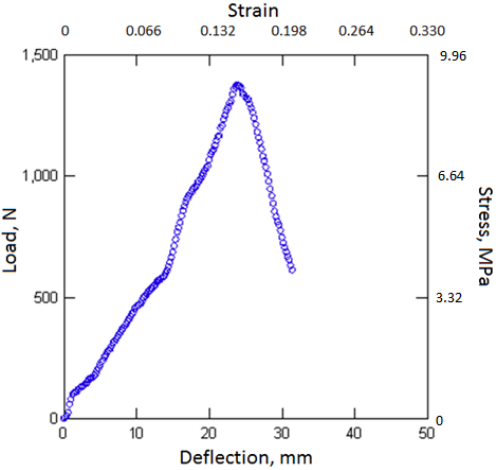


Figure 5.15 Delamination of the mortar coating on the outer layer of the 'Jute 1' burlap with fine opening size



Figure 5.16 Tensile load-deflection and stress-strain curves for a 10 mm thick ferrocement sheet with two layers of 'Jute 1' burlap with fine opening size



The bond strength between the reinforcing fabric and the mortar matrix depends upon interfacial interactions of the yarns and matrix as well as the mechanical interlocking of the 2D fabric within matrix. In order to estimate the bond strength between the 'Jute 2' burlap and the mortar matrix, average crack spacing was measured (Figure 5.17) for two 10 mm thick ferrocement specimens with three layers of 'Jute 2' burlap reinforcement which exhibited multiple cracking. The measured values of crack spacing were then used to back-calculate bond strength, τ , using the following equation (introduced earlier):

$$L_{avg} = \frac{\sigma_{mu} \cdot \gamma}{\tau \cdot S_{rl}}$$

Table 5.4 summarizes calculation of bond strength using the measured values of average crack spacing for the two specimens. Considering that only two specimens are considered here, one can estimate that the bond strength between the 'Jute 2' burlap and the mortar matrix is within the 1-2 MPa range.

Figure 5.17 Crack spacing in two ferrocement tension test specimens with 10 mm thickness and three layers of the 'Jute 2' burlap reinforcement

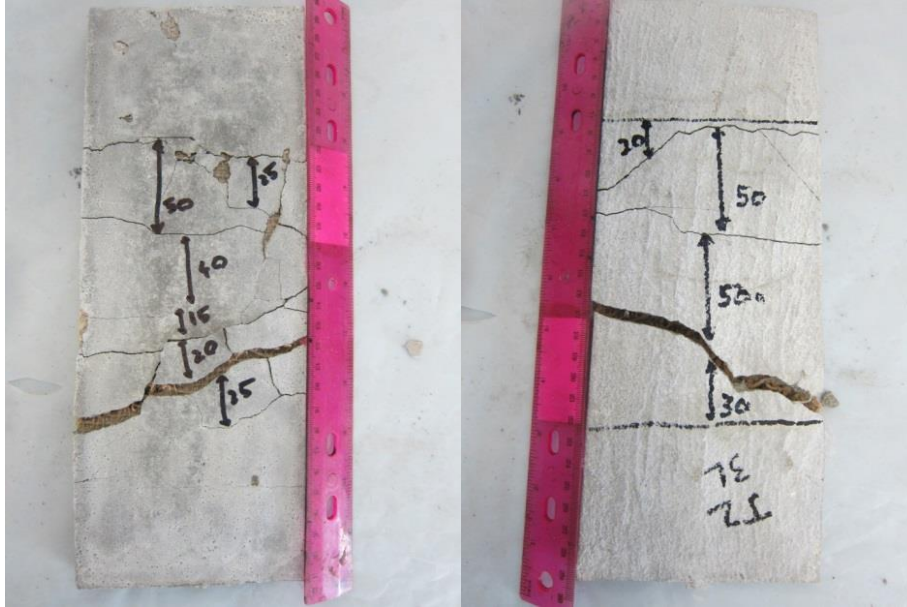
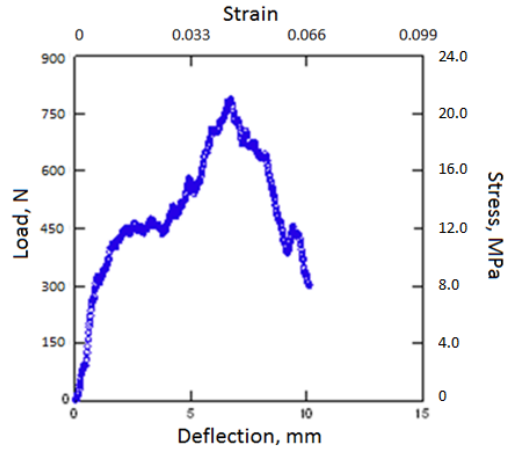


Table 5.4 Calculation of the bond strength of reinforcing fabric to the mortar matrix using the measured values of average crack spacing for the 10 mm thick ferrocement with three layers of 'Jute 2' burlap

σ_{mu} (MPa)	γ	S_{rl} (1/mm)	L_{avg} (mm)	τ (MPa)
2.4	1.5	0.094	25	1.5
2.4	1.5	0.094	35	1.1

Tension tests were also performed on indigenous ferrocement sheets comprising two 'Jute 2' fabric reinforcement in an indigenous pumice-lime matrix with soda ash reinforcement (Mix #8 in Table 2.2). The resulting tensile load-deflection curve is presented in Figure 5.18. Given the relatively low reinforcement ratio of this indigenous ferrocement sheet (two layers of 'Jute 2' reinforcement), it did not exhibit multiple cracking. It should be noted that a similar indigenous ferrocement sheet (but with three layers of 'Jute 2' reinforcement) was used as skin in sandwich composite experiments reported later

Figure 5.18 Tensile load-deflection and stress-strain behavior of an indigenous ferrocement skin with two layers of 'Jute 2' fabric reinforcement and indigenous pumice-lime matrix



The projectile penetration test conducted on the ferrocement sheet with 20 mm thickness led to complete penetration of the projectile into the ferrocement sheet (Figure 5.19). This is expected theoretically based on the following equation (introduced earlier).

$$P_c = \frac{56.6 \left(\frac{m}{D^3}\right)^{0.075} N m v^{1.8} \left(\frac{D}{c}\right)^{1.5} f_{age}}{D^2 \sqrt{f_c}} + D$$

For the projectile penetration test conditions considered in the project (D=5.7 mm, M=0.0023 kg, V=378 m/s, C=1.5 mm, $f_c=25$ MPa), the above equation yields a penetration depth of 118 mm, which exceeds the ferrocement thickness of 20 mm.

Figure 5.19 Pictures depicting the front and back of the ferrocement sheet where two projectiles entered and exited the specimen



In bond tests, specimens with 50 and 90 mm embedment lengths of the 'Jute 2' fabric failed by pullout of fabric (Figure 5.20a), while those with 130 and 170 mm embedment length failed by fabric rupture (Figure 5.20b). Figure 5.21 shows all test specimens after performance of bond tests. These results indicate that

130 mm is the minimum embedment (development) length which ensure that the full tensile strength of the fabric can be developed in the indigenous (pumice-lime) binder considered here. This is a reasonable requirement, and provides further support for the viability of the indigenous building system that is under development in the project. Figure 5.22 shows the load-deflection test data obtained in the bond test on the specimen with 130 mm embedment length of the 'Jute 2' fabric. Stress values are also shown in the figure per unit area of the 'Jute 2' fabric. The tensile strength measured in this task is very close to that of 'Jute 2' fabric measured earlier. This is expected since the embedment length of 130 mm caused failure by rupture of the fabric. The 'Jute 2' fabric comprises 0.9 mm diameter yarns with 3 mm spacing. There are thus 38 yarns within the 115 mm width of the bond test specimens. An embedment length of 130 mm thus translates into $13,960 \text{ mm}^2$ total bond surface area of longitudinal yarns. The nearly 300 N pullout force thus translates into a bond strength of $300/13,960=0.021 \text{ MPa}$. This is smaller than about 1 MPa bond strength derived based on the measured values of crack spacing in ferrocement tension test specimens which experienced multiple cracking. This could be partly attributed to the particular features of this non-standard bond test specimen which produced split cracking (Figure 5.23) at smaller embedment lengths of 50 and 90 mm. Without this failure mode, an embedment length smaller than 130 mm could feasibly produce fabric rupture (in lieu of pullout), which would yield a higher calculated value of bond strength.

Figure 5.20 Failure modes of pullout test specimens



(a) Pullout of fabric with 50 mm embedment length

(b) Rupture of fabric with 130 mm embedment length

Figure 5.21 Failed bond test specimens with different embedment lengths



Figure 5.22 Experimental load-deflection curve in bond test with 130 mm embedment length of 'Jute 2' fabric

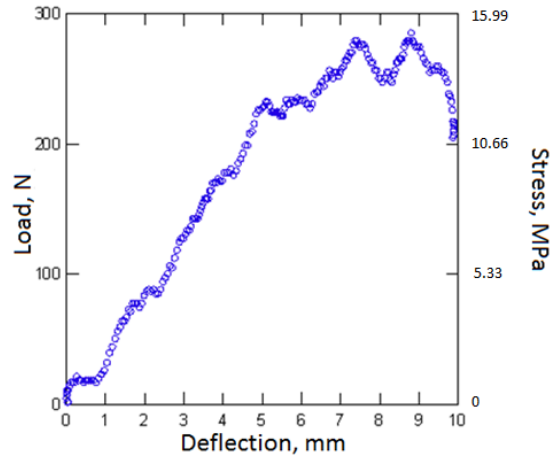


Figure 5.23 Failure by splitting of the ferrocement half of the bond test specimen with 50 mm embedment length



5.5 A Preliminary Assessment of the Indigenous Ferrocement Joint Performance

The building system which is subject of this investigation comprises sandwich composite panels with indigenous ferrocement skins, which are joined together to make the building system. Joining of the panels will be accomplished via overlapping of the indigenous reinforcement in ferrocement skins, and applying the indigenous inorganic binder (of ferrocement) to the overlapped reinforcement fabric. An initial assessment was made of the joint performance by making two ferrocement sheets, each reinforced with one layer of the 'Jute 2' burlap. Each ferrocement sheet was 10 mm thick, 100 mm long and 115 mm

wide, with each ferrocement reinforcement burlap extended 130 mm (the required development length found above) beyond the end face of the sheet. An indigenous matrix based on pumice-lime was used in this investigation. Ferrocement sheets were cured under a wet burlap for three days, and then the two 130-mm extended 'Jute 2' burlap lengths were overlapped (Figure 5.24a), and the pumice-lime matrix was applied to them. It should be noted that the joint area has two layers of 'Jute 2' burlap reinforcement, each extended from one of the two joined ferrocement sheets. It is thus expected to provide a higher tensile strength. The final specimen was cured under a wet burlap for three more days. It was subsequently exposed to 50% relative humidity at room temperature, and tested 14 days after joint formation. The specimen was then subjected to tension testing; it provided the full tensile strength expected from one layer of 'Jute 2' reinforcement in a 10 mm thick ferrocement sheet with 115 mm width. (~376 N).

DEVELOPEMENT AND CHARACTERIZATION OF INDIGENOUS AERATED CONCRETE

6.1 Introduction

Aerated concrete constitutes the lightweight core of the sandwich composite used in the project as the basic module for building construction. The aerated concrete should provide adequate mechanical properties (e.g., shear strength and modulus, tensile strength and strain capacity) to enable structurally efficient sandwich composite behavior. The aerated concrete core should also provide adequate insulation qualities, and should make viable contributions towards resistance of the sandwich composite against projectile penetration.

Aerated concrete comprises a cementitious matrix within which air bubbles are introduced (as replacement for aggregates in normal concrete) using a foaming agent. It should be noted that the air voids in aerated concrete are few millimeter in size, and the air content is 60-80 vol.%. The term concrete is used here because air in aerated concrete is viewed as the extreme limit of lightweight concrete where the void content of aggregates reaches 100 vol.%. One should also distinguish between the air bubbles entrained in concrete for freeze-thaw durability, which are an order of magnitude smaller in size and volume fraction when compare with the aerated concrete air bubbles. Aerated concrete uses foaming principles that are used in broad fields of application (Figure 6.1). Aerated concrete comprises foams that were formed and stabilized in the mixing water of concrete using a surfactant (surface active agent). Surfactants lower the surface tension of water (a phenomenon which allows for mixing of water and oil, which is used in soap to wash away oil). A foam inevitably forms in water carrying a surfactant. This is because the part of soap molecule that bonds well with oil also bonds well with air, forming air bubbles that stay stable. In this capacity, the surfactant in soap acts as an emulsifier, which refers to molecules that help normally repulsive ingredients (like water and air) to mix. Surfactants/emulsifiers are molecules with polar and nonpolar ends that attach to water and air, respectively. Figure 6.2 shows the process

through which surfactants form an individual air bubble in a foam. While water and air do not mix without a surfactant (Figure 6.2a), a surfactant enables formation of stable air bubbles within water (Figure 6.2b). This is the phenomenon which forms fine entrained air bubbles which enhance the freeze-thaw durability of concrete. Some surfactant molecules can stabilize larger air bubbles by orienting themselves on the interfaces of larger air bubbles with water (Figure 6.3).

Figure 6.1 Examples of foam applications (<http://www.molecularrecipes.com/culinary-foams/>).

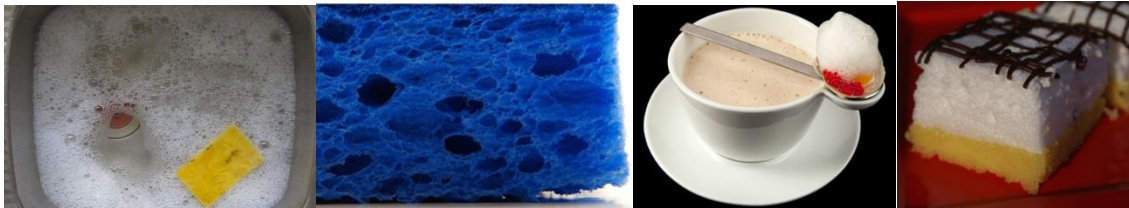


Figure 6.2 Formation of stable air bubbles in water in the presence of surfactant molecules

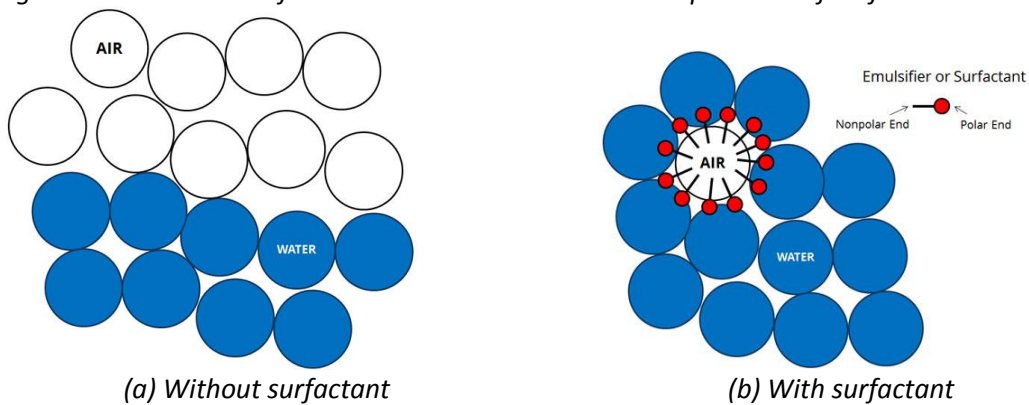
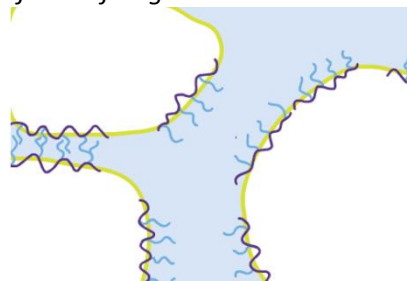


Figure 6.3 Stabilization of larger air bubbles by surfactant molecules which orient themselves on the interfaces of larger air bubbles with water



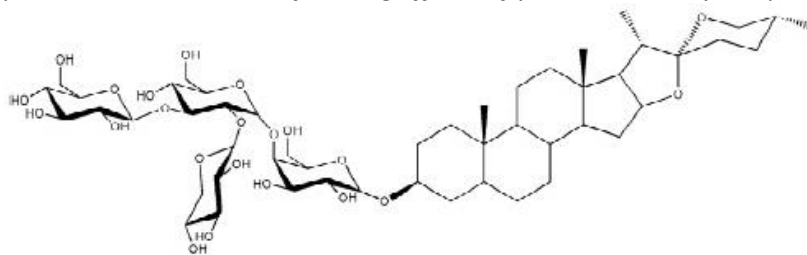
Considering the breadth of surfactant applications, they are available abundantly across the world. Two surfactants were evaluated as examples of those which are indigenous to the targeted geographic areas:

(i) saponin, a major constituent of plants such as caryophyllaceae, sapindus, aceraceae,

hippocastanaceae, gnostemma pentaphllum and ginseng (see Figure 2.5e,f); (ii) egg white; and (iii) liquid soap.

Saponins are natural surfactants found abundantly in various plant species. Saponin molecules (Figure 6.4a) are composed of a hydrophobic steroid or triterpenoid group, and one or several hydrophilic oligosaccharide chains attached to this group. Saponins are used in cosmetic, food and pharmaceutical products due to their excellent ability to stabilize emulsions and foams, and to solubilize bulky hydrophobic molecules. The saponin molecule shown in Figure 5.4a can be extracted from the residues of sisal defibring. It has been used in formulation of detergents [57]. Figures 5.4b and 5.4c show the foaming effects of birch leaves and horse chestnuts, respectively, caused by the presence of saponin.

Figure 6.4 A saponin molecule, and the foaming effects of plants caused by the presence of saponin



(a) Saponin molecule from sisal



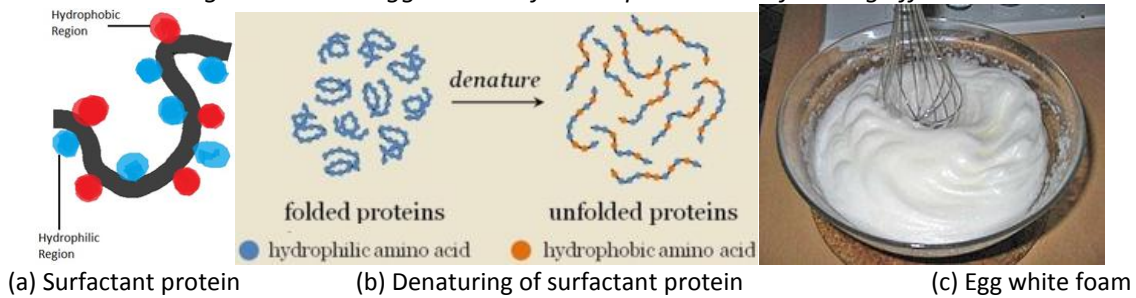
(b) Foaming effect of birch leaves



(c) Foaming effect of horse chestnut

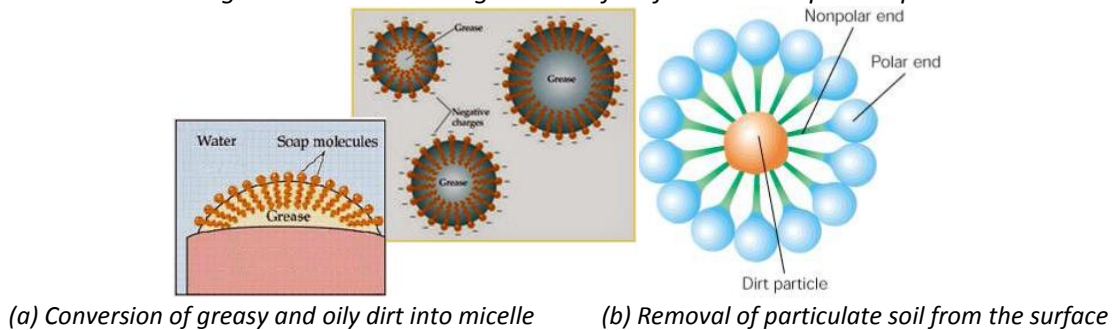
Egg white comprises largely of proteins with surfactant qualities (Figure 6.5a). When egg white is beaten, air is added and proteins are denatured (Figure 6.5b), exposing their hydrophobic and hydrophilic ends. The proteins align themselves between air and water, forming stable foams (Figure 6.5c). In addition, the proteins can bond to one another side-to-side as crosslinks which add to the foam stability.

Figure 6.5 The egg white surfactant proteins and foaming effect



Surfactants are also key constituents of liquid soaps, with the ability to stabilize air bubbles via the mechanisms depicted in Figures 6.2b and 6.3. Foaming, however, is a side effect rendered by the surfactants in liquid soap. A key function of surfactants in this application is to convert greasy and oily dirt into micelle that becomes dispersed in water (Figure 6.6a). Surfactants molecules group themselves around an oil droplet; the hydrophobic part of molecules projects into the droplet while the hydrophilic part remains in water. The oils is held in suspension by the emulsifying action of the surfactant, and is carried away with the dirty water. Surfactants also decrease the surface tension of water, making it a better wetting agent. Surfactants also remove particulate soil from the surface via electrostatic repulsion (Figure 6.6b).

Figure 6.6 The cleaning actions of surfactants in liquid soap



6.2 Experimental Program

6.2.1 Materials and Mix Designs

Four categories of aerated concrete were considered, which comprised: (i) Portland cement paste or mortar with egg white protein foaming agent; (ii) lime/gypsum mortar with liquid soap foaming agent;

(iii) lime/gypsum mortar with saponin foaming agent; and (iv) volcanic deposit/soda ash/lime paste with saponin foaming agent.

Type I Portland cement and hydrated lime were purchased from a local hardware store, and egg white and liquid soap were purchased from a local grocery store. Saponin and calcium sulfate hemi-hydrate were purchased from Sigma Aldrich.

Table 6.1 Mix designs (weight proportions) of aerated concrete materials

Mix #	Binder Composition	Foaming Agent	Binder	Foaming Agent	Water	Sand
1	Portland Cement	Egg White Protein	1	0.01	0.4	0
2	Portland Cement	Egg White Protein	1	0.02	0.7	0
3	Portland Cement	Egg White Protein	1	0.05	0.7	0
4	Portland Cement	Egg White Protein	1	0.05	1.0	0
5	Portland Cement	Egg White Protein	1	0.03	0.7	0
6	Portland Cement	Egg White Protein	1	0.03	0.7	1.0
7	Portland Cement	Egg White Protein	1	0.03	0.7	0.5
8	Portland Cement	Egg White Protein	1	0.025	0.7	0
9	Portland Cement	Egg White Protein	1	0.03	0.6	0.5
10	Portland Cement	Egg White Protein	1	0.03	0.5	0

6.2.2 Foaming and Mixing Procedures

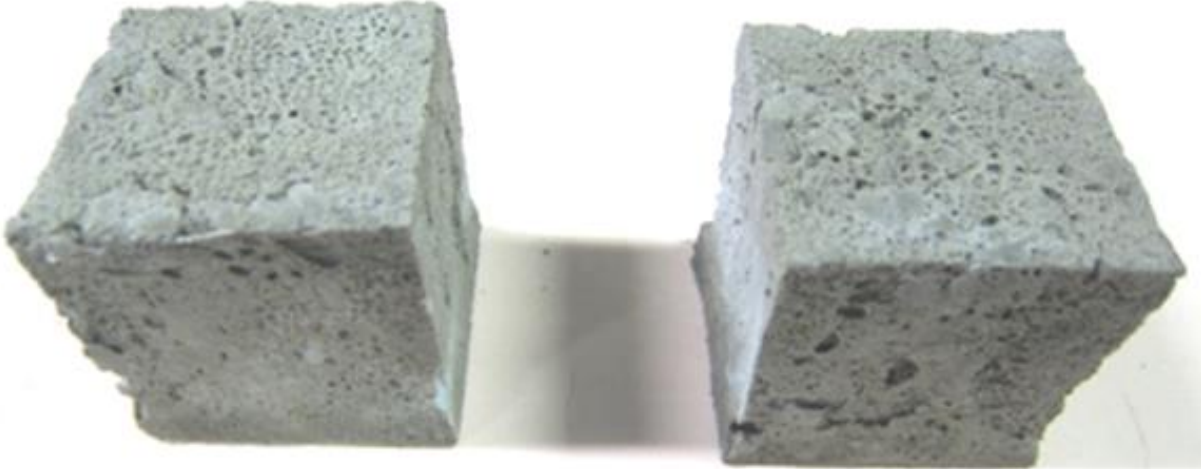
Foam was generated in water by adding the foaming agent (saponin, liquid soap or egg white) to water, and high-speed mixing of the solution at high speed (Figure 6.6). Mixing was continued until all water assumed the appearance of foam. Half of the mixing water was used in the case of saponin and liquid soap for generating the foam. Other mix ingredients were mixed separately in a mortar mixer; the foamed water was then added, and mixing was continued until a homogeneous aerated concrete was achieved (Figure 6.7).

Figure 6.7 Mixing of aerated concrete



The aerated concrete was molded into 50 mm cube specimens, which were kept under wet burlap for 3 days, and then demolded and stored at 50% relative humidity and room temperature until the test age of 7 days. Figure 6.8 shows examples of the cube specimens of aerated concrete.

Figure 6.8 Examples of aerated concrete specimens



6.2.3 Test Procedures

These cube specimens were used to measure the compressive strength of aerated concrete. Density of aerated concrete was calculated as weight divided by volume of cubes, and length change was measured as percent length change of cubes; these measurements were made at 7 days of age after 4 days of storage at 50% relative humidity. It should be noted that, depending on the cementitious material composition and the type of foaming agent, some aerated concrete specimens exhibited relatively large length change due to collapse of the foam system after molding.

Shear modulus is an important property of the (aerated concrete) core material in sandwich composites. A preliminary assessment of shear modulus has made by conducting compression tests on 2 cm cube specimens, where the compressive force and deformation in the loading direction were measured along with transverse deformation (Figure 6.9). The test data was used to calculate the elastic modulus and Poisson's ratio, and the shear modulus of aerated concrete. This test was performed after 14 days of curing on specimens of Mixes 22 and 30 in Table 6.1.

Figure 6.9 Compression testing of cube specimens with instrumentation for measurement of longitudinal force and deformation as well as transverse deformation

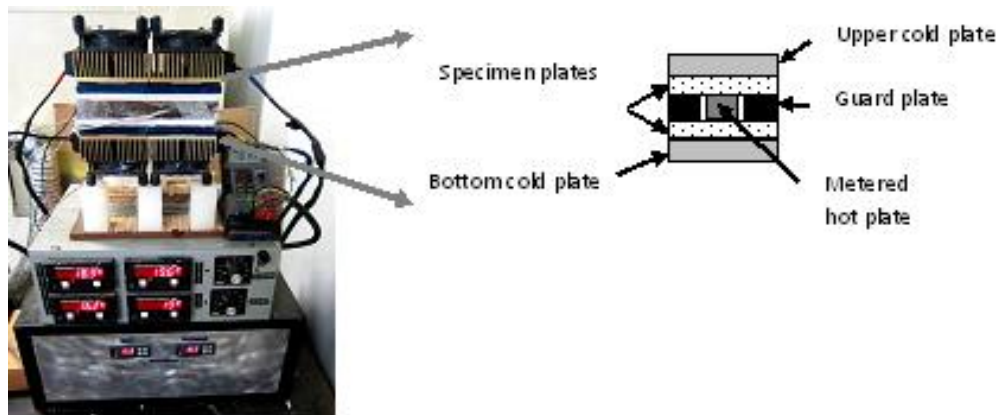


In the case of the lime-gypsum Mix #22 with saponin foaming agent, thermal conductivity tests were performed per ASTM C177 and C1045 on plate specimens with 13 mm thickness and 200mmx200mm planar dimensions. In this test (Figure 6.10) two plate specimens were sandwiched between cold and metered hot plates (with a guard plate). Steady-state temperatures were chosen to be 40°C for the measured area, and 25°C for the cold plates, representing the ambient temperature variations in the targeted geographic areas. When steady-state conditions were achieved, three successive readings were made, that were separated by at least 30 minutes. Heat flux and thermal conductivity were calculated as follows:

$$q = \frac{Q}{2A} \quad \& \quad \lambda = \frac{q}{\Delta TL}$$

Where, q represents heat flux, Q is power, A is the total metered area, λ is thermal conductivity; ΔT is temperature difference between the metered hot plate and the cold plate surfaces, and L is the thickness of the specimen.

Figure 6.10 Thermal conductivity test setup (insulation removed to show the specimens)



Split tension tests (Figure 6.11) were performed on the lime-gypsum Mix #22 with saponin foaming agent per ASTM C496, using cylindrical specimens of 152 mm diameter and 72 mm height. Flexure tests (Figure 6.12) were also performed on the Mix #22 specimens per ASTM C78 using prismatic specimens with 50mmx50mm cross-section and 285 mm total length. Flexural load and deflection data were collected using a load cell and a deflection transducer. A 60 mm thick cylindrical specimen of the Mix #22 aerated concrete was also subjected to projectile penetration test following the procedures outlined earlier for ferrocement sheets.

Figure 6.11 (A) Split tension test setup (B) failure mode

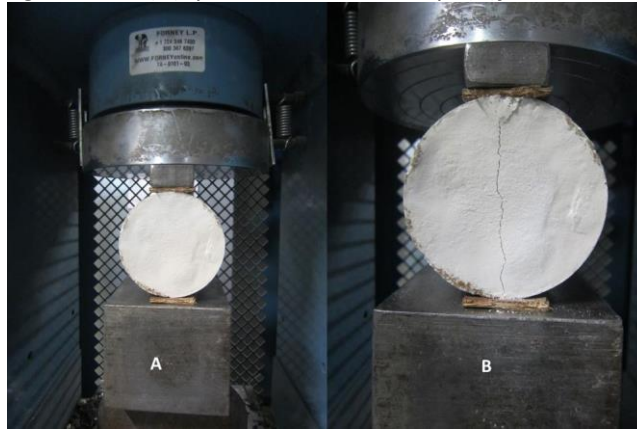
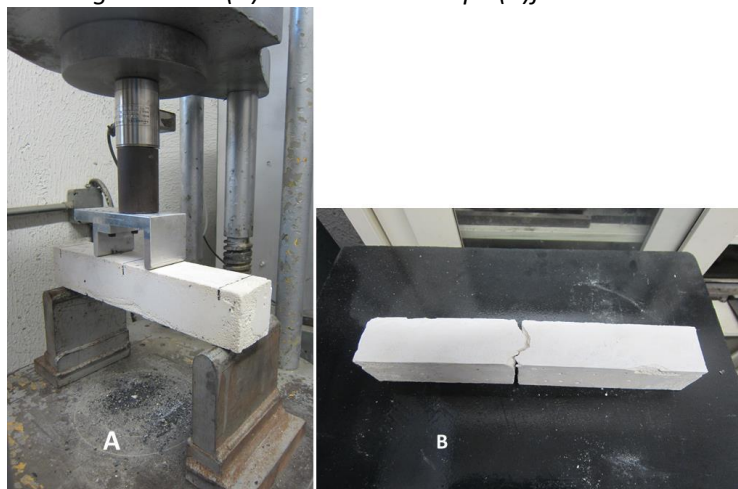


Figure 6.12 (A) Flexural test setup (B) failure mode



Sorptivity (rate of water absorption) tests were conducted on 10 cm height by 5 cm diameter cylindrical specimens per ASTM C 1585 (Figure 6.13). In this test, one surface of specimens is exposed to water, with all other surfaces sealed (Figure 6.13), and the gain in specimen mass caused by capillary sorption of water is measured as a function of time. Sorption is defined as the ratio of change in mass to the product of the water-contact area of the test specimen and the density of water:

$$I_t = \frac{m_t}{ad}$$

where l_t is sorption at time t , m_t is the change in specimen mass at time t , a is the exposed area of the specimen to water, and d is the density of water. Sorption tests were performed on lime-gypsum Mixes 22 and 30 in Table 6.1 with saponin and liquid soap foaming agents, respectively.

Figure 6.13 Sorption test specimens with one surface exposed to water



6.3 Test Results and Discussion

Aerated concrete specimens exhibited ductile failure modes in compression Figures 6.14a and 6.14b show a compression test cube prior to and after testing. The compressive strength, density and length change test results for different aerated concrete mixtures are presented in Table 6.2 and Figure 6.15. The role of aerated concrete as the core in sandwich composite which provides minimum shear strength and modulus to ensure sandwich behavior, and makes key contributions towards thermal insulation and projectile penetration resistance would probably be satisfied at lower densities ($\sim 0.5 \text{ g/cm}^3$). Stability of the foam structure during curing is also a key requirement in development of aerated concrete. Among mixtures considered in the experimental work on aerated concrete, Mix #22 (comprising a lime-gypsum matrix with saponin used as foaming agent) would probably satisfy these requirements. The 7-day compressive strength of this aerated concrete formulation is comparable with those reported in the literature (or deducted from the reported 28-day values) [88, 108]. The measured value of thermal conductivity for Mix #22 with 0.53 g/cm^3 density was $0.546 \text{ W m}^{-1} \text{ }^\circ\text{C}^{-1}$, which is of the same order of magnitude as those reported in the literature [108]. The 7-day split tensile and flexural strengths of the Mix #22 aerated concrete were 0.256 and 1.32 MPa, respectively. Both these values exceed the 7-day compressive

strength of this aerated concrete. The ratio of flexural-to-split tensile strength of aerated concrete (at 7 days of age) is also high when compared with normal concrete. These observations point at the ductility of the aerated concrete Mix #22, and its fundamentally different qualities (at least at 7 days of age) when compared with normal concrete. Figure 6.16 presents the flexural load-deflection behavior of the Mix #22 aerated concrete at age of 7 days.

Figure 6.14 Compression test cube prior to (A) and after (B) failure

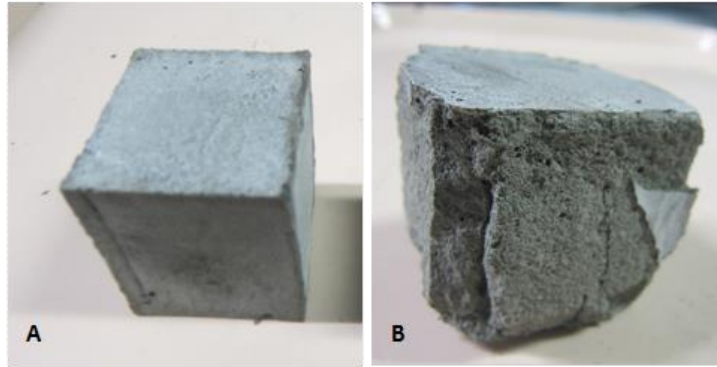


Figure 6.15 Compressive strength and density test results for different aerated concrete formulations

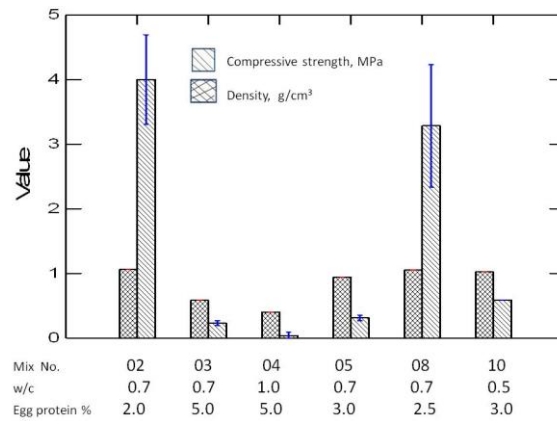
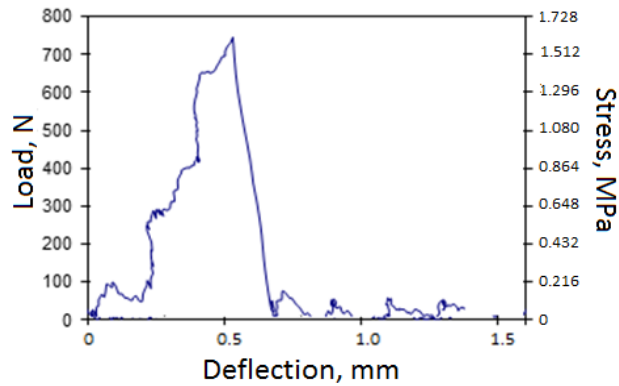


Figure 6.16 Flexural load-deflection behavior of the Mix #22 aerated concrete



The measured shear moduli of aerated lime-gypsum Mixes #22 and #30 with saponin and liquid soap foaming agents were 11 and 23 MPa, respectively. These values are two orders of magnitude greater than that of polyurethane foam used in sandwich composites (with fiber reinforced polymer composite skins); judicious selection of indigenous cementitious matrices could further increase the shear modulus of aerated concrete materials. This finding implies that the aerated lime-gypsum mixtures developed in the project probably provide adequate shear moduli for use in sandwich composites. The elastic moduli of Mixes #22 and #30 were 16 and 36 MPa, respectively, and the corresponding Poisson's ratios were 0.24 and 0.22.

Sorption test results for Mixes #22 and #30 are presented, as a function of the square root of time ($\text{sec}^{1/2}$), in Figure 6.17. Table 6.3 presents the initial and secondary sorptivity values for Mixes #22 and #30. With saponin as foaming agent, Mix #22 has a higher initial sorption rate than Mix #30 with liquid soap foaming agent. The secondary sorption rates of Mix #22, however, is smaller than that of Mix #30.

Figure 6.17 Sorption versus square root of time for Mix #22 (A) and #30 (B)

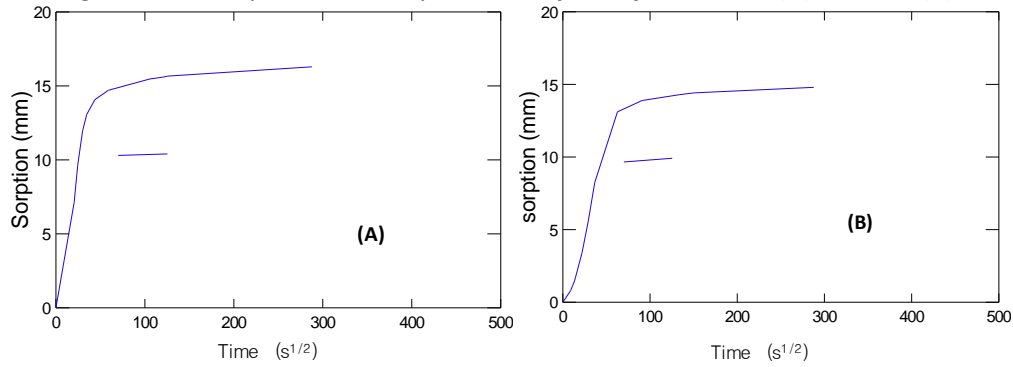


Table 6.2 Initial and secondary sorption rates of Mix #22 and #30

Mix #	Initial sorptivity (mm/s ^{1/2})	Secondary sorptivity (mm/s ^{1/2})
22	0.377	0.0029
30	0.239	0.0036

In projectile penetration tests, the projectile fully penetrated and exited the 60 mm thick aerated concrete (Mix #22) specimen. Figure 6.18 shows the entry and exit points of two projectiles shot at the same specimen. Full penetration into the 60 mm thick aerated concrete specimen is expected theoretically using the following equation (introduced earlier).

$$P_c = \frac{56.6 \left(\frac{m}{D^3}\right)^{0.075} N m v^{1.8} \left(\frac{D}{c}\right)^{.15} f_{age}}{D^2 \sqrt{f_c}} + D$$

For the projectile penetration test conditions considered in the project (D=5.7 mm, M=0.0023 kg, V=378 m/s, C=1.5 mm), and assuming $f_c=1$ MPa for the aerated concrete at the later projectile penetration test age, the above equation yields a penetration depth of 568 mm, which exceeds the aerated concrete thickness of 60 mm.

Figure 6.18 Entry and exit points of two projectiles shot at the same specimens



Important Note - The credits to this entire section must be given to Faris Matakah and Weerasiri

A PRELIMINARY DEVELOPMENT AND EVALUATION OF SANDWICH COMPOSITES

7.1 Introduction

A preliminary experimental work was conducted on sandwich composites in the course of developing the ferrocement skin and the aerated concrete core. This preliminary study was performed in order to better understand the production methods and failure conditions of sandwich composites, and identify those aspects of design that need to be emphasized in order to realize the full structural potential of the system.

7.2 Production of a First-Generation Sandwich Composite

A sandwich composite was prepared (Figure 7.1) with 20 mm skin thickness incorporating two layers of the 'Jute 2' burlap reinforcement, and 80 mm of aerated concrete core preparing using Mix #21 introduced in previous chapter with a relatively high density of 0.91 (see Table 6.1) and a 7-day compressive strength of 3.65 MPa (which was relatively high compared to other mixtures). This specimen (with 120 mm total height) had a length of 285 mm and a width of 110 mm. The specimen was prepared by sequential casting of the lower skin, the aerated concrete core, and the upper skin inside a mold. This specimen was prepared for testing in flexure. A projectile penetration test specimen was prepared similar to the flexure test specimen, except that the skins were reinforced with two layers of 'Jute 1' burlap (instead of the 'Jute 2' burlap used in the flexure test specimen).

Figure 7.1 The first-generation sandwich composite specimen



7.3 Evaluation of the First-Generation Sandwich Composite Behavior in Flexure and Under Projectile Impact

7.3.1 Flexural Behavior

Figure 7.2 presents the setup for flexure testing of the sandwich composite specimen. This ferrocement skin with two layers of 'Jute 2' burlap provides a peak tensile force of about 750 N, which was obtained in tension testing of a 10 mm thick ferrocement sheet with similar reinforcement (see Figure 5.18). With 100 mm center-to-center spacing of the upper and lower skins, the ultimate flexural strength of the sandwich composite, when failure is governed by tensile rupture of the lower (tensile) skin, would be $750 \times 100 = 75,000$ N.mm. In a four-point flexure test over a span of 250 mm, this flexural strength translates into $6 \times 75,000 / 250 = 1,800$ N peak load.

Under increasing flexural loading, initial cracking occurred in the aerated concrete core, starting just above the lower skin, which prompted cracking of the ferrocement skin (Figure 7.3a). Subsequently, with further increase in load, the tensile (lower) skin crack grew, and failure occurred by full-depth cracking of the sandwich composite (Figure 7.3b) at the section where core cracking initiated. Failure occurred by the growth of the initial crack, without any indication of multiple cracking. Full-depth cracking of the composite specimen indicates that delamination of skins led to the loss of sandwich composite behavior, with each skin acting independently in flexure. If the sandwich composite behavior would have continued without skin delamination, ultimate failure could have induced crushing of the top skin in compression.

The flexural load-deflection behavior of this sandwich composite specimen (Figure 7.4) indicates that the experimentally obtained peak load ($\sim 4,400$ N) is significantly higher than the theoretically predicted value of 1,800 N (which neglected the flexural behavior of skins and the contribution of core to flexural strength). The failure mode of this trial sandwich composite specimen under non-cyclic loading could be characterized as ductile. After removing the failed sandwich composite specimen, it was noted that the tension skin was fully debonded from the core. The aerated concrete core used in this sandwich composite

was of relatively high density and strength; it is thus expected to raise the flexural strength of the sandwich composite. Initiation of failure by tensile cracking of the aerated concrete core implies that the tensile strain capacity of the core was not adequate, which could be attributed to the relatively high density of this particular aerated concrete. Delamination of the tensile skin from the core is another factor which could compromise the flexural load-bearing capacity of the sandwich composite. These observations indicate that improved stress transfer at the skin-core interface and lowering of the density of the core could produce favorable effects on the failure mode and ductility of the sandwich composite; the flexural load-carrying capacity of the sandwich composite would benefit from improved interfacial stress transfer and increased strain capacity of a lower-density core; the lower strength properties of this core, on the other hand, could lower the flexural strength of the sandwich composite.

Figure 7.2 Sandwich composite flexure test setup



Figure 7.3 Failure mode in flexure of the first-generation sandwich composite

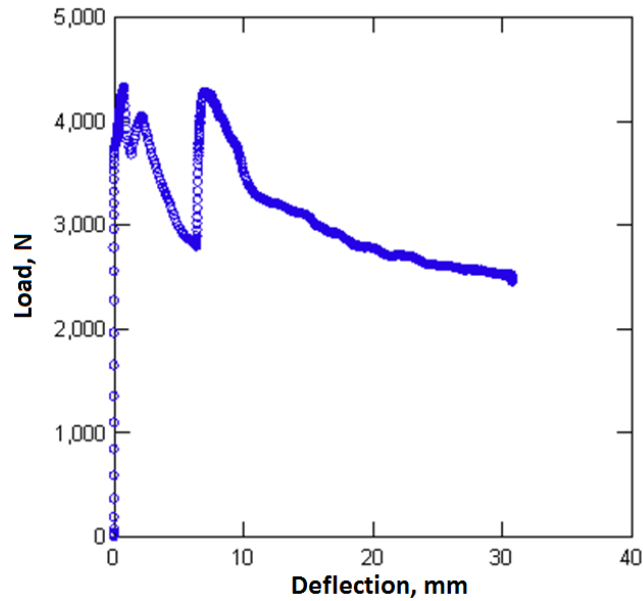


(a) Cracking of the aerated concrete core and tensile skin



(b) Failure by rupture of the lower skin followed by full-depth cracking of sandwich composite

Figure 7.4 Flexural load-deflection behavior of the sandwich composite



7.3.2 Behavior Under Projectile Impact

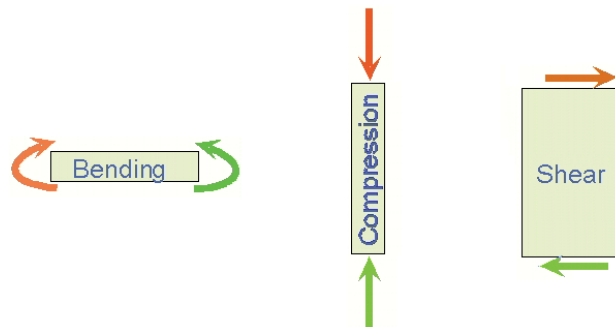
Projectile penetration testing of the sandwich composite followed the procedures outlined earlier in Chapter 5. The skin (which incorporated two layers of 'Jute 1' burlap with fine yarn spacing) experienced extensive cracking and delaminated from the core (Figure 7.5a). This was partly due to the use of 'Jute 1' burlap which was not thoroughly impregnated with the cementitious mortar used in ferrocement. The cracking and delamination of skin in this case effectively absorbed the kinetic energy of the projectile. Removal of the skin from the core (Figure 7.5b) indicated that the projectile only dented the core, but did not penetrate it.

PRODUCTION AND EVALUATION OF INDIGENOUS SANDWICH COMPOSITE

8.1 Introduction

Sandwich composites comprising indigenous ferrocement skins and indigenous aerated concrete core constitute the primary structural module for production of building systems with indigenous materials and resources. Live and dead gravity loads, and wind, blast and earthquake effects produce out-of-plane bending, in-plane shear, and axial compression forces (Figure 8.1) in the indigenous sandwich composite structural elements. An experimental program complemented with theoretical studies was implemented in order to assess these key aspects of the structural performance of indigenous sandwich composites, and to devise a theoretical basis for design of indigenous sandwich composite structural components. The outcomes of the preliminary experimental work reported in the previous chapter indicated that delamination of the ferrocement skin from the aerated concrete core could compromise the flexural performance of sandwich composite panels. Hence, as a first step, an experimental investigation was conducted to enable design of shear connectors which mitigate delamination of ferrocement skins from the aerated concrete core in the indigenous sandwich composite panels which are subject of this investigation.

Figure 8.1 Primary modes of the indigenous sandwich composite structural behavior



8.2 Development of Shear Connectors at the Ferrocement Skin/Aerated Concrete Core Interface

The preliminary work on sandwich composites reported in the previous chapter indicated that the ferrocement skin delaminated from the aerated concrete core in both flexure and projectile impact tests. Therefore, an experimental study was undertaken to mitigate the delamination failure mode in order to improve the structural performance of sandwich composites. Two strategies are commonly used ensuring the integrated behavior of composite skins and lightweight cores in sandwich composites [109-111]; one uses shear connectors (Figure 8.2a), and the other runs the skin material through the core as webs (Figure 8.2b). Both these options are viable in application to the indigenous sandwich composites that are under development in the project. Given the time constraints of the Phase I project, only the first option of shear connectors was considered here; chicken mesh was used as the indigenous shear connector in this project (Figure 8.3). It should be noted that the second (ferrocement web) option (Figure 8.2b), which was not considered in Phase I project, would also make important contributions to the flexural, shear and other modes of the sandwich composite structural behavior. The spacing of chicken mesh in Figure 8.3 is the primary consideration related to shear connector in design of indigenous sandwich composites which are integrated with shear connectors. This spacing would depend upon the contribution of chicken mesh to shear resistance across the ferrocement skin-aerated concrete core interface, which was determined experimentally.

Figure 8.2 The shear connector and web options for ensuring the integrated action of composite skins and the lightweight core in sandwich composites [111]

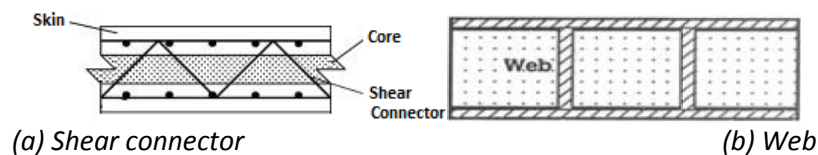
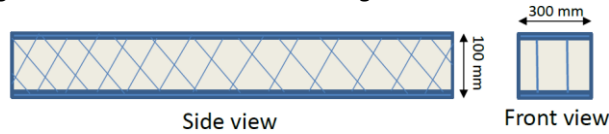


Figure 8.3 Chicken mesh as indigenous shear connector



The test specimen and loading condition for evaluating the contribution of chicken mesh to the shear transfer capacity of the ferrocement skin-aerated concrete core interface is schematically depicted in Figure 8.4 [112]. Pictures of the test specimen under load are presented in Figure 8.5. Specimens with 0, 1 and 2 layers of chicken mesh (used as shear connector) were tested. The aerated concrete in these test specimens was Mix #22 in Table 6.1 with lime-gypsum matrix and saponin as foaming agent. The ferrocement skin was 10 mm in thickness, and was made of the pumice-lime matrix with soda ash additive (Mix #8 in Table 2.2) with three layers of 'Jute 2' fabric reinforcement.

Figure 8.4 Schematic depiction of the test specimen and loading condition for measurement of the interfacial shear strength

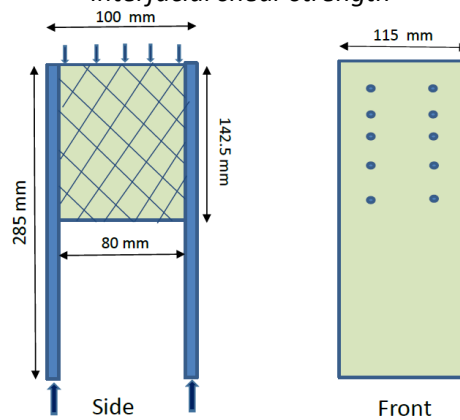


Figure 8.5 Interfacial shear test setup



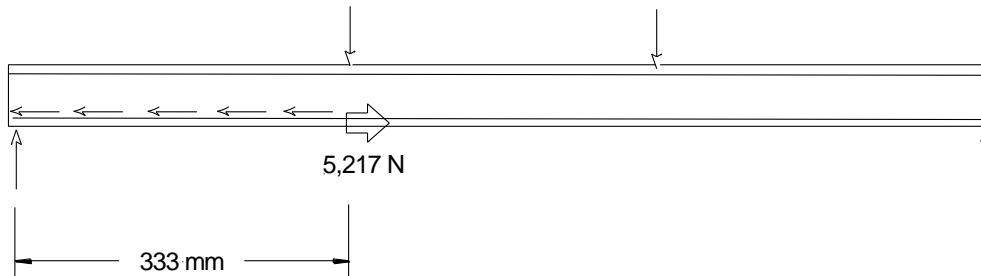
Specimens without shear connector failed in a brittle manner by debonding of ferrocement skins from the aerated concrete cores. Specimens with the chicken mesh used as shear connector exhibited a ductile behavior with the mesh pullout from skin and realignment of wires at the interface; complete pullout of mesh wires from the skin led to eventual delamination of the ferrocement skin. Figure 8.6 shows the damage mechanism during shear failure of the interface with shear connector. The measured values of peak force in shear tests on specimens with 0, 1 and 2 chicken mesh shear connectors were 816, 1,570 and 2,650 N, respectively. The contributions of chicken mesh shear connectors to interfacial shear strength are thus 754 and 1,834 N for specimens with one and two shear connectors. Total lengths of chicken mesh at the interface for specimens with one and two shear connectors are 285 and 570 mm, respectively. Hence, the average shear strength provided by a unit length of the chicken mesh shear connector is 2.9 N/mm. The adhesion shear capacity of 816 N, provided without any shear connector over two interface areas of 115mmx142.5mm translates into 0.025 MPa shear strength.

Figure 8.6 Damage mechanism during shear failure of the ferrocement skin-aerated concrete core interface with shear connector



The flexure test specimen introduced below has 10 mm thick skins of 300 mm width, with 3 layers of 'Jute 2' fabric in each skin. This skin provides a tensile load-carrying capacity of 5,217 N. These specimens will be tested over a span length of 1000 mm under four-point loading. Assuming that cracking of the tensile skin occurs under load, a tensile force of 5,217 N should not cause debonding at a 333mmx300mm interfacial area (Figure 8.7). The adhesion capacity at the 333mmx300mm interface area would be $0.025 \times 333 \times 300 = 2,498 \text{ N}$. This leaves $5,217 - 2,498 = 2,719 \text{ N}$ to be carried by the chicken mesh shear connectors. With the chicken mesh shear connector providing 2.9 N/mm shear load-carrying capacity at the interface, one would need a total chicken mesh length of $2,719 / 2.9 = 938 \text{ mm}$. For an interface with 333 mm length (Figure 8.7), this translates into $938 / 333 = 2.8$ layers of chicken mesh across the width of the sandwich composite test specimen. Therefore, 3 layers of chicken mesh should be used as shear connector in this sandwich composite structural element.

Figure 8.7 A simplified approach to interfacial shear stress calculation in four-point flexure testing of a sandwich composite panel with width (perpendicular to plane) of 300 mm

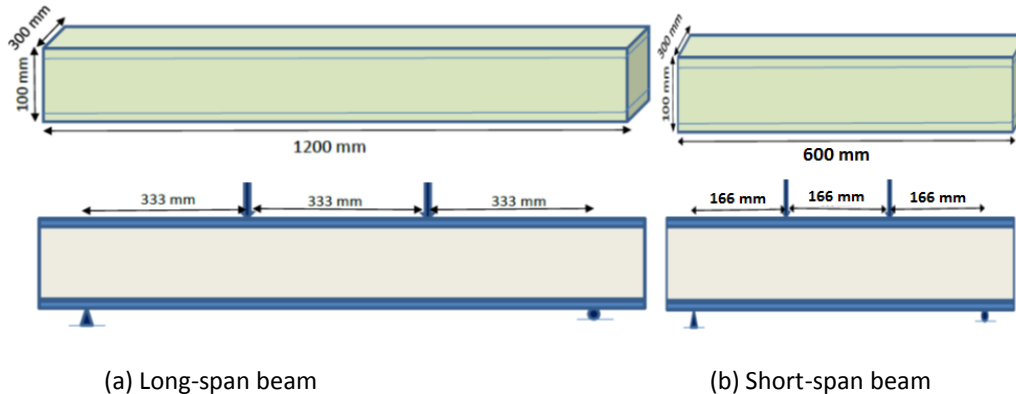


8.3 Production, Experimental Evaluation and Theoretical Analysis of the Indigenous Sandwich Composite in Out-of-Plane Loading

8.3.1 Design and Loading Conditions

The sandwich composite test panels with long and short spans, and the corresponding loading conditions are schematically depicted in Figure 8.8. The ferrocement skins in this sandwich composite are 10 mm thick, made using the pumice-lime binder with soda ash additive (Mix #8 in Table 2.2) incorporating three layers of the 'Jute 2' fabric reinforcement. The aerated concrete core in this sandwich composite is Mix #22 in Table 6.1 with lime-gypsum binder and saponin as foaming agent. The sandwich composite panels were tested under four-point loading.

Figure 8.8 Schematic depiction of the sandwich composite flexure test component and loading condition



8.3.2 Production

The flexure test component was produced in a mold (Figure 8.9a) by placing the lower ferrocement skin incorporating three layers of 'Jute 2' fabric with three chicken mesh strips installed as shear connectors (Figure 8.9b, placement of the aerated concrete core (Figure 8.9c), and placement of upper ferrocement skin (Figure 8.9d). The sandwich composite structural test component was cured under a wet burlap for 4 days, and then exposed to ambient conditions. Figure 8.10 shows the flexure test component after demolding.

Figure 8.9 Production of the sandwich composite flexure test component

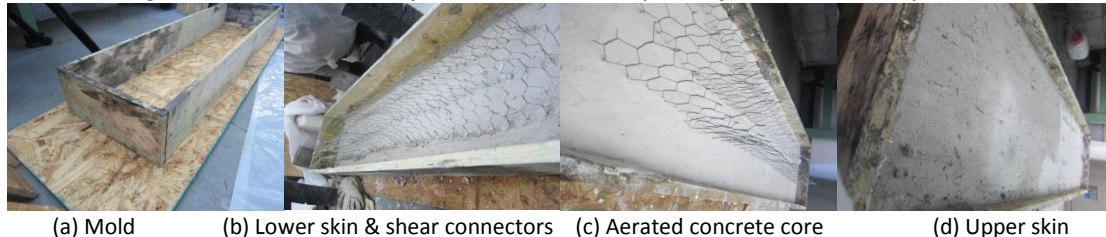


Figure 8.10 The indigenous sandwich composite panel



8.3.3 Experimental Evaluation

The long-span sandwich composite panel test setup is shown in Figure 8.11. Two deflection transducers were used to monitor midspan deflection; a load-cell recorded the applied load. Failure of this panel initiated with tensile cracking of the bottom (tension) skin (Figure 8.12a); additional cracks formed later in tension skin. With further increase in load, one critical crack propagated slightly along the skin-core interface, and then (as a flexural-shear crack) into the core (Figure 8.12 b). At this point, the top skin acted

nearly individually in flexure, and exhibited a flexural cracking mode of failure. The short-span panel test setup is shown in Figure 8.13a; its failure mode (Figure 8.13b) was similar to that of the long-span sandwich composite panel. Typical experimental load-deflection behavior of the long-span and short-span indigenous sandwich composite panels are shown in Figure 8.14a and 8.14b, respectively. The failure modes of these sandwich composite panels could be qualified as ductile. A strain-hardening type of behavior was observed after cracking of the tension skin; the panels also exhibited extensive deformation beyond peak load. The average peak loads of the long- and short-span indigenous sandwich composite panels were 1,200 and 2,750 N, respectively.

Figure 8.11 Long-span indigenous sandwich composite panel test setup



Figure 8.12 Failure mode of the long-span indigenous sandwich composite panel



(a) Initial cracking of tension skin

(b) Failure mode

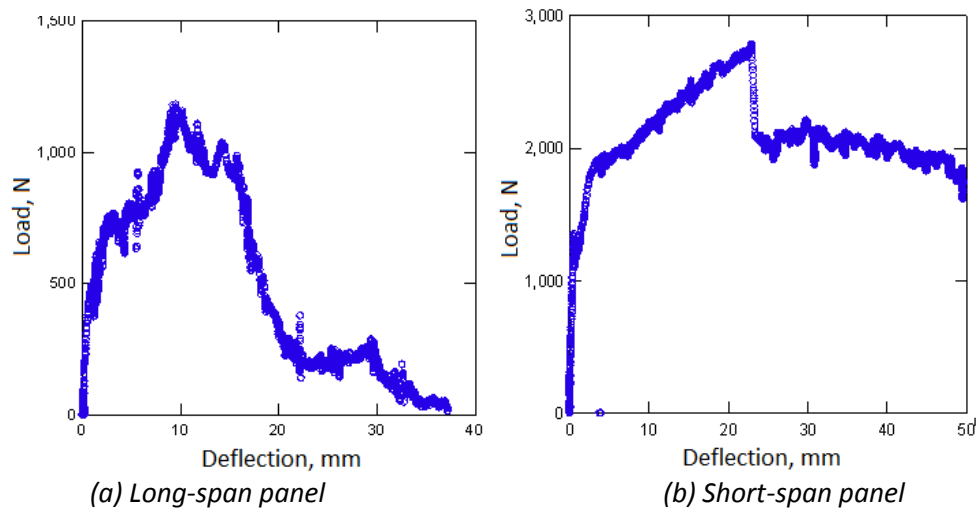
Figure 8.13 The short-span indigenous sandwich composite panel test setup and failure mode



(a) Test setup

(b) Failure mode

Figure 8.14 Typical load-deflection behavior of indigenous sandwich composite panels under out-of-plane loading



(a) Long-span panel

(b) Short-span panel

8.3.4 Theoretical Analysis

The sandwich composite panel subjected to out-of-plane loading is schematically depicted in Figure 8.15. The flexural mode of failure, which is preferred for maximum use of the structural qualities built into skins, would be governed by the failure of the tension skin. Beyond initial cracking of tension skin, its (burlap) reinforcement acts as the primary load-bearing element. The ultimate load corresponding to the flexural failure of the sandwich composite beam (which is governed by tensile failure of the indigenous ferrocement skin) can be conservatively estimated by neglecting the contribution of core as follows:

$$P_{fs} = 6\sigma_s \cdot b \cdot t \cdot d/L$$

For the indigenous ferrocement skin comprising 3 layers of 'Jute 2' with gypsum-lime matrix, with a width of 300 mm and a thickness of 10 mm, the skin ultimate tensile force, $\sigma_s \cdot b \cdot t$, is equal to 2040 N. This yields ultimate loads, P_{fs} , of 1653 and 3305 N for the long- and short-span panels (with 1000 and 500 mm span lengths), respectively. These theoretically predicted values should be compared with the experimental results of 1,200 and 2,750 N, respectively. The experimental results are 27% and 17% lower than the theoretical predictions. The flaws generated in scaled-up production of the sandwich composite panels partly explain the higher values of theoretical predictions when compared with experimental results.

The shear mode of failure in sandwich composites can occur via diagonal tension cracking of the core. The shear stress in core, τ_c , can be calculated as follows [113]:

$$\tau_c = \frac{P \cdot (E_s \cdot t \cdot \frac{d}{2} + E_c \cdot \frac{c^2}{8})}{2D}$$

where, D = effective flexural stiffness = $b \cdot t^3 \cdot E_s / 6 + b \cdot t \cdot d^2 \cdot E_s / 2 + b \cdot c^3 \cdot E_c / 12$, σ_s = skin (normalized) tensile strength, L = span length, E_s = elastic modulus of skin, E_c = elastic modulus of core, c = core thickness.

At the neutral axis, the diagonal tensile stress in core would be equal to the shear stress. Diagonal tension cracking of the core thus occurs at a load P_s where the stress calculated above reaches the tensile strength of the core, σ_{tc} :

$$P_s = \frac{2\sigma_{tc} \cdot D}{E_s \cdot t \cdot \frac{d}{2} + E_c \cdot \frac{c^2}{8}}$$

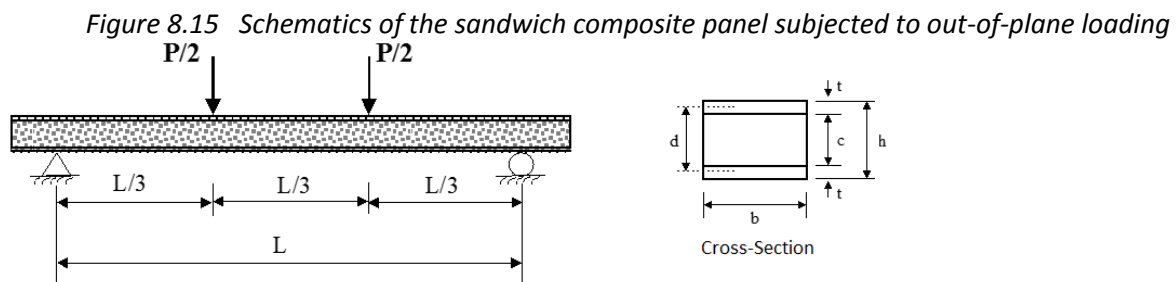
where, σ_{tc} is the tensile strength of the core. Experimental results generated in the project for the specific indigenous skin and core materials used in the sandwich composite panel indicated that the elastic moduli of the aerated lime-gypsum core and the indigenous ferrocement skin are 1,000 MPa and 10,000 MPa, respectively. The indigenous aerated lime-gypsum concrete core used in the sandwich composite provides a (split) tensile strength of 0.256 MPa. Inserting these values and the dimensions of the sandwich

composite beam in above equation yields an ultimate load corresponding to the core shear (diagonal tension) failure of 12,775 N, which is far greater than the theoretically predicted flexural strengths of 1,653 and 3,305 N. This theoretical finding confirms the experimental observation that failure occurs in flexure, governed by the tensile skin strength. It is worth mentioning that the shear connectors act as shear reinforcement in the core, and are expected to further rise the shear strength of sandwich composite panels.

The core flexural tension mode of failure occurs if the maximum tensile stress generated in the core by flexural action (at the tension skin-core interface) exceeds the tensile strength of the core. The peak load associated with this failure mode, P_{fc} , can be calculated as follows:

$$P_{fc} = \frac{D \cdot \sigma_t}{C \cdot L \cdot E_c \cdot c / 2}$$

where, σ_t = flexural strength of the aerated concrete core (measured at 1.32 MPa). The above equation yields ultimate loads, P_{fc} , of 48,488 and 24,244 N for long- and short-span panels, respectively. These values are far greater than the theoretically predicted ultimate loads corresponding to (tension skin) flexural failure of 1,653 and 3,305 N for long- and short-span sandwich composite panels, respectively. This theoretical finding supports the experimental observation that flexural failure of the sandwich composite beam governed by failure of the tension skin is the governing mode of failure.

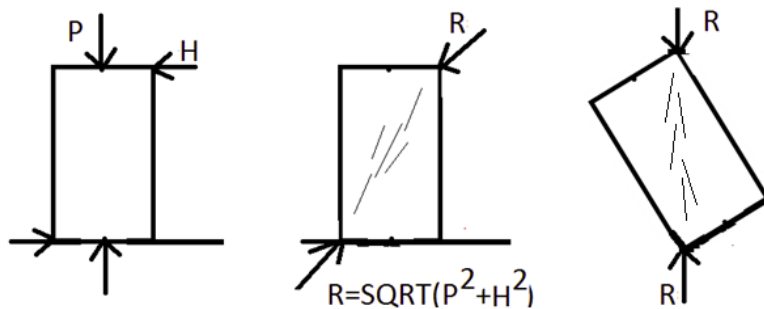


8.4 Production, Experimental Evaluation and Theoretical Analysis of the Indigenous Sandwich Composite Panel Subjected to In-Plane Shear

8.4.1 Design and Loading Condition

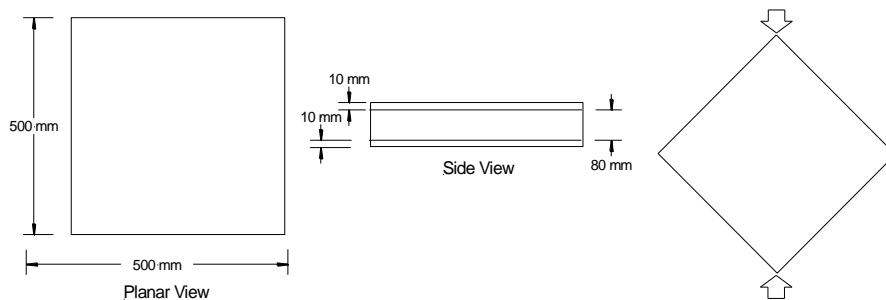
A sandwich composite wall subjected to lateral (in-plane) shear and gravity loading is shown in Figure 8.16a. The resultant force (R) representing this loading condition is shown in Figure 8.16b. The in-plane shear and gravity loads can thus be represented by a nearly diagonal compressive load (Figure 8.16c). Hence, this project investigated the in-plane shear behavior of sandwich composite wall panels by subjecting the sandwich composite test component shown in Figure 8.17a to compressive loading (Figure 8.17b).

Figure 8.16 Sandwich composite wall subjected to in-plane shear and gravity loads



(a) In-plane shear and gravity loads (b) Resultant force (c) Representative loading

Figure 8.17 The sandwich composite in-plane shear test component and loading condition



(a) Test component

(b) Loading condition

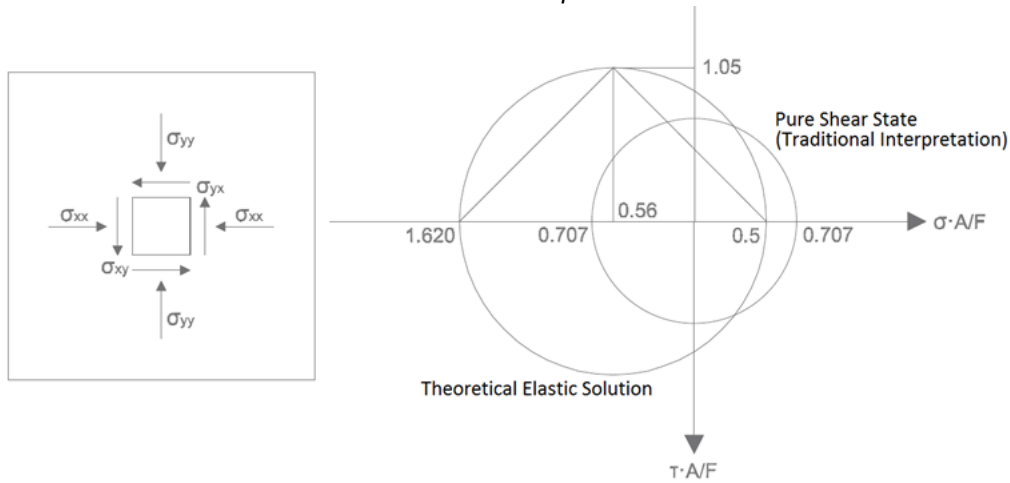
Traditionally, the diagonal compression test (Figure 8.17b) is used to evaluate the tensile strength of masonry panels, assuming that the diagonal cracking failure mode prevails. Tensile strength is calculated by assuming that the panel starts to collapse at its center when the principal tensile stress attains its maximum value. However, since different definitions of the stress field inside the panel can be found in the literature, the analysis of test results is subject to various interpretations (Figure 8.18) [114]. In the standard interpretation of the test, the diagonal tensile strength, f_{dt} , is obtained by assuming a uniform pure shear stress state. In this condition, the center of Mohr's circle is in the origin of the Cartesian axis, so the maximum principal (tensile) stress, σ_I , is equal to both principal compression, σ_{II} , and shear stress, σ_{xy} ($\sigma_I/\sigma_{II}=-1$ for the loading direction angle of 45°). As a consequence, the value of f_{dt} is computed as: $f_{dt}=0.707 \cdot F_{max}/A$.

A different interpretation of the diagonal compression test has been proposed recently, assuming that the stress field in a square panel with diagonal compression is not uniform. As demonstrated theoretically and numerically, the elastic solution provides the following stress state at the center of a panel subjected to a diagonal load: $\sigma_{xx}=\sigma_{yy}=0.56F/A$ $\sigma_{xy}=1.05F/A$ According to this, the principal stresses at the center of the panel are different ($\sigma_I/\sigma_{II}\approx-0.3$ for the loading direction angle of 45°): $\sigma_I=0.5F/A$ $\sigma_{II}=-1.62F/A$, and the actual value of f_{dt} is calculated as: $f_{dt}=0.5F_{max}/A$. In this context, the limit strength domain can be defined only on the basis of tensile strength. More specifically, the shear strength may be evaluated as: $\tau_{0d}=f_{dt}/1.5$

In addition to strength performance, it is also important to analyze the deformation capacity of the panel, which is the reference parameter within a performance-based seismic design [114]. Particularly, with ϵ_c and ϵ_t referring to compressive and tensile strains, respectively, the tangential strain can be expressed as: $\gamma = \epsilon_c + |\epsilon_t|$ where the two addenda are calculated from the relative displacement between two control points in each diagonal. Numerical analyses have indicated that the influence of the control point location is negligible. Also, assuming the control point at the panel corners, the tangential strain does not change

significantly; if the compressive strain is greater, due to the high stress close to corners, the tensile strain would be lower as strains are negligible in unloaded corners. As a consequence, with the aim of determining (from the global response of the panel) the shear modulus of the material, the apparent shear modulus of the panel, G^* , has been defined as the secant stiffness of the linear elastic branch until the occurrence of the first crack [114]: $G^* = (\tau_{el} - \tau_i) / (\gamma_{el} - \gamma_i)$ where, τ_i is taken (in tests on masonry panels) as 0.015 MPa and τ_{el} corresponds to the point on the curve where the first crack occurs in the panel.

Figure 8.18 Interpretation of the diagonal compression test: stress at the center of the panel in Mohr's representation



8.4.2 Production

The square sandwich composite panel for performance of the diagonal compression test was prepared similar to the flexure and compression test component using a square mold (Figure 8.19a). The production process involved placement of the lower ferrocement skin with chicken mesh shear connectors (Figure 8.19b), placement of the aerated concrete core (Figure 8.19c), and finally placement of the upper ferrocement skin. Similar to flexure and compression test components, curing was accomplished under a wet burlap for 4 days; the square test component was then exposed to ambient conditions.

Figure 8.19 Production of the square sandwich composite component for performance of diagonal compression tests



(a) Square mold

(b) Placement of lower skin and shear connectors

(c) Placement of core

8.4.3 Experimental Evaluation

The experimental setup for application of diagonal compression to the sandwich composite panel is shown in Figure 8.20a. A servovalve-controlled hydraulic test system was used for application of the diagonal compression load at a quasi-static rate of deformation. A load cell and a displacement transducer (oriented along the loading direction) were used to collect load and deformation data throughout the test. Failure occurred by diagonal cracking of the sandwich composite panel along the loading direction (Figure 8.20b). Failure of the panel under diagonal compression loading was ductile. The experimental load-deflection curve shown in Figure 8.21 depicts an ascending load branch after initial cracking, followed by a ductile post-peak behavior. The ductile tensile behavior of the indigenous ferrocement skins can be used to explain the ductile behavior of the panel under diagonal compression which reflects upon its in-plane shear behavior. This is advantageous towards dissipation of the energy input to the building structure by extreme events such as severe earthquakes.

Figure 8.20 Diagonal compression test setup, and failure mode of the indigenous sandwich composite

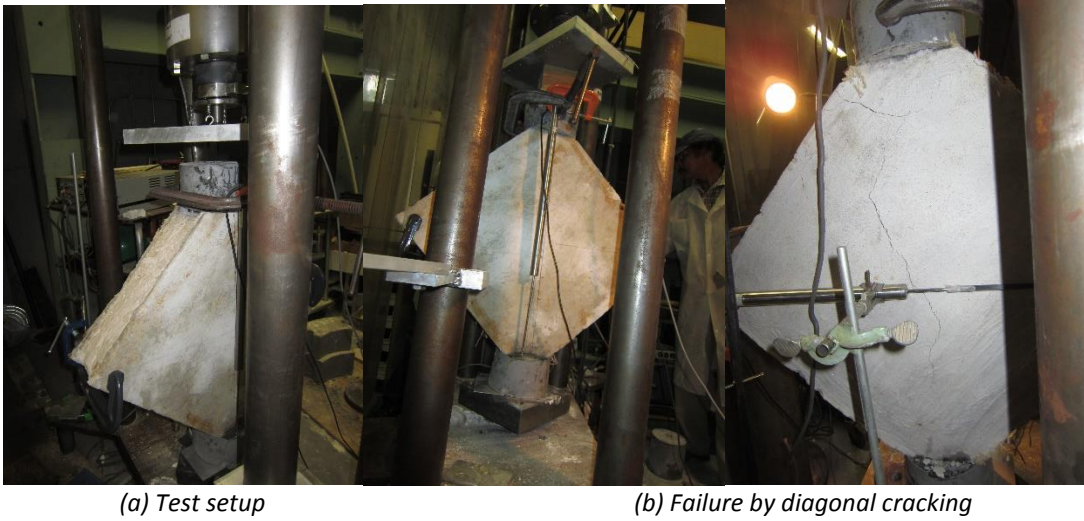
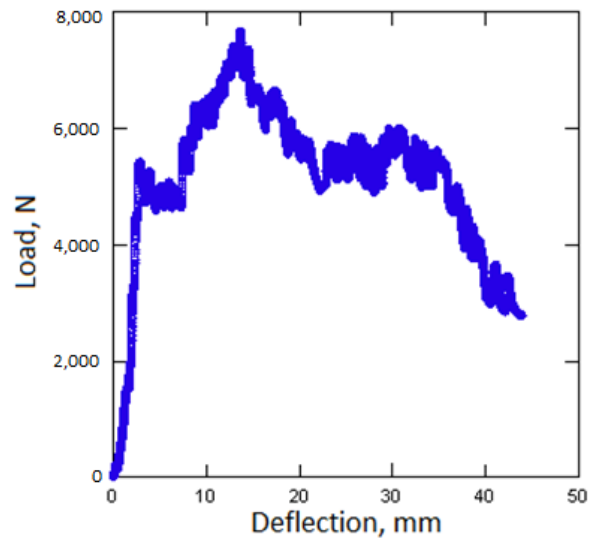


Figure 8.21 Load-deflection behavior of the indigenous sandwich composite panel subjected to diagonal compressive loading



8.4.4 Theoretical Analysis

The average compressive stress, σ_c , generated in the direction of loading at the center of the sandwich composite panel subjected to diagonal compression can be estimated as:

$$\sigma_c = \frac{0.707P}{A}$$

The traditional (pure shear) interpretation of the diagonal compression stress condition (see Figure 8.14) implies that the resulting principal tensile stress, σ_t , is equal to the compressive strength. The theoretical elastic solution shown in Figure 8.14, on the other hand, implies that $\sigma_t = 0.31 \sigma_c$.

Assuming that only ferrocement skins contribute to the diagonal tensile resistance of sandwich composite, the tensile strength and cross-section area to be used for calculation of the ultimate diagonal compression load are 0.68 MPa and 10,000 mm², respectively. The pure shear (traditional) and the theoretical elastic solution would thus yield the following values of ultimate load in diagonal compression [114]:

$$P_{u,pure\ shear} = \frac{\sigma_{tu} \cdot A}{0.707} = \frac{0.68 \times 10,000}{0.707} = 9,618\ N$$

$$P_{u,elastic\ solution} = \frac{\sigma_{tu} \cdot A}{0.5} = \frac{0.68 \times 10,000}{0.5} = 13,600\ N$$

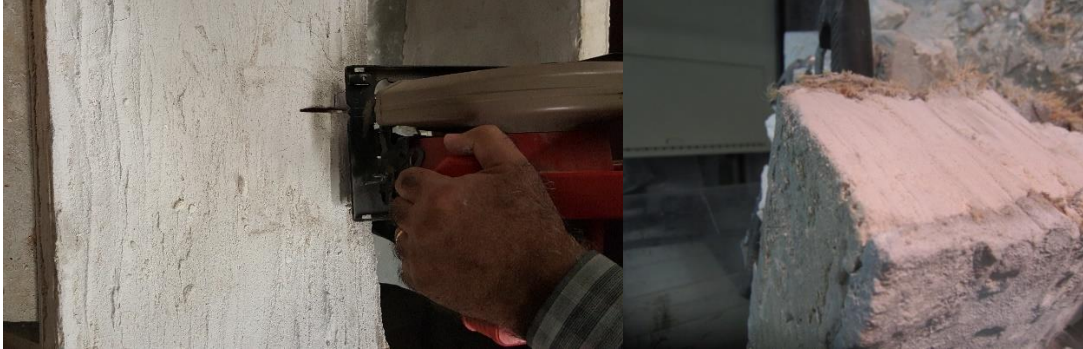
The measured value of ultimate diagonal compression load is 7,850 N. Given the cracking and inelastic behavior exhibited by the indigenous sandwich composite panel prior to reaching the peak load, it seems that the elastic solution does not suit analysis of the system. On the other hand, the traditional (pure shear) analysis yields a peak force that is closer to the experimentally measured value; the test result is 18% below the theoretical prediction. This difference can be partly explained by the imperfections introduced during scaled-up production of the indigenous sandwich composite structural panel.

8.5 A preliminary Assessment of the Ease of Demolition

The sandwich composites which constitute the primary module for construction of the building system comprises thin-sheet ferrocement skins with indigenous (e.g., jute burlap) reinforcement and an aerated concrete core. The primary load-bearing structural elements in this system are the thin-sheet ferrocement skins. A trial was made to cut through these thin sheets (and the aerated concrete core) using a circular saw (2 ¼ horse power) with a diamond turbo blade. As shown in Figure 8.22a, the circular saw could cut

through the sandwich composite. The resulting cut surface is shown in Figure 8.22b. The cut sandwich composite can be recycled as a building module, or can be discarded as a mineral product with no environmental hazards.

Figure 8.22 Cutting of the indigenous sandwich composite using a circular saw with a diamond blade



(a) Cutting the sandwich composite (top view)

(b) The cut surface

SUMMARY AND CONCLUSIONS

9.1 Introduction

The main thrust of this project is to develop building systems which employ locally available resources to efficiently meet the structural (load-bearing), protective (projectile penetration resistance and energy absorption), moisture barrier, weathering resistance, thermal insulation, fire resistance, health and sustainability requirements of modern building systems. A sandwich composite is devised as the primary module for development of the building system. This sandwich composite comprises indigenous ferrocement skins and an indigenous aerated concrete core. Indigenous cementitious binders play an enabling role in development of the sandwich composite building module. Strategies were devised for development of cementitious binders using indigenous raw materials which are abundantly available in Africa, middle east and elsewhere. These strategies emphasize simple processing of raw materials using locally available resources. The raw materials selected for development of indigenous cementitious materials include volcanic deposits, lateritic clay, gypsum, limestone, soda ash, and natron. Other abundant raw materials that could be used for this purpose include potash (soluble potassium salts), sodium sulfate (thenardite) and its hydrate (mirabilite) constitute. Various indigenous plant extracts could also be used as additives in cementitious materials to impart foaming, set retardation, activating and other effects. Examples include saponin foaming agent (from caryophyllaceae an sapindus), citric acid set retarder (from agave and opuntia), and oxalic and acetic acid activator (from boursapastoris).

9.2 Indigenous Cementitious Binders

Volcanic deposits are aluminosilicates with different calcium and iron oxide contents, alkalinities, degrees of crystallinity and reactivity. alkalis. Such aluminosilicate compounds can be transformed into inorganic, cementitious binders via dissolution and precipitation steps using different activators. Various indigenous activators could be used with volcanic deposits, including soda ash and natron which, due to their higher

alkalinity, offer greater capabilities for dissolution of volcanic ash and precipitation of inorganic binders including alkali aluminosilicate hydrate. In order to expand the range of indigenous 'cementitious' binders for diverse regions of Africa, middle east and the rest of the world, the more challenging task of activating volcanic deposits with lime was undertaken in Phase I project. Aluminosilicates such as volcanic deposits can, in a lime solution, undergo dissolution and precipitation processes which yield a 3D calcium aluminosilicate hydrate (C-A-S-H) structure with desired binding attributes. The 3D structure of C-A-S-H provides it with enhanced mechanical, stability and binding qualities when compared with calcium silicate hydrate (C-S-H), the primary binder in Portland cement concrete, or Portlandite ($\text{Ca}(\text{OH})_2$) formed in the course of Portland cement hydration. It should be noted that lime activation of aluminosilicates also generates C-S-H. Successful lime activation of volcanic deposits is projected to yield a cementitious binder comprising a combination of C-A-S-H and C-S-H. Volcanic powders of pumice and red lava with less than 125 μm particle size were used in the experimental work. Lime and quick lime were used as activators. Soda ash (Na_2CO_3) was used as an accelerator in lime-aluminosilicate binders; it is feasible that they raise the alkalinity of the solution, thereby enhancing the dissolution of aluminosilicate precursors and formation of precipitate binders (C-A-S-H and probably N,C-A-S-H), which benefit both the short- and long-term properties of the inorganic binder. Gypsum was the other additive used for enhancing the dissolution of alumina-carrying compounds. Natural sand was used as filler in the lime/volcanic powder mixtures. Early-age compressive strength test results indicated that pumice/lime binders which incorporated soda ash as additive produced viable levels of compressive strength. Microstructural, chemical and mineralogical analyses of pumice and the pumice/lime binder indicated that the binder and particularly pumice are largely amorphous. Chemical composition of the binder supports the presence of C-A-S-H and C-S-H; the amorphous nature of binder, however, prevents identification of these compounds via XRD analysis. The crystalline species identified in the binder include calcite, portlandite and iron carbonate hydroxide.

Gypsum is an abundant natural resource, which can be simply and sustainably converted into a hydraulic binder. Gypsum binder, however, are moisture-sensitive. The strategies evaluated in the project for enhancing the moisture resistance of gypsum include blending with lime (another indigenous binder) to produce Portlandite which yields stable calcite binder via reaction with the carbon dioxide in air, and use of additives such as citric acid which control the rate of setting and alter the crystallization kinetics and the morphology of gypsum crystals. Early-age compressive strength test results indicated that the addition of lime at gypsum: lime ratio of 0.8: 0.2 and the use of citric acid at 2% by weight of the solid binder yielded viable levels of early-age compressive strength. Testing at early age, however, did not allow for extensive carbonation of lime to significantly enhance the moisture resistance of gypsum. Microstructural, chemical and mineralogical analyses indicated that gypsum crystalline needles are the primary binders at early age; early indications of the evolution of Portlandite into calcite via carbonation reactions could be detected. Calcined (thermally treated) kaolinite clay is a reactive aluminosilicate precursor which, upon exposure to alkaline solutions, transfer into a high-performance alkali aluminosilicate hydrate (geopolymer) binder via dissolution, condensation and polycondensation steps. Calcination of kaolinite clay activates clay by distorting its structure via dehydration. This project focused on the use of laterite clay to avoid or reduce the need for heat treatment of clay, and employed soda ash and lime as alkali activators for production of indigenous geopolymer binders. Laterite clays are soil types rich in iron, aluminum and kaolinite clays, formed in hot and wet tropical areas. Lateritic soils can be described as $\text{Fe}_2\text{O}_3\text{-Al}_2\text{O}_3\text{-SiO}_2\text{-H}_2\text{O}$ matrices made from kaolinite in which a high portion of Al^{3+} is replaced with Fe^{2+} or Fe^{3+} . This replacement transforms the structure of kaolinite into a more amorphous and reactive product. It is postulated that, in the deep layers of laterites fed by Fe^{3+} solutions, the protons required to dissolve kaolinite are generated via a chemical reaction. In the presence of kaolinite, the release of Al^{3+} species into solution and the precipitation of Fe^{3+} hydroxide are two simultaneous processes. The increase in iron accumulation leads initially to the production of nodule nuclides that progressively grow with the iron content and, finally,

laterite 'concrete' is formed with amorphous silica which acts as binder. These features together with the disordered structure of laterites enhance their merits as an aluminosilicate precursor for production of geopolymer binders via alkali activation. Their reactivity and behavior during the key polycondensation step of geopolymerization should be linked to the degree of iron accumulation. The resulting inorganic (geopolymer) binder is expected to comprise alkali aluminosilicate hydrate with Al partially replaced with Fe. In tropical regions, laterite generally occurs at the surface. Hence, their extraction is simpler and less detrimental to the environment. The option of lime activation (similar to that practiced with volcanic deposits) could also be applied to laterite clay. This only requires consideration of the retarding effects of iron (hydr)oxide which tends to coat kaolinite particles. The option exercised here, however, involves alkali activation of laterite clay, which expands the selections of indigenous cementitious binders. This option could better suit laterite soils which, depending on their specific characteristics, could be less reactive than volcanic deposits. There are also structural differences between lime-activated aluminosilicates which yield calcium aluminosilicate hydrate (C-A-S-H) and calcium silicate hydrate (C-S-H) versus alkali activated aluminosilicates which yield alkali aluminosilicate hydrates (e.g., Na-A-S-H or N-A-S-H). The structure of N-A-S-H tends to be more ordered than that of C-A-S-H. Crosslinking is a distinct feature which distinguishes C-(N)-A-S-H from the non-crosslinked tobermite-lime C-S-H gels in Portland cement concrete. Crosslinking is accomplished via AlO_4 tetrahedra, and improves the properties of C-A-S-H and N-A-S-H when compared with C-S-H. Among the indigenous formulations considered for production of laterite clay-based aluminosilicate hydrate binders, that comprising laterite clay: calcined laterite clay at 0.7: 0.3 weight ratio, activated with soda ash and lime, produced mortars with high early-age compressive strengths. Calcination of laterite clay was accomplished in moderate conditions. SEM/EDX evaluation of a laterite-based binder activated with soda ash/lime, without any calcination of laterite, confirmed the presence of the laterite precursor and the activators. In this case, a gradient structure was noted across the depth, pointing at leaching of sodium attributed to incomplete transformation of laterite

(without any calcination) via polycondensation into a stable binder. XRD spectra of laterite and the laterite-based binder pointed at a relatively high degree of crystallinity of the laterite used here, and the presence of carbonates and aluminosilicate hydrate in binder, noting that the alkali aluminosilicate hydrate binder formed here would be largely amorphous.

9.3 Indigenous Reinforcement

Natural (e.g., jute, sisal, kenaf) fabric (burlap) and chicken mesh are the indigenous reinforcement systems selected for production of ferrocement with the indigenous binders developed in the project. Ferrocement is a thin-sheet reinforced cementitious product which offers a distinct balance of engineering properties, and can be processed, using unskilled labor, into structurally efficient configurations. A host of plant fibers which are abundantly available in Africa, middle east and elsewhere can be used for production of natural fabric (burlap). Jute burlaps of different yarn size and spacing were used in Phase I project. Processing of vegetable fiber into yarn and fabric is a widespread practice in developing nations. Two jute burlaps and one chicken mesh were used as indigenous reinforcement in Phase I project. The burlap with finer openings was made of 1.2 mm diameter yarns with 1.5 mm clear spacing; that with coarser openings was made of 0.9 mm yarns with 3 mm clear spacing. Tension testing of the jute burlaps and chicken mesh indicated that burlaps compare well with chicken mesh in terms of tensile strength, stiffness and ductility.

9.4 Building System and Indigenous Sandwich Composite Module

A sandwich composite comprising ferrocement skins and an aerated concrete core was devised as an indigenous building module to efficiently meet the structural criteria while playing a multi-functional role towards satisfying the insulation and projectile penetration resistance requirements. A preliminary design was devised for the sandwich composite module based on the following requirements: blast resistance (out-of-plane and in-plane behavior), projectile penetration resistance, seismic forces, and thermal insulation.

9.5 Indigenous Ferrocement

Ferrocement sheets were produced and characterized using three indigenous reinforcement systems: two jute burlaps, and chicken mesh. Ferrocement is a thin-sheet cement product where fabrics comprising relatively small-diameter wires with high specific surface area are used as reinforcement in a cementitious mortar matrix. The reinforcement volume fraction in ferrocement is relatively large when compared with that in conventional reinforced concrete. The high reinforcement ratio and specific surface area, and the improved bonding via mechanical anchorage of the 2D fabric reinforcement induce multiple cracking in ferrocement under tensile and flexural loading. This phenomenon enables redistribution of force from critically stressed regions, and enhances the ductility and energy absorption capacity of ferrocement structures. A basic theoretical framework was devised for analysis and design of ferrocement with different reinforcement and matrix systems. This framework encompasses a minimum reinforcement ratio to encourage brittle modes of failure, crack spacing when the preferred multiple-cracking mode of failure governs, and tensile load-bearing capacity. Ferrocement thin sheets were developed with two jute burlap and also the chicken mesh reinforcement systems. Tension tests were performed, and the results were evaluated against theoretical predictions. The concept of minimum reinforcement ratio for inducing ductile modes of failure and multiple cracking was verified. Adequate reinforcement ratios were found to induce the strain-hardening type of behavior. The ultimate tensile load-bearing capacity of ferrocement was found to exceed that of its constituent reinforcement. This was attributed to the stress redistribution capabilities (after local fiber/yarn rupture) provided by the cementitious matrix, precipitation of hydrates within yarn pores (which raises their strength), and the governing role of cementitious matrix in determining the location of failure which is probably away from the weakest link(s) within the reinforcing fabric. Tension test results also indicated that jute burlaps can produce ferrocement sheets with structural qualities (strength, stiffness, ductility) which match those offered by chicken mesh (steel fabric) reinforcement. Projectile penetration tests performed on ferrocement skins confirmed the theoretical

prediction that a skin alone is not capable of mitigating the penetration of the projectile with typical mass and speed considered in the experimental work. Bond tests performed on natural fabric reinforcement embedded in indigenous ferrocement sheets yielded test data based on which the bond strength and the required development length of a selected natural fabric in an indigenous binder was calculated. The measured values of bond and development length provided further evidence for the viability of the indigenous building system that is under development in the project.

9.6 Indigenous Aerated Concrete

Aerated concrete constitutes the lightweight core of the sandwich composite used in the project as the fundamental module for building construction. The aerated concrete should provide adequate mechanical properties (e.g., shear strength and modulus, tensile strain capacity) to enable the structurally efficient sandwich composite behavior. The aerated concrete core should also provide adequate insulation qualities, and should make viable contributions towards resistance of the sandwich composite against projectile penetration. Aerated concrete comprises a cementitious matrix within which air bubbles are introduced (as replacement for aggregates in normal concrete) using a foaming agent. Aerated concrete uses foaming principles that are used in broad fields of application. It comprises foams that were formed and stabilized in the mixing water of concrete using a surfactant (surface active agent). Surfactants are molecules with polar and non-polar ends; they lower the surface tension of water. A foam inevitably forms in water carrying a surfactant because the non-polar part of surfactant molecules bonds well with air and stabilizes the foam. Surfactant molecules can stabilize air bubbles by orienting themselves on the interfaces of the bubbles with water. Considering the breadth of surfactant applications, they are available abundantly across the world. Two surfactants were evaluated as examples of those which are indigenous to the targeted geographic areas: (i) saponin (a major constituent of diverse plants); and (ii) egg white. Saponins are natural surfactants found abundantly in various plant species. Saponin molecules comprise hydrophobic steroid or triterpenoid group, and one or several hydrophilic oligosaccharide chains attached

to this group. Saponins are used in cosmetic, food and pharmaceutical products due to their excellent ability to stabilize emulsions and foams, and also because they can solubilize bulky hydrophobic molecules. Egg white largely comprises proteins with surfactant qualities. When egg white is beaten, air is added and proteins are denatured, exposing their hydrophobic and hydrophilic ends. The proteins align themselves between air and water, forming stable foams. In addition, the proteins can bond to one another side-to-side as crosslinks which add to the foam stability. An experimental program was conducted where different foaming agents (saponin, egg white and liquid soap) were used at different dosages within cementitious matrices based on Portland cement or lime-gypsum. The stability of the resulting foam, and its impact on the density as well as the physical and mechanical properties of aerated concrete incorporating the foam were investigated. Several indigenous aerated concrete materials were developed successfully. One with lime-gypsum matrix and saponin foaming agent was selected for further characterization. It was found to provide a viable balance of compressive, tensile and flexural strengths, density, thermal conductivity, stability of the foam structure, elastic and shear moduli, sorptivity, and projectile penetration resistance (which agreed with past experience and theoretical predictions) for use as the lightweight core in indigenous sandwich composites.

9.7 Preliminary Work on Indigenous Sandwich Composites

Preliminary studies were conducted on indigenous sandwich composites comprising ferrocement skins with jute burlap reinforcement and an aerated concrete core made of lime-gypsum matrix and saponin foaming agent. The aerated concrete used here was of relatively high density. Flexure tests of this sandwich composite produced failure modes which pointed at the contributions of the relatively dense aerated concrete core to flexural performance. Lighter cores with relatively large strain capacity as well as improved bonding of ferrocement skins to the aerated concrete core would be required for realizing failure modes which ensure effective use of the ferrocement skin strength and ductility towards achieving a desired balance of flexural strength, ductility and toughness (as well as shear strength, thermal

insulation qualities and penetration resistance). These improvements would avoid premature delamination of skins from the core, and would avoid premature failure modes initiated in the core.

9.8 Production and Structural Evaluation of Indigenous Sandwich Composites

Sandwich composite structural components resembling those identified through a preliminary structural design of a B-hut were produced and subjected to structural tests concerned with their out-of-plane flexure and in-plane shear performance. As a first step, given the experience gained with flexure testing of smaller sandwich composite specimens, an indigenous shear connector was developed for preventing premature delamination of ferrocement skins from the aerated concrete core, and for ensuring integrated structural performance of the sandwich composite constituents. The shear connectors are chicken mesh strips connecting the two ferrocement skins through the aerated concrete core. An experimental program was conducted through which the contribution of the chicken mesh shear connector to transfer of shear forces across the ferrocement skin-aerated concrete core interface was measured. Procedures were devised for design of chicken mesh shear connectors in sandwich composite structural components, through which the interfacial shear strength test data were used to identify the required spacing of chicken mesh strips (shear connectors). The spacing was found to be reasonable, enabling practical construction of indigenous sandwich composite structural components incorporating them. Relatively large sandwich composite components were produced for performance of structural tests. These components were subjected to out-of-plane flexure and in-plane shear (diagonal compression) tests. The flexure and compression test components were 1,200 mm long, 300 mm wide, and 100 mm thick. Shorter flexure test specimens with 500 mm length and similar cross-section were also fabricated. The in-plane shear (diagonal compression) test components were 500 mm square with 100 mm thickness. The thickness of all structural test components comprised 80 mm of an indigenous lightweight concrete core with two 10 mm thick indigenous ferrocement skins incorporating natural jute burlap reinforcement. The structural test components were produced by sequential placement of the lower ferrocement skin (with

chicken mesh shear connectors), the aerated concrete core, and the upper ferrocement skin. These test components were cured under wet burlap for four days, and then exposed to ambient conditions. Out-of-plane bending tests were performed on spans of 1000 mm and 500 mm by four-point loading. Failure of specimens initiated by cracking of the tension ferrocement skin (with multiple cracking of skin observed in some tests). Further increase in loading led to growth of the skin crack a short distance along the interface, and its extension into the core. This failure phenomenon led to eventual loss of sandwich composite action, which led to flexural cracking of the other skin. Failure of both short- and long-span specimens in out-of plane loading was governed by flexure, pointing at the high resistance of the indigenous aerated concrete to shear failure modes. The shear connector design could be improved to mitigate the short-distance delamination at the location of skin cracking. Failure of sandwich composites in out-of-plane bending could be qualified as ductile for both the short- and long-span panels tested in Phase I project. Load could be increased significantly beyond initial cracking of the skin, and the post-peak deformation capacity was significant without any sudden drop in load-carrying capacity. Theoretical models were developed for predicting the out-of-plane load-carrying capacity of sandwich composite panels governed by three failure modes: (i) flexural failure induced by tensile failure of the skin; (ii) shear failure governed by diagonal tensile cracking of the core; and (iii) flexural failure induced by tensile cracking of the core at the skin-core interface. It should be noted that shear connectors were previously designed to mitigation the skin-core delamination failure mode. Theoretical analyses indicated that failure of the indigenous sandwich composite panels tested in Phase I project under out-of-plane loading on long and short spans is governed by flexural action involving failure of the tension skin. This theoretical prediction confirmed experimental observations. The experimentally measured out-of-plane load-carrying capacities of the indigenous sandwich composite panels were 17-27% lower than the theoretically predicted values. This can be partly explained by the flaws generated during scaled-up production of these first-generation sandwich composite panels. The in-plane behavior of sandwich

composite walls under lateral (e.g., wind) and gravity loads was simulated by diagonal compression loading of sandwich composite panels. Failure of panels under in-plane diagonal compression loading was governed by tensile (diagonal) cracking of skins parallel to the loading direction. Failure of the indigenous sandwich composite panel under in-plane loading was ductile, reflecting the ductile tensile behavior of ferrocement skins. The load-deflection behavior beyond initial diagonal cracking of the skin exhibited an ascending branch with crack propagation. Beyond the peak load, the drop in load was gradual, and the sandwich composite panel provided a relatively large deformation capacity under in-plane loading. Different theoretical models were used to predict the failure load of sandwich composite panels subjected to in-plane diagonal compression. A model commonly used for calculating the principal tensile stress under in-plane loading produced reasonable predictions of the in-plane load-carrying capacity of the sandwich composite panel when the principal stress reached the tensile strength of the indigenous ferrocement skin. The experimentally measured value of in-plane (diagonal compression) load-bearing capacity was 18% less than the theoretical prediction. This difference could be partly explained by the flaws generated during scaled-up production of these first-generation sandwich composite panels.

9.9 Assessment of the Competitive Advantages

The indigenous building materials and systems developed in the project offer the following competitive advantages: (i) versatility of indigenous building construction materials for use in diverse geographic and climatic regions; (ii) versatility of the building components and systems for design of safe, serviceable and efficient buildings under diverse loading systems, ranging from common gravity and wind loads to those corresponding to extreme events (blast, projectile impact, severe earthquake); (iii) convenient, expeditious and economical construction with indigenous materials and resources; (iv) structural efficiency and reduced weight for exercising the options of supporting on a gavel layer or a footing system, depending upon the loading conditions considered; (v) ease of demolition and disposal or recycling of building materials and components; (vi) inherent fire resistance; (vii) integration of thermal insulation into

the load-bearing structural system; (viii) inherently healthy living environment; (ix) versatility for development of semi-permanent as well as conventional military and civilian building systems; (x) potential to use low-quality water at limited quantities for building construction; (xiii) moisture resistance; (xiii) economics; and (xiv) use of indigenous materials for construction of infrastructure systems other than buildings.

9.10 Development of Numerical Modeling Capabilities

Finite element models were developed for indigenous sandwich composite panels and building systems comprising these panels as walls, roof and floor. Nonlinear finite element analyses of sandwich composite panels were performed under out-of-plane loading, and of building systems under different combinations of factored dead, live, wind and snow loading. The sandwich composite panels considered here comprised indigenous aerated lime-gypsum core and indigenous ferrocement skins. Perfect interfacial stress transfer was assumed between the core and skins. The finite element modeling and analyses were conducted using the ANSYS software. A fine mesh with solid elements was used in finite element modeling of the sandwich composite panel. Shell elements were used in the case of the building system in order to reduce the required computational time and capacity. Finite element analysis of the sandwich composite panel was performed under uniform gravity loading, and the deformation behavior, and stress and strain distributions of the panel were produced. In the case of the building system, finite element analysis was performed under different factored load combinations, and the resulting deformation patterns, and stress and strain distributions were produced. Discussions were made based on the outcomes of finite element analyses in light of the experimental findings. Recommendations were made to improve the stability and efficiency of the numerical solutions.

REFERENCES

REFERENCES

1. Windstorm, B. and A. Schmidt, *A Report of Contemporary Rammed Earth Construction and Research in North America*. Sustainability, 2013. **5**(2): p. 400-416.
2. Kuchena, J. and P. Usiri, *Low cost construction technologies and materials-case study Mozambique*. 2009.
3. Al-Chaar, G., et al., *Indigenous Construction Materials for Theater Facilities*. 2013, DTIC Document.
4. Pullen, Q.M., *Strength and Composition of Willamette Valley Cob: An Earthen Building Material*. 2009.
5. Sherpa, D., *Affordable Solution for Earthquake Resistant Building Construction in Haiti*. 2010.
6. Shittu, T.A., *Development of a framework for sustainable repair of adobe building in an urban area in Nigeria*. 2012.
7. Silveira, D., H. Varum, and A. Costa, *Influence of the testing procedures in the mechanical characterization of adobe bricks*. Construction and Building Materials, 2013. **40**: p. 719-728.
8. SIMENSON, E.W., *RAMMED EARTH: FIBER-REINFORCED, CEMENT-STABILIZED*. 2013, University of Colorado.
9. Swan, A.J., A. Rteil, and G. Lovegrove, *Sustainable earthen and straw bale construction in North American buildings: Codes and practice*. Journal of Materials in Civil Engineering, 2011. **23**(6): p. 866-872.
10. Billong, N., et al., *Properties of compressed lateritic soil stabilized with a burnt clay-lime binder: Effect of mixture components*. Construction and Building Materials, 2009. **23**(6): p. 2457-2460.
11. Bui, Q., et al., *Durability of rammed earth walls exposed for 20 years to natural weathering*. Building and Environment, 2009. **44**(5): p. 912-919.
12. Jain, A.K. and M.C. Paliwal. *Adoption of Appropriate and Cost Effective Technologies in Housing: Indian Experience*. World Academy of Science, Engineering and Technology.
13. Kogbara, R.B. and A. Al-Tabbaa, *Mechanical and leaching behaviour of slag-cement and lime-activated slag stabilised/solidified contaminated soil*. Science of the Total Environment, 2011. **409**(11): p. 2325-2335.
14. Reddy, V.B., *Sustainable building technologies*. Current Science, 2004. **87**(7): p. 899-907.
15. Sukmak, P., et al., *Factors influencing strength development in clay-fly ash geopolymer*. Construction and Building Materials, 2013. **47**: p. 1125-1136.

16. Zhang, M., et al., *Experimental feasibility study of geopolymer as the next-generation soil stabilizer*. Construction and Building Materials, 2013. **47**: p. 1468-1478.
17. Gamrani, N., et al., *The particular "rammed earth" of the Saadian sugar refinery of Chichaoua (XVIth century, Morocco): mineralogical, chemical and mechanical characteristics*. Environmental Earth Sciences, 2012. **66**(1): p. 129-140.
18. Karim, M.R., et al., *Fabrication of a non-cement binder using slag, palm oil fuel ash and rice husk ash with sodium hydroxide*. Construction and Building Materials, 2013. **49**: p. 894-902.
19. Lugowski, J., *Ferrocement Super-Insulated Shell House Design and Construction*. 2013.
20. Morsy, M.S., S.H. Alsayed, and Y.A. Salloum, *Development of eco-friendly binder using metakaolin-fly ash-lime-anhydrous gypsum*. Construction and Building Materials, 2012. **35**: p. 772-777.
21. Alavez-Ramirez, R., et al., *Thermal lag and decrement factor of a coconut-ferrocement roofing system*. Construction and Building Materials, 2014. **55**: p. 246-256.
22. Greepala, V. and P. Nimityongskul, *Structural integrity and insulation property of ferrocement exposed to fire*. Journal of ferrocement, 2006. **36**(4): p. 939.
23. Greepala, V. and P. Nimityongskul, *Structural integrity of ferrocement panels exposed to fire*. Cement & Concrete Composites, 2008. **30**(5): p. 419-430.
24. Saleem, M. and M. Ashraf, *Low cost earthquake resistant ferrocement small house*. J. Pak. J. Engg. & Appl. Sci, 2008. **2**.
25. Thanoon, W.A., et al., *Structural behaviour of ferrocement-brick composite floor slab panel*. Construction and Building Materials, 2010. **24**(11): p. 2224-2230.
26. Wafa, M.A. and K. Fukuzawa, *Characteristics of ferrocement thin composite elements using various reinforcement meshes in flexure*. Journal of Reinforced Plastics and Composites, 2010. **29**(23): p. 3530-3539.
27. Alomayri, T., F.U.A. Shaikh, and I.M. Low, *Synthesis and mechanical properties of cotton fabric reinforced geopolymer composites*. Composites Part B: Engineering, 2014. **60**: p. 36-42.
28. Alomayri, T., F.U.A. Shaikh, and I.M. Low, *Effect of fabric orientation on mechanical properties of cotton fabric reinforced geopolymer composites*. Materials and Design, 2014. **57**: p. 360-365.
29. Reis, J.M.L., *Fracture and flexural characterization of natural fiber-reinforced polymer concrete*. Construction and Building Materials, 2006. **20**(9): p. 673-678.
30. Teixeira-Pinto, A., et al. *Geopolymer-jute composite: A novel environmentally friendly composite with fire resistant properties*. in *31st International Conference on Advanced Ceramics and Composites, January 21, 2007 - January 26, 2007*. 2008. Daytona Beach, FL, United states: American Ceramic Society.

31. Al-Chaar, G.K., M. Alkadi, and P.G. Asteris, *Natural pozzolan as a partial substitute for cement in concrete*. Open Construction and Building Technology Journal, 2013. **7**: p. 33-42.
32. Al-Chaar, G.K., et al., *The Use of Natural Pozzolan in Concrete as an Additive or Substitute for Cement*. 2011, DTIC Document.
33. Shannag, M.J. and T. Bin Ziyad, *Flexural response of ferrocement with fibrous cementitious matrices*. Construction and Building Materials, 2007. **21**(6): p. 1198-1205.
34. Cheah, C.B. and M. Ramli, *Load capacity and crack development characteristics of HCWA-DSF high strength mortar ferrocement panels in flexure*. Construction and Building Materials, 2012. **36**: p. 348-357.
35. Kahn, M.E., *The death toll from natural disasters: the role of income, geography, and institutions*. Review of Economics and Statistics, 2005. **87**(2): p. 271-284.
36. Ngo, T., et al., *Blast loading and blast effects on structures—an overview*. Electronic Journal of Structural Engineering, 2007. **7**: p. 76-91.
37. Bondar, D., et al., *Effect of type, form, and dosage of activators on strength of alkali-activated natural pozzolans*. Cement and Concrete Composites, 2011. **33**(2): p. 251-260.
38. Yang, K.H., H.Z. Hwang, and S. Lee, *Effects of Water-Binder Ratio and Fine Aggregate-Total Aggregate Ratio on the Properties of Hwangtoh-Based Alkali-Activated Concrete*. Journal of Materials in Civil Engineering, 2010. **22**(9): p. 887-896.
39. Sargent, P., et al., *The use of alkali activated waste binders in enhancing the mechanical properties and durability of soft alluvial soils*. Engineering Geology, 2013. **152**(1): p. 96-108.
40. Van Chanh, N., B.D. Trung, and D. Van Tuan. *Recent research geopolymers concrete*.
41. Van Jaarsveld, J.G.S., J.S.J. Van Deventer, and G.C. Lukey, *The effect of composition and temperature on the properties of fly ash-and kaolinite-based geopolymers*. Chemical Engineering Journal, 2002. **89**(1): p. 63-73.
42. Provis, J.L. and J.S.J. van Deventer, *Alkali Activated Materials: State-of-the-art Report, RILEM TC 224-AAM*. 2014: Springer Dordrecht.
43. Rajendran, M. and N. Soundarapandian, *Geopolymer ferrocement panels under flexural loading*. Science and Engineering of Composite Materials: p. 1-11.
44. Rajendran, M. and N. Soundarapandian, *An experimental investigation on the flexural behavior of geopolymer ferrocement slabs*. Journal of Engineering and Technology, 2013. **3**(2): p. 97.
45. Sreevidya, V., R. Anuradha, and R. Venkatasubramani, *Experimental study on geopolymer ferrocement slab using various wire meshes*. Journal of Structural Engineering (India), 2012. **39**(4): p. 436-443.

46. Arellano Aguilar, R., O. Burciaga Díaz, and J. Escalante García, *Lightweight concretes of activated metakaolin-fly ash binders, with blast furnace slag aggregates*. Construction and building materials, 2010. **24**(7): p. 1166-1175.
47. Song, X., *Development and performance of class F fly ash based geopolymer concretes against sulphuric acid attack*. 2007, The University of New South Wales.
48. Yao, W. and Z. Li, *Flexural behavior of bamboo–fiber-reinforced mortar laminates*. Cement and concrete research, 2003. **33**(1): p. 15-19.
49. Ali, M. and N. Chouw. *Coir fibre and rope reinforced concrete beams under dynamic loading*. in *Annual Australian Earthquake Engineering Society Conference, "Newcastle Earthquake–20 years on*. 2009.
50. Ali, M. and N. Chouw, *Experimental investigations on coconut-fibre rope tensile strength and pullout from coconut fibre reinforced concrete*. Construction and Building Materials, 2013. **41**: p. 681-690.
51. Kim, S.Y., et al., *Tests of reinforced concrete beams strengthened with wire rope units*. Engineering Structures, 2007. **29**(10): p. 2711-2722.
52. Quagliarini, E., et al., *Tensile characterization of basalt fiber rods and ropes: A first contribution*. Construction and Building Materials, 2012. **34**: p. 372-380.
53. Yang, K.H., G.H. Kim, and H.S. Yang, *Shear behavior of continuous reinforced concrete T-beams using wire rope as internal shear reinforcement*. Construction and Building Materials, 2011. **25**(2): p. 911-918.
54. Li, Z., L. Wang, and X.A. Wang, *Cement composites reinforced with surface modified coir fibers*. Journal of composite materials, 2007. **41**(12): p. 1445-1457.
55. Alomayri, T., F.U.A. Shaikh, and I.M. Low, *Thermal and mechanical properties of cotton fabric-reinforced geopolymer composites*. Journal of Materials Science, 2013. **48**(19): p. 6746-6752.
56. Alavez-Ramirez, R., et al., *Thermal conductivity of coconut fibre filled ferrocement sandwich panels*. Construction and Building Materials, 2012. **37**: p. 425-431.
57. Ribeiro, B., D. Barreto, and M. Coelho, *Application of foam column as green technology for concentration of saponins from sisal (Agave sisalana) and Juá (Ziziphus joazeiro)*. Brazilian Journal of Chemical Engineering, 2013. **30**(4): p. 701-709.
58. Remadnia, A., et al., *Use of animal proteins as foaming agent in cementitious concrete composites manufactured with recycled PET aggregates*. Construction and Building Materials, 2009. **23**(10): p. 3118-3123.
59. Greepala, V. and P. Nimityongskul, *Influence of Heating Envelope on Structural Fire Integrity of Ferrocement Jackets*. Fire Technology, 2009. **45**(4): p. 385-404.

60. Hago, A.W., et al., *Ultimate and service behavior of ferrocement roof slab panels*. Construction and Building Materials, 2005. **19**(1): p. 31-37.
61. Nădășan, L. and T. Oneț, *POSSIBLE USE OF FERROCEMENT IN ROMANIA*. Bulletin of the Polytechnic Institute of Iasi-Construction & Architecture Section, 2013. **63**(2).
62. Chandramohan, D. and K. Marimuthu, *A Review On Natural Fibers*. International Journal of Research & Reviews in Applied Sciences, 2011. **8**(2).
63. Sarsby, R.W., *Limited-life geosynthetics*. Geosynthetics in civil engineering: p. 244.
64. Tawab, A.A., E.H. Fahmy, and Y.B. Shaheen, *Use of permanent ferrocement forms for concrete beam construction*. Materials and Structures, 2012. **45**(9): p. 1319-1329.
65. Swarnamala, W.R., *Out-of-Plane Strengthening of unreinforced masonry walls using textile reinforced mortar systems*. 2010.
66. ASPINALL, A. and S. WARREN, *Making cements*.
67. Narayanan, N. and K. Ramamurthy, *Structure and properties of aerated concrete: a review*. Cement and Concrete Composites, 2000. **22**(5): p. 321-329.
68. Abeyruwan, H., *CEMENT, SOCIETY AND SUSTAINABILITY*. 2014.
69. Colleparidi, M., *Thaumasite formation and deterioration in historic buildings*. Cement and Concrete Composites, 1999. **21**(2): p. 147-154.
70. Jackson, M.D., et al., *Material and elastic properties of Al-tobermorite in ancient Roman seawater concrete*. Journal of the American Ceramic Society, 2013. **96**(8): p. 2598-2606.
71. Rodríguez-Navarro, C. *Binders in historical buildings: traditional lime in conservation*. in *International seminar on archaeometry and cultural heritage: the contribution of mineralogy*. Bilbao: Sociedad Española de Mineralogía. 2012.
72. ŠKVÁRA, F., et al., *Geopolymer concrete-an ancient material too?* Ceramics– Silikáty, 2008. **52**(4): p. 296-298.
73. Cantisani, E., et al., *The binder of the Roman concrete of the Ponte di Augusto at Narni (Italy)*. Per. Mineral, 2002. **71**: p. 113-123.
74. Okeniyi, A., S. Adeniji, and B. Dahunsi, *Effects of Chemical Additives on the Production of Structural Brick for Construction Works*. Journal of Chemical, Mechanical and Engineering Practice, 2012. **2**(3): p. 18-23.
75. Crisp, J., et al., *Crystallization history of the 1984 Mauna Loa lava flow*. Journal of Geophysical Research: Solid Earth (1978–2012), 1994. **99**(B4): p. 7177-7198.

76. SHI, C., F. HE, and P. Angel, *Classification and characteristics of alkali-activated cements*. Journal of The Chinese Ceramic Society, 2012. **40**(1): p. 69-75.
77. Khatib, J., et al., *Fly ash paste activated with lime incorporating metakaolin*. Engineering (ICITE 2014), 2014. **1**: p. 13.
78. Shoji, S., et al., *Chemical and mineralogical studies on volcanic ashes I. Chemical composition of volcanic ashes and their classification*. Soil science and plant nutrition, 1975. **21**(4): p. 311-318.
79. Cashman, K.V., C. Thornber, and J.P. Kauahikaua, *Cooling and crystallization of lava in open channels, and the transition of Pāhoehoe Lava to 'A'ā*. Bulletin of Volcanology, 1999. **61**(5): p. 306-323.
80. Gartner, E.M. and D.E. Macphee, *A physico-chemical basis for novel cementitious binders*. Cement and Concrete Research, 2011. **41**(7): p. 736-749.
81. Cultrone, G., E. Sebastián, and M.O. Huertas, *Forced and natural carbonation of lime-based mortars with and without additives: Mineralogical and textural changes*. Cement and Concrete Research, 2005. **35**(12): p. 2278-2289.
82. Chatterji, J., D.C. Brenneis, and C.L. Keys, *Geopolymer Cement Compositions and Methods of Use*. 2012, Google Patents.
83. ALLAHVERDI, A. and J. GHORBANI, *CHEMICAL ACTIVATION AND SET ACCELERATION OF LIME-NATURAL POZZOLAN CEMENT*. Ceramics – Silikáty, 2006. **50**(4): p. 193-199.
84. Garcia-Lodeiro, I., et al., *Compatibility studies between NASH and CASH gels. Study in the ternary diagram $Na_2O-CaO-Al_2O_3-SiO_2-H_2O$* . Cement and Concrete Research, 2011. **41**(9): p. 923-931.
85. Bakker, J. and H. Brouwers, *Mortar and concrete based on calcium sulphate binders*. 2006.
86. Badens, E., S. Veessler, and R. Boistelle, *Crystallization of gypsum from hemihydrate in presence of additives*. Journal of Crystal Growth, 1999. **198**: p. 704-709.
87. Igea Romera, J., et al., *Assessment of the physico-mechanical behaviour of gypsum-lime repair mortars as a function of curing time*. Environmental Earth Sciences, 2013. **70**(4): p. 1605-1618.
88. Baux, C., C. Lanos, and A. Phelipot-Mardelé. *Mineral Foams with improved performances*. in *Annales du Bâtiment et des travaux publics*. 2011.
89. Lesovik, V.S., et al., *Effective Composite Gypsum Binders On The Basis Of Raw Materials From The Middle East Countries*. Advances in Natural & Applied Sciences, 2014. **8**(5).
90. Arikan, M. and K. Sobolev, *The optimization of a gypsum-based composite material*. Cement and Concrete Research, 2002. **32**(11): p. 1725-1728.

91. Chindaprasirt, P., et al., *Plaster materials from waste calcium sulfate containing chemicals, organic fibers and inorganic additives*. Construction and Building Materials, 2011. **25**(8): p. 3193-3203.
92. Carvalho, M.A., et al., *Microstructure and mechanical properties of gypsum composites reinforced with recycled cellulose pulp*. Materials Research, 2008. **11**(4): p. 391-397.
93. Davidovits, J., *Geopolymer Chemistry and Applications*. 3 ed. 2011: Geopolymer Institute.
94. Adekunle, A., et al., *Analysis of Thermal and Electrical Properties of Laterite, Clay and Sand Samples and Their Effects on Inhabited Buildings in Ota, Ogun State, Nigeria*. Journal of Sustainable Development Studies, 2014. **6**(2).
95. Eisazadeh, A., K.A. Kassim, and H. Nur, *Characterization of phosphoric acid-and lime-stabilized tropical lateritic clay*. Environmental Earth Sciences, 2011. **63**(5): p. 1057-1066.
96. Eisazadeh, A., K.A. Kassim, and H. Nur, *Solid-state NMR and FTIR studies of lime stabilized montmorillonitic and lateritic clays*. Applied Clay Science, 2012. **67**: p. 5-10.
97. Obonyo, E.A., et al., *A Sustainable Approach for the Geopolymerization of Natural Iron-Rich Aluminosilicate Materials*. Sustainability, 2014. **6**(9): p. 5535-5553.
98. Lemougna, P.N., et al., *Laterite based stabilized products for sustainable building applications in tropical countries: review and prospects for the case of Cameroon*. Sustainability, 2011. **3**(1): p. 293-305.
99. Zini, E. and M. Scandola, *Green composites: An overview*. Polymer Composites, 2011. **32**(12): p. 1905-1915.
100. Naaman, A.E., *Ferrocement and laminated cementitious composites*. Vol. 3000. 2000: Techno press.
101. Satyanarayana, K.G., et al., *Natural fibre-polymer composites*. Cement & Concrete Composites, 1990. **12**(2): p. 117-136.
102. Thomason, J.L., et al., *Fibre cross-section determination and variability in sisal and flax and its effects on fibre performance characterisation*. Composites Science and Technology, 2011. **71**(7): p. 1008-1015.
103. PertanGroup, *Comparison and Analysis of Energy Performance of Temporary Army Shelters*. 2013, U.S. Army. p. 36.
104. Dick, R., *Blast Design and Analysis*, in *Architectural Engineering*. 2012, Pennsylvania State University. p. 63.
105. Babaeidarabad, S., *Masonry Walls Strengthened with Fabric-Reinforced Cementitious Matrix Composite Subjected to In-Plane and Out-of-Plane Load*. 2013.
106. Churilov, S. and E. Dumova-Jovanoska, *In-plane shear behaviour of unreinforced and jacketed brick masonry walls*. Soil Dynamics and Earthquake Engineering, 2013. **50**: p. 85-105.

107. Ahmad Zaidi, A.M. and Q.M. Li, *Investigation on penetration resistance of foamed concrete*. Proceedings of the Institution of Civil Engineers: Structures and Buildings, 2009. **162**(1): p. 77-85.
108. Hamad, A.J., *Materials, Production, Properties and Application of Aerated Lightweight Concrete: Review*. 2014.
109. Al-Kashif, M., et al. *Nonlinear Modeling and Analysis of AAC in-filled Sandwich Panels for out of Plane Loads*. World Academy of Science, Engineering and Technology.
110. Basunbul, I.A., M. Saleem, and G.J. Al-Sulaimani, *Flexural behavior of ferrocement sandwich panels*. Cement and Concrete Composites, 1991. **13**(1): p. 21-28.
111. Radin Sumadi, S. and M. Ramli, *Development of lightweight ferrocement sandwich panels for modular housing and industrialized building system*. 2008.
112. Shams, A., M. Horstmann, and J. Hegger, *Experimental investigations on textile-reinforced concrete (TRC) sandwich sections*. Composite Structures, 2014. **118**(1): p. 643-653.
113. Manalo, A.C., et al., *Flexural behaviour of structural fibre composite sandwich beams in flatwise and edgewise positions*. Composite Structures, 2010. **92**(4): p. 984-995.
114. Borri, A., et al., *Shear behavior of unreinforced and reinforced masonry panels subjected to in situ diagonal compression tests*. Construction and Building Materials, 2011. **25**(12): p. 4403-4414.
115. Allahverdi, A. and E.N. Kani, *Construction Wastes as Raw Materials for Geopolymer Binders*. International Journal of Civil Engineering, 2009. **7**(3): p. 154-160.
116. Hognestad, E., N.W. Hanson, and D. McHenry. *Concrete stress distribution in ultimate strength design*. in *ACI Journal Proceedings*. 1955. ACI.